Buoyancy-dominated flows of supercritical carbon dioxide
Mixed convection & natural circulation at supercritical pressures
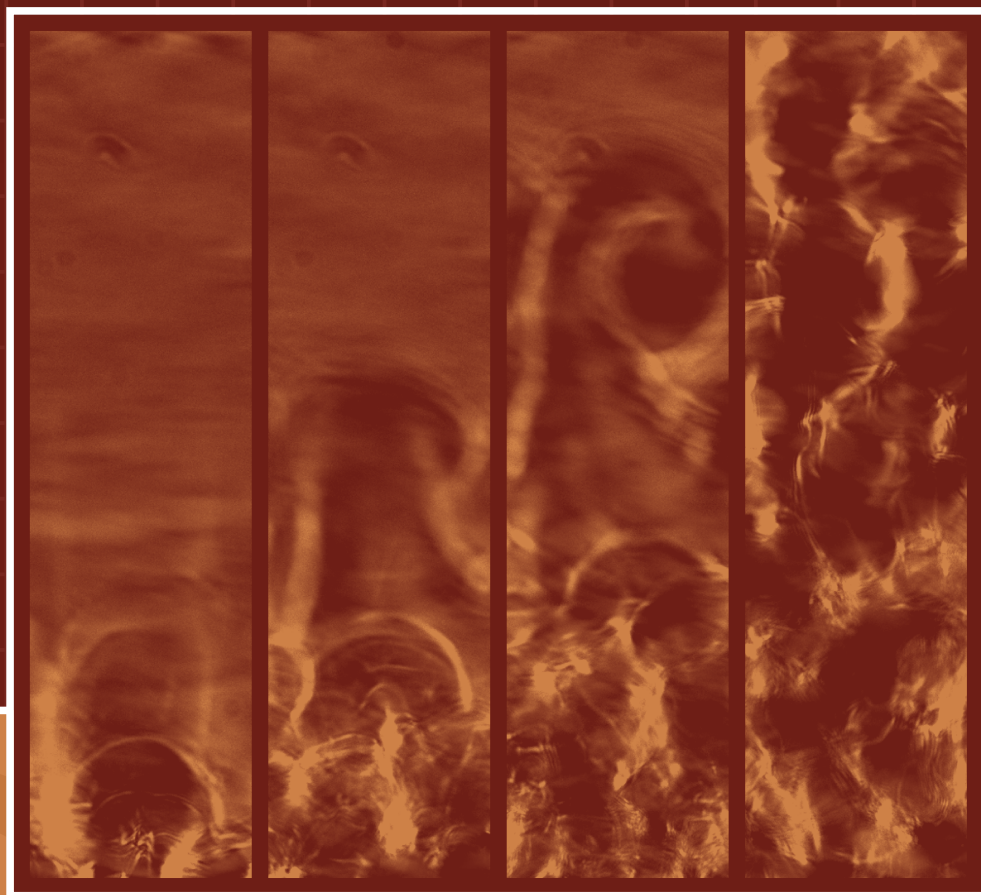
Draskic, Marko

DOI
10.4233/uuid:51558b8b-1927-4aa9-bab4-8caf4f862f7b

Buoyancy-dominated flows of supercritical carbon dioxide

Marko Draskic

Buoyancy-dominated flows of supercritical carbon dioxide

Mixed convection and natural circulation at supercritical pressures

Marko Draskic

Buoyancy-dominated flows of supercritical carbon dioxide

Mixed convection and natural circulation at supercritical pressures

Dissertation

for the purpose of obtaining the degree of doctor
at Delft University of Technology
by the authority of the Rector Magnificus, prof. dr. ir. T.H.J.J. van der Hagen,
chair of the Board for Doctorates
to be defended publicly on
Tuesday 2 September 2025 at 12:30 o'clock

by

Marko Draskic

Master of Science in Mechanical Engineering,
Delft University of Technology, The Netherlands
born in Rotterdam, The Netherlands.

This dissertation has been approved by the promotors.

Composition of the doctoral committee:

Rector Magnificus,	chairperson
Prof. dr. R. Pecnik,	Delft University of Technology, promotor
Prof. dr. ir. J. Westerweel,	Delft University of Technology, promotor

Independent members:

Prof. dr. C. Cierpka,	Ilmenau University of Technology
Prof. dr. ir. J.A. van Oijen,	Eindhoven University of Technology
Prof. dr. ir. R.A.W.M. Henkes,	Delft University of Technology
Dr. ir. M. Rohde,	Delft University of Technology
Dr. ir. J.W.R. Peeters,	Delft University of Technology
Prof. dr. K. Hooman,	Delft University of Technology, reserve member

Keywords:	Supercritical, Carbon Dioxide, Experiments, Shadowgraphy, Natural Circulation Loop, Stratification, Heat Transfer Deterioration
Printed by:	Ridderprint
Cover:	Shadowgraphs of unstable stratification onset in CO_2 at a supercritical pressure (front), & time series of natural circulation loop oscillations (back).

voor mijn moeder, Zora
en mijn vader, Rade

Abstract

A desire to transition away from fossil fuels to more sustainable alternatives has driven the development of energy conversion systems at pressures beyond the vapor-liquid critical point. Transcritical heat pumps, for instance, can decarbonize industrial processes that require heat beyond 100°C, such as drying processes in the food and chemical industry, when powered by renewable electricity. Additionally, supercritical power cycles enable the conversion of heat from previously unsuitable sustainable heat sources into electricity. Therewith, these power cycles can meet the rising demand for non-fossil power, partly driven by the electrification of heat.

However, these systems operate in a highly non-ideal thermodynamic region, where a fluid no longer undergoes a discrete phase transition from liquid to gas when it is heated. Instead, at supercritical pressures, fluids undergo a boiling-like process in which they remain in a continuous phase. During this pseudo-boiling process, fluids exhibit considerable non-linear variations of thermodynamic properties. These variations are most pronounced in the pseudo-critical region, where thermophysical gradients strongly influence flow behavior and heat transfer. The consequences of the variations are most pronounced in the heat exchangers of these energy conversion systems, which operate in the near-pseudo-critical region. In these heat exchangers, buoyancy effects are significantly more dominant than in similar heat exchangers operating with subcritical pressure fluids, leading to highly configuration-dependent heat transfer behavior. Currently, the understanding of these non-ideal effects remains limited, especially in an experimental context, hindering the design of efficient and safe equipment for supercritical energy conversion systems. To bridge this knowledge gap and support the successful implementation of supercritical pressure energy conversion systems, this dissertation investigates the influence of buoyancy on heat transfer in supercritical carbon dioxide (sCO_2) flows, with a specific emphasis on thermal stratification in near-pseudo-critical heat exchangers.

To explore these phenomena, a novel experimental facility was developed, featuring a naturally circulated flow loop operating at supercritical pressures. The four-meter-tall structure exploits the substantial density gradients of sCO_2 to induce a buoyancy force over its vertical legs, driving the flow. By integrating buoyancy-driven natural circulation as the flow-driving mechanism, the facility eliminates the need for mechanical pumps and ensures stable flow conditions for controlled experimentation. The current Natural Circulation Loop (NCL) provides a steady and stable circulation across a broad range of operating conditions. In this work, a steady-state flow rate equation

for the natural circulation of supercritical pressure fluids is proposed and validated against experimental data, demonstrating close agreement between predictions and measured flow rates.

Under specific conditions, when the system's mass flow rate is sufficiently reduced at a constant heating rate, the natural circulation loop becomes unstable. This instability manifests as system-wide oscillations in temperature and pressure, posing a thermal fatigue risk for high-pressure loops. These oscillations are identified as dynamically induced, driven by traveling density waves resulting from periodic deterioration in heat transfer within the NCL heaters. However, these oscillations occur only under a narrow set of conditions and can be mitigated by diffusing the density waves through the system. When appropriate mitigation measures are implemented, natural circulation loops can provide a reliable and stable passive circulation mechanism, making them well-suited for critical applications such as nuclear reactor cooling or for sensitive applications such as the current heat transfer experiments.

A test section integrated within the circulation loop enables optical investigations of flow behavior in a horizontal plate heat exchanger channel, providing insight into buoyancy-induced thermal stratification. The test section employs optical techniques that visualize refractive index variations to capture CO_2 flow motion. These optical methods, used alongside heat transfer measurements, reveal highly transient flow phenomena within the heat exchanger channel for the first time in experiment. Shadowgraphy, in particular, proves effective in visualizing fluid motion in turbulent supercritical CO_2 flows with imhomogeneous temperatures.

In the test section, a hydrodynamically developed flow is examined, with heating applied either from the top or bottom to impose a one-sided density gradient in the CO_2. The results reveal strong stratifications in both heating configurations, occurring much earlier than expected compared to subcritical fluids.

In the two heat transfer configurations, buoyancy effects act in opposite ways. When CO_2 is heated from the bottom, creating an unstable stratification, the channel flow is characterized by secondary motion away from the heated wall. Here, buoyancy enhances heat transfer, enhancing the effect of an increasing specific heat near the wall. As buoyancy effects intensify at higher heating rates, heat transfer progressively improves. Conversely, under stable stratification, when CO_2 is heated from the top downward, the imposed density gradient suppresses turbulence-induced vertical motion, hindering heat removal from the heated wall. As a result, buoyancy opposes the heat transfer enhancement by variable specific heat. As buoyancy effects become more significant, the heat transfer deteriorates beyond an optimum. The heat transfer rates between the two configurations differ by up to an order of magnitude in the current experiments.

The current findings confirm that supercritical CO_2 flows are highly susceptible to buoyancy effects and demonstrate how buoyancy can significantly alter heat transfer relative to a neutrally buoyant setting, often overshadowing other property variation effects. As such, this research contributes to the validation of numerical models and the resolution of previously divergent experimental heat transfer results, thereby aiding in the development of improved predictive models and optimized heat exchanger designs. By enhancing the reliability of supercritical energy conversion system designs, this work supports the broader goal of defossilizing industrial heating and power generation.

Samenvatting

De wens om van fossiele brandstoffen naar duurzamere alternatieven over te gaan heeft heeft geleid tot de ontwikkeling van energieomzetsystemen die werken bij drukken boven het kritieke punt. Transkritieke warmtepompen maken het bijvoorbeeld mogelijk om bepaalde industriële processen die temperaturen boven de 100°C vereisen, zoals droogprocessen in de voedings- en chemische industrie, te verduurzamen wanneer ze worden aangedreven door groene stroom. Daarnaast kunnen superkritieke krachtcycli warmte uit voorheen ongeschikte duurzame warmtebronnen efficient omzetten in elektriciteit, wat helpt om te voldoen aan de groeiende vraag naar fossielvrije energie, deels veroorzaakt door de elektrificatie van warmte.

Echter, deze systemen opereren in een sterk niet-ideale thermodynamische regio, waarin vloeistoffen bij verhitting niet langer een discrete faseovergang van vloeistof naar gas ondergaan. In plaats daarvan doorlopen vloeistoffen bij superkritieke drukken een kookachtig proces, waarbij ze in een continue fase blijven. Tijdens dit pseudo-kookproces vertonen vloeistoffen aanzienlijke niet-lineaire variaties in thermodynamische eigenschappen. De variaties zijn het sterkst in de pseudo-kritieke regio, waar thermofysische gradiënten een grote invloed hebben op het stromingsgedrag en de warmteoverdracht van het medium. De gevolgen hiervan zijn het meest uitgesproken in de warmtewisselaars van de energieomzetsystemen op superkritieke drukken, die worden ontworpen om te opereren in de pseudo-kritieke regio. In deze warmtewisselaars spelen dichtheidsverschillen een veel grotere rol dan in warmtewisselaars met vloeistoffen op lagere, subkritieke drukken, wat leidt tot een warmteoverdracht die sterk afhangt van de configuratie van het systeem. Op dit moment is het experimenteel inzicht in deze effecten nog beperkt, wat het ontwerpen van efficiënte en betrouwbare superkritische energieconversiesystemen bemoeilijkt. In dit proefschrift wordt derhalve onderzocht hoe opwaartse krachten de warmteoverdracht en turbulentie beïnvloeden in superkritieke CO_2-stromingen, met een specifieke focus op thermische stratificatie in warmtewisselaars nabij de pseudo-kritische curve.

Om deze fenomenen te bestuderen is een experimentele installatie ontwikkeld: een stromingslus waarin CO_2 op natuurlijke wijze circuleert bij superkritieke druk. Dit vier meter hoge systeem maakt gebruik van de sterke dichtheidsverschillen van CO_2 om zonder pomp een natuurlijke stroming op te wekken. De stroming van deze passieve circulatie is uiterst stabiel, wat gevoelige stromingsexperimenten mogelijk maakt. In het proefschrift wordt een formule voorgesteld om de massastroom van de natuurlijke circulatie van het superkritieke medium in te lus te voorspellen. Bij

het valideren van de formule met experimentele data blijkt de voorspelling van de formule sterk overeen te komen met de gemeten massastromen van de opstelling.

Bij lage massastromen en hoge warmte-invoeren is het natuurlijke circulatiesysteem vatbaar voor instabiliteiten. Deze instabiliteiten kunnen grote temperatuurschommelingen en drukvariaties veroorzaken die kunnen leiden tot thermische vermoeiing van het gehele systeem. De oscillaties blijken veroorzaakt te worden door reizende dichtheidsgolven die ontstaan door een periodieke verslechtering van de warmteoverdracht in de verwarmingselementen van de lus. De oscillaties kunnen worden onderdrukt door de dichtheidsgolven in het systeem te dempen. Met de juiste maatregelen kan een natuurlijke circulatielus derhalve een betrouwbare en stabiele passieve circulatie genereren, bijvoorbeeld voor kernreactoren of gevoelige warmteoverdrachtsstudies.

Om optische metingen van de stroming in een horizontale warmtewisselaar mogelijk te maken wordt in dit proefschrift een testsectie in de circulatielus geplaatst. Door gebruikt te maken van optische technieken die variaties in de brekingsindex van het medium zichtbaar maken, kan de beweging van CO_2 worden opgenomen. Deze methode, in combinatie met warmteoverdrachtsmetingen, toont in dit proefschrift voor het eerst de sterk dynamische stromingspatronen binnen een warmtewisselaar op superkritieke druk aan. Met name schaduwfotografie (shadowgraphy) blijkt effectief om turbulente bewegingen in CO_2 op superkritieke drukken met inhomogene temperatuursverdelingen in beeld te brengen.

De experimenten laten zien dat thermische stratificatie veel sneller optreedt dan verwacht op bij vloeistoffen op lagere drukken. Dit gevolgen van de thermische stratificatie op de stroming blijken daarbij sterk afhankelijk van de verwarmingsrichting. Bij verwarming van onderaf ontstaat een instabiele stratificatie, waarbij opwaartse krachten secundaire stromingen veroorzaken die de warmteoverdracht verbeteren. Deze warmteoverdrachtsverbetering werkt de verbetering van de warmteoverdracht door een toename in soortelijke warmte bij de wand in de hand. Bij verwarming van bovenaf leidt de stabiele stratificatie juist tot een afname van de warmteoverdracht, omdat de verticale beweging wordt onderdrukt. Naarmate de drijvingskrachten sterker worden wordt de verbetering van de warmteoverdracht door een toename in warmtecapaciteit vermeerderd tegengewerkt, en neemt de gehele warmteoverdracht uiteindelijk af. De experimenten in dit proefschrift tonen aan dat de warmteoverdracht tussen deze twee configuraties een ordegrote van elkaar kunnen verschillen. In een warmtewisselaar met verwarming aan beide zijden zullen de effecten elkaar beïnvloeden, waarbij de mate van stratificatie aan de bovenzijde (stabiele stratificatie) significanter is dan aan de onderzijde van het kanaal.

Deze studie bevestigt dat superkritische CO_2-stromingen zeer gevoelig zijn voor

opwaartse krachten, die vaak een veel grotere invloed hebben op de warmteover-dracht dan andere variaties in materiaaleigenschappen. De huidige resultaten helpen bij het verbeteren van numerieke modellen en verklaren eerdere tegenstrijdige experimentele bevindingen in de warmteoverdracht van vloeistoffen op superkritieke drukken. Daarmee dragen de huidige resultaten bij aan het verbeteren van modellen die de stroming en de warmteoverdracht van superkritieke vloeistoffen omschrijven, nodig voor het ontwerp van efficiëntere warmtewisselaars en betrouwbaardere superkritische energieconversiesystemen. Daarmee ondersteunt dit onderzoek de verduurzaming van industriële warmte en elektriciteitsproductie.

Contents

Chapter 1

Introduction

At supercritical pressures, the distinction between liquid and gas disappears, and fluids behave in ways we are not accustomed to. This unique thermodynamic behavior creates new possibilities for cleaner and potentially sustainable heat and power production. However, it also introduces numerous new challenges for engineers, who must navigate the complex behavior of supercritical fluids to unlock their full potential.

1

1.1   Motivation

Since the industrial revolution, fossil fuels have been the main facilitator of human progress, shaping modern society with their high energy density, versatility, and ease of use. Where they are abundant, they have acted as catalysts for economic growth and human development (EEA, 2015). However, the consequences of their widespread use have become increasingly evident in recent decades. The use of fossil fuels releases greenhouse gases, driving more frequent and intense climate events and contributing to a steady rise in global temperatures since the 1980s (NASA, 2024), with the latest year, 2024, being the warmest year recorded in modern history (WMO, 2025). If these trends persist, we face worsening droughts and wildfires, rising sea levels, the loss of habitable land, and the extinction of numerous species (EC, 2025a).

The growing risks associated with climate change place increasing pressure on governments to enact mitigation policies. However, global climate action is often hindered by shifting political priorities, economic constraints, and geopolitical tensions. This instability can lead to inconsistent commitments, as demonstrated by the recent withdrawal of the world's second-largest emitter from the most significant international climate agreement (BBC, 2025). Given that political will alone has proven insufficient to ensure long-term decarbonization efforts, a fundamental shift is needed: sustainable energy alternatives must become not only viable but also economically and technically superior to fossil-based systems. Without competitive alternatives that offer clear advantages, transitions will remain vulnerable to policy reversals, delaying urgent climate action.

Nearly half of all energy consumption globally is dedicated to heat (IEA, 2019), making it a key area for emissions reduction. Electrification, particularly of heating, has been identified as the primary strategy for decarbonizing thermal energy and meeting the Paris agreement targets (UNCC, 2015). While the share of heat generated using renewable electricity and heat pumps is steadily increasing (IEA, 2019), most of this growth is concentrated in domestic and space heating applications (IEA, 2022), where output temperatures remain well below 100°C. In contrast, the adoption of heat pumps for industrial processes such as those in the paper, food, and chemical industries remains significantly slower, particularly for applications requiring temperatures above 100°C (IRENA, 2023). At these higher temperature levels, where large temperature lifts are necessary, the efficiency of conventional heat pumps declines sharply, posing a major challenge for industrial heat decarbonization (IEA, 2022).

To efficiently upgrade heat for high-temperature industrial processes that are not yet heated by heat pumps, the operating pressures of heat pump designs are partially being raised to beyond the critical point of their working fluid. A practical implementation
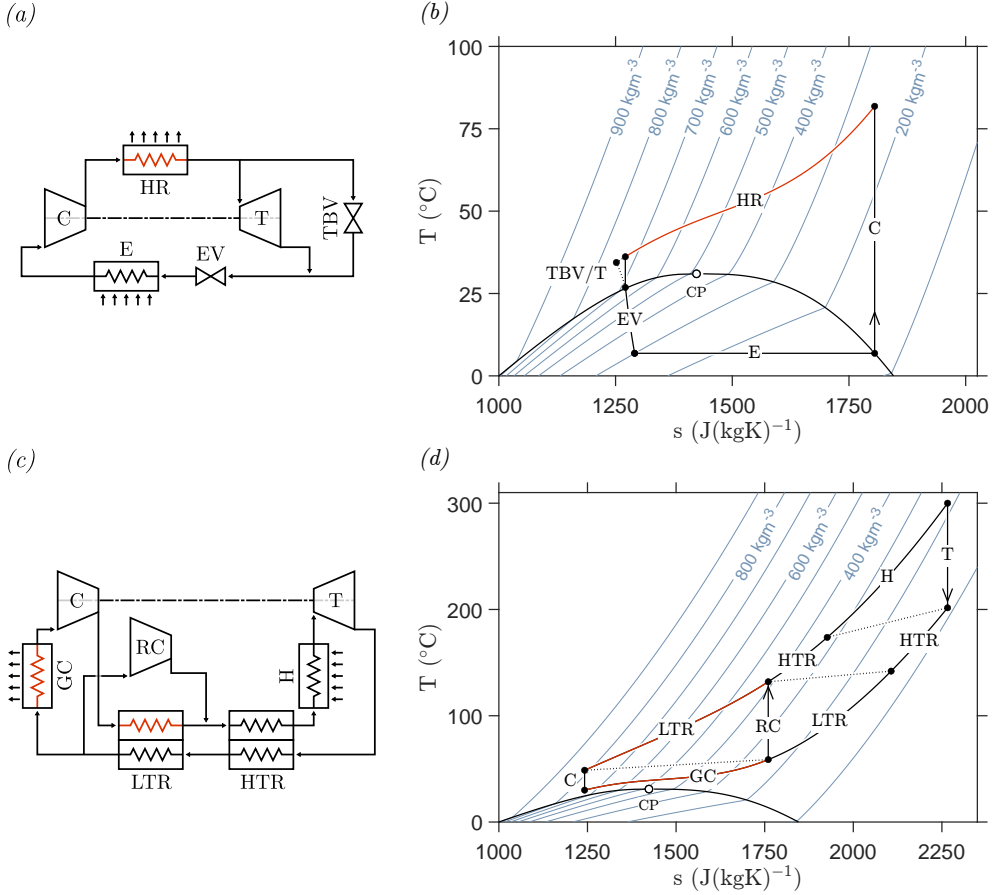
Figure 1.1: Two promising supercritical CO_2 energy conversion systems. *(a)* shows a trans-critical heat pump (Wolscht et al., 2023, 2024), in which turbine (T) can be bypassed with turbine bypass valve (TBV). Furthermore, the subfigure indicates the compressor (C), the expansion valve (EV), the evaporator (E) and the heat rejector (HR). The T-s diagram of the trans-critical heat pump is shown in *(b)*. *(c)* shows a supercritical pressure recompression Brayton cycle (Crespi et al., 2017), the T-s diagram of which is shown in *(d)*. Both subfigures indicate the compressor (C), the turbine (T), the re-compressor (RC), the heater (H), the gas cooler (GC), the low-temperature recuperator (LTR) and the high-temperature recuperator (HTR). Both T-s diagrams show several isochors and the vapour-liquid critical point, CP. Moreover, the T-s diagrams assume negligible internal losses.

of one such transcritical heat pump, as shown in figures 1.1(a) and 1.1(b), has been proposed by Wolscht et al. (2023, 2024). Given the high density and heat capacity of the supercritical fluid at the thermodynamic conditions of the cycle, the heat pump shown in figures 1.1(a) and 1.1(b) can upgrade large heat flow rates with a relatively compact system (Austin and Sumathy, 2011). Moreover, transcritical heat pumps can achieve larger temperature increases than systems with subcritical working fluids (Austin and Sumathy, 2011; Ma et al., 2013; Adamson et al., 2022). As a result, they can efficiently upgrade heat from low-temperature renewable sources for district heating systems (Wolscht et al., 2023, 2024). Additionally, when operating at compressor outlet pressures above 100 bar (with carbon dioxide as the working fluid), transcritical heat pumps can achieve heat rejection temperatures beyond 100°C. Their supercritical pressure heat rejection temperature profiles align particularly well with heating processes that require sensible heat, making them especially suitable for air heating applications such as industrial drying in the paper and food industries (Zhao et al., 2024). When powered by a sustainable electricity source, transcritical heat pumps enable the defossilization of the heating of these processes.

Besides the potential defossilization of industrial heat, supercritical pressure energy conversion systems offer opportunities to further decarbonize electricity production. While the share of electricity from renewable sources is steadily increasing — reaching 39% in Europe in 2025 (EC, 2025b) — the global electricity demand continues to rise (IEA, 2024), driven in part by the electrification of previously fossil-fueled processes. As such, there is a growing need for reliable power sources that are less volatile and intermittent than wind and solar energy, helping to replace natural gas power systems. Many low and intermediate temperature heat sources have so far been unsuitable for efficient conversion into electricity using subcritical pressure energy cycles. To overcome this limitation, supercritical thermal energy conversion systems have been proposed. These systems promise to convert thermal energy across a broad temperature range with high thermal efficiencies (Liao et al., 2019), while also enabling compact designs due to the high power densities of their working fluids. A schematic of one such cycle is shown in the bottom half of figure 1.1. Among these, the recompression cycle, illustrated in figures 1.1(c) and 1.1(d), is one of the most extensively studied supercritical pressure cycle configurations for the sustainable generation of power (Angelino, 1968; Dostal et al., 2006; Wang et al., 2014a; Crespi et al., 2017). Adaptations of this cycle have been proposed for a range of heat sources that were previously not considered for large-scale power generation, including concentrated solar heat (Turchi et al., 2013; Garg et al., 2013; Dunham and Iverson, 2014; Osorio et al., 2016), nuclear heat (Ahn et al., 2015; Guo et al., 2018), and even waste heat (Wright et al., 2016; Marchionni et al., 2020). Since these heat

sources are not derived from fossil fuels, supercritical power cycles have the potential to meet the growing demand for electricity in a sustainable manner.

Supercritical pressure energy conversion systems have most commonly been designed to employ carbon dioxide as their working fluid. As carbon dioxide is inert, non-flammable and thermally stable, it is often favored over organic compounds and refrigerants with critical points at more accessible pressures. Furthermore, the relatively low critical temperature of CO_2 in comparison to most other inorganic fluids makes it attractive for applications at intermediate temperatures, such as potentially sustainable power cycles in particular. It is therefore that from here onwards the discussion on fluids at supercritical pressures is limited to only CO_2 in the current manuscript. While this thesis focuses exclusively on CO_2, research on fluids at supercritical pressure extends beyond it. Various fluids are considered in the broader literature, with applications extending past those mentioned in this work (Brunner, 2010).

1.2 Non-ideality at supercritical pressures

Whereas energy conversion systems at supercritical pressures are promising candidates for the sustainable generation of heat and power, their practical implementation is challenged by the complexity of the thermodynamic region in which they operate. The non-ideality of the thermodynamic region can be highlighted by considering a process in which the temperature of a fluid is increased for a constant pressure. Figure 1.2 compares the heating of subcritical carbon dioxide to the heating of CO_2 at a supercritical pressure. Beyond the vapour-liquid critical point, a fluid no longer undergoes a discrete phase transition from liquid to gas at a given boiling temperature T_B when it is heated. Instead, fluids undergo a boiling-like process during which they remain in a continuous phase. Over the span of a finite temperature range, the thermodynamic properties of the fluids transition from their liquid to their gas values. The non-linear variations in thermodynamic properties that fluids exhibit during this pseudo-boiling process can be considerable. The thermophysical gradients are most pronounced near the pseudo-critical temperature T_{pc}, defined at the temperature where the specific isobaric heat capacity has its maximum along a supercritical isobar (Banuti, 2015). The span of pseudo-critical temperatures shapes the pseudo-critical curve (p-c curve), a quasi-extension of the vapour-liquid coexistence curve into the supercritical domain. The location of the p-c curve in the phase-diagram and the evolution of several thermodynamic quantities in its vicinity are shown in figure 1.3. As apparent from the figure, the variation in properties is the largest for near-critical pressures. As the pressure is increased further, the thermophysical gradients decrease
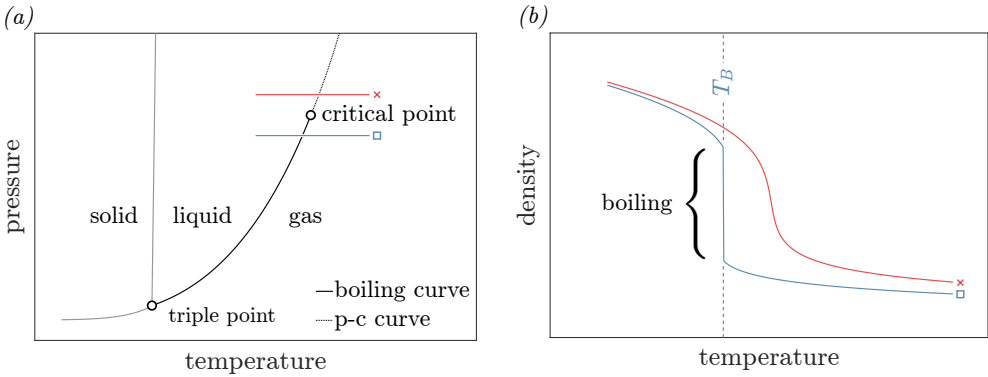
Figure 1.2: The disappearance of a discrete phase transition at supercritical pressures. *(a)* shows the phase diagram of carbon dioxide, in which the temperature of the CO_2 is increased along a constant subcritical (blue, □) and a supercritical (red, ×) pressure. *(b)* shows the evolution of the CO_2 density for both processes.

gradually.

Due to the large thermophysical variations that can be induced in systems with supercritical working fluids, their flow behavior differs considerably from that of subcritical single-phase fluid flow systems. In supercritical fluid flows with temperature variations, the assumptions underlying conventional single-phase flow models break down. However, designing compressors, heat exchangers, and turbines that operate in this thermodynamic regime requires a thorough understanding of fluid behavior under these conditions, along with accurate models to reliably predict turbulent heat transfer and pressure losses. As such, these models are essential for developing sustainable energy conversion systems that operate safely and perform as expected. In recent years, various aspects of supercritical pressure flows have been modeled, including their hydrodynamic stability (Ren et al., 2019a,b; Bugeat et al., 2024; Boldini et al., 2024a,b), the modulation of their turbulence by property variations (Patel et al., 2015, 2016; Pecnik and Patel, 2017; Hasan et al., 2023; Hasan and Pecnik, 2024), and their viscous losses (Fang et al., 2012; Ehsan et al., 2018; Fang et al., 2020).

1.3   Challenges in heat transfer & buoyancy

Thermophysical property variations also strongly affect the heat transfer within heat exchangers. Several of the heat exchangers of supercritical energy conversion cycles operate in the near vicinity of the pseudo-critical curve, where large property variations manifest. For the two energy systems shown in figure 1.1, the processes within these
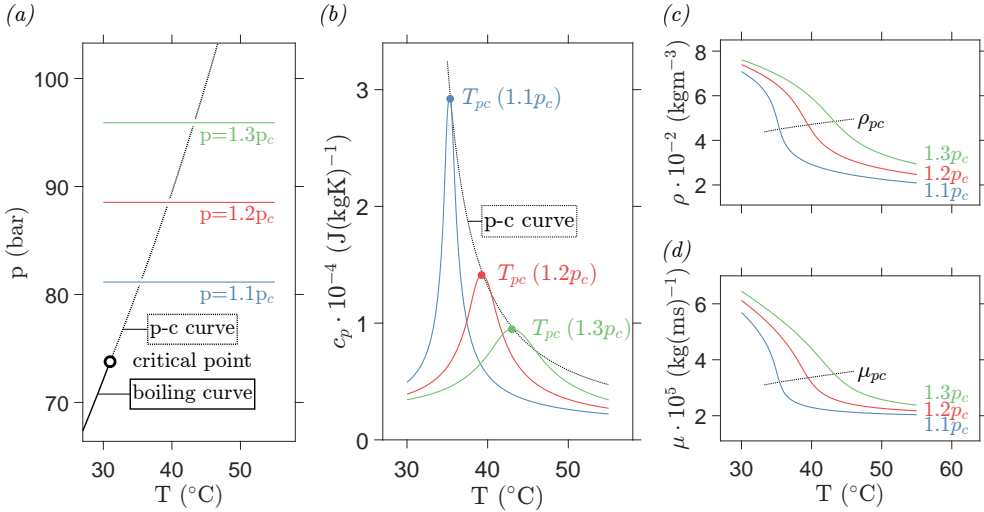
Figure 1.3: Thermodynamic properties of carbon dioxide at several supercritical pressures, for which the critical temperature and pressure are at $T_c = 31.0°C$ and $p_c = 73.8$ bar, respectively. *(b)* shows the isobaric heat capacity c_p along the isobars that are indicated in the phase diagram in *(a)*. The pseudo-critical (p-c) curve is defined at the local maxima of c_p along an isobar (Banuti, 2015). Distributions of density ρ and viscosity μ for the current isobars are shown in *(c)*, respectively.

near-pseudo-critical heat exchangers are shown in red. Within the high-pressure side of the low-temperature recuperator, the gas cooler and the heat rejector, a large density span is traversed with an effectively single-phase fluid. To predict the heat transfer within these particular heat exchangers, many new empirical models have been proposed in recent years (Pitla et al., 1998; Pioro et al., 2004; Yoo, 2013; Huang et al., 2016; Cabeza et al., 2017; Ehsan et al., 2018; Bodkha and Maheshwari, 2021; Lopes et al., 2022; Wang et al., 2023a). As highlighted in the review by Wang et al. (2023a) on supercritical pressure heat transfer, the proposed heat transfer coefficients exhibit substantial variation, particularly near the pseudo-critical curve. In this region, reported heat transfer coefficients can be up to an order of magnitude higher or lower than the corresponding constant-property coefficients (Wang et al., 2023a). As discussed in the paragraph hereafter, this variability is likely driven by buoyant effects within the heat exchangers.

Flows of fluids at supercritical pressures are readily susceptible to substantial buoyant forces. As shown earlier, when a fluid at supercritical pressure is heated in the vicinity of the pseudo-boiling point, its density decreases sharply over a narrow temperature
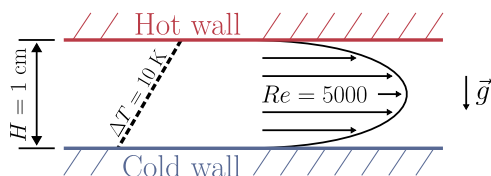
Figure 1.4: Fictional flow and heating configuration for figure 1.5. A single plate heat exchanger channel is considered, in which a hydrodynamically developed horizontal flow with a constant Reynolds number and channel height is differentially heated in the vertical direction.

range. As a result, regions of fluid with significantly different densities—a heavier and a lighter one—can coexist in close proximity, inducing strong buoyancy forces. To illustrate the prevalence of buoyancy in supercritical flow systems, a fictional flow configuration is considered in figure 1.4, representative of the flow within a plate heat exchanger channel. In the considered channel, a hydrodynamically developed flow is differentially heated. The height of the cavity, the temperature difference between the top and bottom constant temperature surfaces, the direction of gravity, and the Reynolds number are imposed. In figure 1.5, the Richardson number - a dimensionless measure of natural convection with respect to forced convection - of the configuration described in figure 1.4 is presented for several working fluids. More specifically, the value of Ri is shown for water and air at atmospheric conditions, and compared to the value of Ri for CO_2 at the conditions of the three most non-ideal heat exchangers in figure 1.1: the low-temperature recuperator, the gas cooler or the heat rejector. The value of Ri for CO_2 within the specified heat exchangers exceeds that of the considered subcritical fluids by several (> 3) orders of magnitude. As such, the magnitude of buoyancy-driven effects in heated flows at supercritical pressures far exceed those in subcritical flows with the same heating rates and length scales. As a result, even in heat exchangers where buoyancy is negligible under subcritical single-phase conditions, buoyancy can significantly influence —or even dominate— flows at supercritical pressures. These buoyancy-dominated flows are highly prone to thermal stratification, making heat transfer dependent on both the flow direction and the direction of the heat transfer. With respect to a neutrally buoyant flow, buoyancy either strongly aids or opposes heat transfer. Consequently, heat transfer coefficients lose their generality, and no single coefficient can predict heat transfer behavior across all configurations, unlike in flows where buoyancy is negligible. This has driven the development of numerous new correlations to better capture heat transfer behavior in different settings.
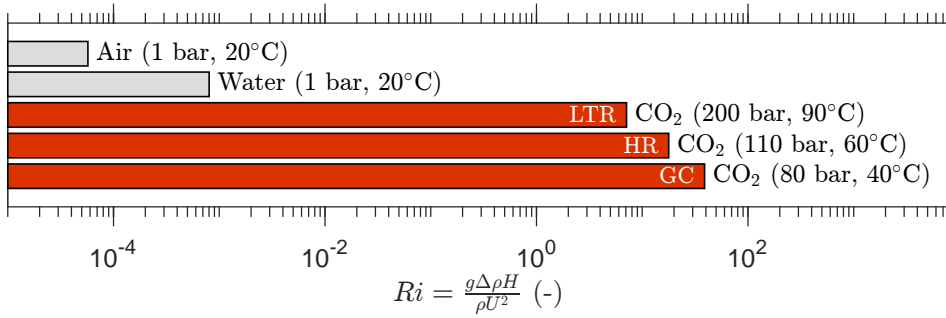
Figure 1.5: Relative buoyant contributions for the heat transfer configuration shown in figure 1.4. In the current figure, the values of *Ri* for (subcritical) air and water at atmospheric conditions are compared to the supercritical thermodynamic conditions of the three heat exchange processes (LTR, HR and GC) that are indicated in red in figure 1.1.

1.4   Scope of work

In this thesis, the modulation of heat transfer in flows of a fluid at supercritical pressures by buoyancy is investigated. This work is motivated by the development of near-pseudo-critical heat exchangers for energy conversion systems, which operate under highly non-ideal thermodynamic conditions where conventional models for subcritical single-phase heat transfer break down. Despite significant previous research efforts to characterize heat transfer at supercritical pressures, the presented models prove to be highly specific to particular flow directions and configurations. The considerable variations between these models have often been attributed to the influence of buoyancy, yet a comprehensive understanding of its manifestation in a fluid with substantial non-ideal property variations is still lacking, especially in an experimental context.

The objective of this thesis is to experimentally elucidate the mechanisms by which buoyancy affects the flow and turbulence characteristics of supercritical pressure CO_2. In doing so, the aim is to determine the implications of these buoyancy effects on heat transfer. In particular, the horizontal flow within a (plate) heat exchanger channel is considered, as it is for this configuration where the contrast in the modulation of the flow by buoyancy between different heating configurations is most pronounced.

To facilitate this study, a new experimental setup has been designed and constructed, as described in detail in this work. The following sections highlight two key features of this facility. First, it enables optical measurements, allowing for the first experimental analysis of supercritical fluid flow under heat transfer. This capability addresses a

long-standing need for optical experiments to validate modeling trends in supercritical fluids, as notably emphasized by Yoo (2013). Second, the facility operates with a natural circulation-driven flow of supercritical pressure carbon dioxide, providing a stable base flow for investigating buoyancy effects under controlled conditions.

1.4.1   Optical experiments

Existing experimental studies on the heat transfer of supercritical CO_2 have largely been limited to wall temperature measurements, constrained by finite probe size and well dimensions. While the spatial resolution of thermal measurements can be improved using infrared imaging techniques, the thermal response time remains a limiting factor due to the thermal inertia of the measured surface. Consequently, these surface temperature measurements have a limited ability to capture transient phenomena within the fluid.

In this work, these limitations are overcome by conducting optical flow investigations concurrently with physical heat transfer measurements. Specifically, optical methods are considered that exploit the large variations in refractive index of the non-ideal operating fluid to generate shadow patterns that reveal thermal variability and, by extension, fluid motion. These optical measurements serve to support and clarify the observed trends in heat transfer behavior. Unlike surface temperature measurement techniques, the considered optical methods are not restricted by physical constraints that limit temporal resolution and, crucially, enable direct probing and observation of fluid behavior. This approach allows us to capture local and highly transient fluid behavior during heat exchange with supercritical CO_2, revealing buoyancy-induced phenomena that previous experimental studies could only infer indirectly.

1.4.2   Natural circulation

To drive the flow for the current heat transfer and mixed convection experiments, natural circulation has been employed in this work. This approach exploits the significant density gradients in supercritical carbon dioxide by differentially heating the two vertical legs of a closed flow loop, thereby inducing a sustained flow. Natural circulation offers several advantages over forced convection. Notably, it eliminates the need for a mechanical pump, which could introduce vibrations and noise, potentially interfering with sensitive measurements. By extension, it also circumvents the challenges associated with sealing high-pressure rotary and reciprocating systems, a challenge particularly pronounced with supercritical fluids. Most critically, it eliminates the need for pump lubricants, which could dissolve into the carbon dioxide and limit its optical accessibility during investigations.

While natural circulation alleviates some mechanical complexities in circulating su-
percritical CO_2, its implementation introduces distinct challenges. Unlike forced con-
vection systems, the steady-state mass flow rate in a natural circulation loop (NCL)
with a supercritical working fluid is not inherently well-defined (Swapnalee et al.,
2012; Liu et al., 2019). Moreover, these systems are modeled to be highly susceptible
to dynamic instabilities, often characterized by thermal oscillations (Wang et al., 2024;
Rai et al., 2025). Such instabilities can lead to thermal fatigue, posing significant
risks under the current high-pressure conditions. To address these challenges, this
thesis first investigates and characterizes the steady-state performance of the NCL.
Subsequently, the stability boundaries of the NCL are experimentally examined to
ensure reliable operation during mixed convection experiments.

1.5 Thesis outline

The remainder of this thesis is structured as follows. CHAPTER 2 provides a detailed
description of experimental facility developed to investigate mixed convection in
supercritical pressure CO_2. This chapter elaborates on the design considerations of
the facility, both concerning the design of the test section for the optical measurements
and the design of the loop within which CO_2 is circulated naturally. CHAPTERS 3 and
4 focus on the natural circulation within the experimental setup. CHAPTER 3 presents
an experimental evaluation and characterization of the steady-state behavior of the
Natural Circulation Loop (NCL), with an emphasis on its performance under various
operational conditions. CHAPTER 4 investigates the stability limits of the NCL to
ensure the reliable and stable circulation of CO_2 throughout the mixed convection
experiments. CHAPTER 5 examines the heat transfer characteristics of horizontal
supercritical CO_2 flows, particularly the influence of buoyancy forces on heat transfer.
The chapter discusses experimental heat transfer results and supports observed trends
with optical investigations of the fluid motion, offering insights into the underlying
flow dynamics. Finally, CHAPTER 6 concludes the thesis by summarizing the key
findings and discussing their implications on the heat transfer in supercritical pressure
energy conversion systems.

1

Chapter 2

Experimental facility

At first glance, stripped of context, the current experimental setup appears deceptively simple: just a few pipes connected to a metal box with windows in it. Yet, through its careful design, it enables the observation of phenomena that have not been previously explored in experiment. Such is the nature of experimental research — where progress is not necessarily dictated by the appearance, size, or cost of the apparatus, but by the insights it reveals.

2.1 Experimental facility

In this thesis, the mixed convection of supercritical pressure carbon dioxide is investigated to assess the influence of buoyancy on heat transfer, to enhance our understanding of supercritical pressure heat exchange and its role in sustainable heat and power conversion systems. To enable this study, a novel experimental facility has been designed and constructed. At its core is a high-pressure test section that provides optical access to the supercritical carbon dioxide, enabling optical investigations of its flow. The test section is integrated into a natural circulation loop, where buoyancy forces drive passive flow circulation.

This chapter provides an overview of the experimental facility. Section 2.2 introduces the natural circulation loop in its initial configuration, before the integration of the optical test section. Section 2.3 then discusses the test section and its incorporation into the loop. Finally, Section 2.4 details the instrumentation used in the facility and the uncertainty propagation associated with the measured data.

2.2 Flow circulation loop

2.2.1 Natural circulation

For chapters 3 and 4 of this thesis, the test section is not integrated into the natural circulation loop, and only the natural circulation loop is considered. Figure 2.1 presents a schematic of the NCL used in these chapters, where the test section is explicitly excluded. In this figure, the main NCL is highlighted with a thick black closed line. The dimensions of the flow loop and the range of conditions within which

parameter	& description	value	unit
H	natural circulation loop height	4	m
L	natural circulation loop length	10	m
D	loop internal diameter	21.1	mm
Δz	driving height	≤ 2.5	m
p_d	design pressure	140	bar
T_d	design temperature	65	°C

Table 2.1: Description of the natural circulation loop. The table gives the values of the parameters indicated in figure 2.1.
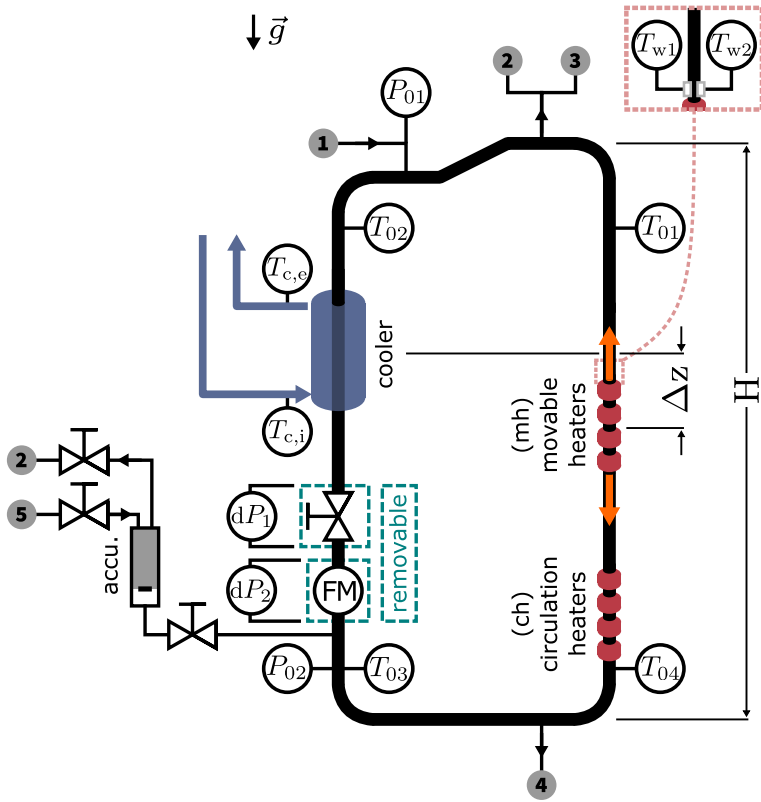
Figure 2.1: Schematic of the current natural circulation loop (NCL). The main flow loop is indicated with a thick black line. The system is connected to ① a CO_2 bottle with a dip tube, ② a purge that is connected to the laboratory's gas vent system, ③ a vacuum pump, ④ a drain, and ⑤ a nitrogen bottle. The electric heating elements and the annular cooler are indicated in red and blue, respectively. The top-most electric heaters (labelled *mh*) can be translated vertically. All removable elements are outlined with a green dotted line. Temperature-, absolute pressure- and mass flow rate transmitters are indicated with T_{0x}, P_{0x} and FM, respectively.

it has been designed to operate are specified in table 2.1.

The system is characterized by a closed stainless steel piping loop spanning a vertical height of 4 meters. This height was deliberately chosen to mitigate transient effects and instabilities, which have been predicted to manifest in natural circulation systems at supercritical pressures (Wang et al., 2024; Rai et al., 2025). To approximate the system's response to these instabilities, a one-dimensional compressible model was

developed for this work, though it is not discussed in this thesis. In qualitative agreement with a linearized approach by (Debrah et al., 2013), the model predicts that oscillations are only induced when the driving height, Δz in figure 2.1, falls below a certain threshold, which depends on the thermodynamic conditions of the loop. Consequently, the experimental facility was designed to maximize the driving height within the constraints of the available lab space, ensuring steady and stable circulation when necessary.

The circulation of carbon dioxide in the loop is driven by buoyancy forces arising from differential heat exchange along a vertical span. One vertical leg of the NCL is cooled using a tube-in-tube counter-current heat exchanger with baffles on the coolant side, depicted in blue in the top left of figure 2.1. The inlet temperature of the cooler is controlled using a Julabo FP51-Sl refrigerated circulator. Heat is supplied to the opposite vertical leg via two sets of electric band heaters. The lower heater set (labelled *ch* in figure 2.1) is used to provide a steady base flow, delivering up to 1500 W of heating from a fixed vertical position. The top-most set of heaters (labelled *mv*) is used to drive the system to an oscillatory state. The six electric band heaters (up to 11.1 W/cm^2) are clamped to the system at fixed intervals and can be manually repositioned along the vertical riser between measurements to vary the natural driving height Δz of the NCL and provide up to 2100 W of heating in total. Since natural circulation is driven by density differences over Δz, altering the heater position directly affects the mean mass flow rate of the system. The sensitivity of the mass flow rate to Δz is examined in detail in Chapter 3. Conversely, the mass flow rate can also be controlled by adjusting the flow resistance of the regulating valve in the cold section of the loop. To eliminate this resistance entirely, the valve can be removed from the NCL.

As all heat exchangers are positioned along the vertical sections of the loop, the vertical line symmetry of the system is broken. As a result, a preferential counter-clockwise flow direction prevails for the perspective of figure 2.1.

The system is primarily assembled using detachable stainless steel tube fittings. However, where non-metallic soft seals are required, EPDM or PTFE components are used Ansaloni et al. (2020). Moreover, to minimize heat losses to the surroundings, the circulation loop is insulated with a 40 mm thick annulus of rockwool.

2.2.2 Initial pressurization

To fill the loop, the system is initially pressurized to a moderate level (approximately 5–10 bar) using carbon dioxide from a supply bottle connected at ① in Figure 2.1. A blow-off valve ② at the top of the loop is then used to purge non-condensable gases, while a valve ④ at the bottom is thereafter opened to drain any unwanted liquids.
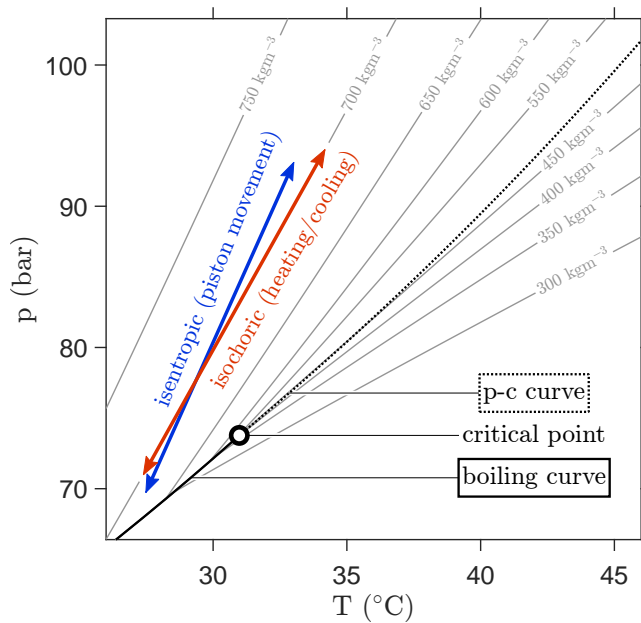
Figure 2.2: Modes of modulation of the thermodynamic state of the system. During normal operation, the system operates with a constant volume. Under such conditions, any imbalance in heat induces movement of the mean thermodynamic state along a set isochor, as indicated with the red arrow. Any movement of the piston within the accumulator, if connected to the main loop, induces the compression or expansion of the CO_2. The consequent changes in thermodynamic state are indicated in blue if this process is isentropic.

Once this initial purging is complete, the system is evacuated using a vacuum pump connected via line ③. High-purity liquid carbon dioxide is then fed to the NCL from a dip-tube-equipped vessel, in which CO_2 is at its vapor pressure for the ambient temperature at equilibrium. Once an equilibrium in pressure is reached between the bottle and the experimental facility, the loop is cooled. As a result, the loop pressure decreases to below the vapor pressure of the bottle, resulting in a flow of carbon dioxide towards the facility. To accelerate the filling process, the loop is moderately heated during cooling, generating a natural circulation that enhances the cooling rate. By weighing the supply bottle, the exact filling mass of the loop is determined.

2.2.3   Modulation of thermodynamic state

The supercritical thermodynamic region of CO_2 in the NCL is explored through either isochoric or isentropic processes, as illustrated in Fig. 2.2. Isochoric operation is achieved by disconnecting the accumulator, whereby the volume and the contained mass of CO_2 determine the isochor. Any heat imbalance, caused by changes in heating power or coolant temperature, shifts the thermodynamic state of the system towards a new equilibrium along an isochor, as shown by the red arrow in Fig. 2.2. Conversely, when the piston accumulator is connected, altering the nitrogen charge compresses or expands the CO_2 in the system. If these changes are adiabatic and with negligible viscous losses, they result in isentropic shifts in the thermodynamic state, as indicated by the blue arrow in Fig. 2.2.

2.3   Test section & optics

2.3.1   Test section

To optically investigate the flow of supercritical carbon dioxide and its heat transfer response, a high-pressure stainless steel test section is placed at the bottom horizontal leg of the natural circulation loop. The placement of the test section within the natural circulation loop is indicated in the top-left of figure 2.3. An image of the apparatus, outlined in blue, is shown in the top-right of figure 2.3. The internal dimensions of the test section are indicated in table 2.1.

The test section provides bi-lateral optical access to a flow channel through two 40 mm thick tempered obround borosilicate visors, as shown in cross-section **B** of figure 2.3. A key feature of the test section is its modularity, allowing easy interchangeability of the internal flow path. This flexibility enables the investigation of multiple flow configurations. To study hydrodynamically developed flows, the CO_2 is directed through a rectangular flow channel. Under the current operating conditions and flow rates (specified later in chapter 5), the flow within this channel is expected to fully develop before reaching the visors, after a length $L_{s,0}$. Alternatively, the internal flow path can be reconfigured to study developing flows. In this configuration, CO_2 first passes through a honeycomb and a set of wire meshes within a settling chamber (Mehta and Bradshaw, 1979; Reshotko et al., 1997; Tropea et al., 2007; Cattafesta et al., 2010), followed by acceleration through a two-dimensional asymmetric contraction designed to mitigate secondary flows induced by wall curvature. However, preliminary investigations revealed that at the mass flow rates required to study the stability of a developing flow, the current optical setup provided limited insights into the flow dynamics of the CO_2. Consequently, only the hydrodynamically developed flow
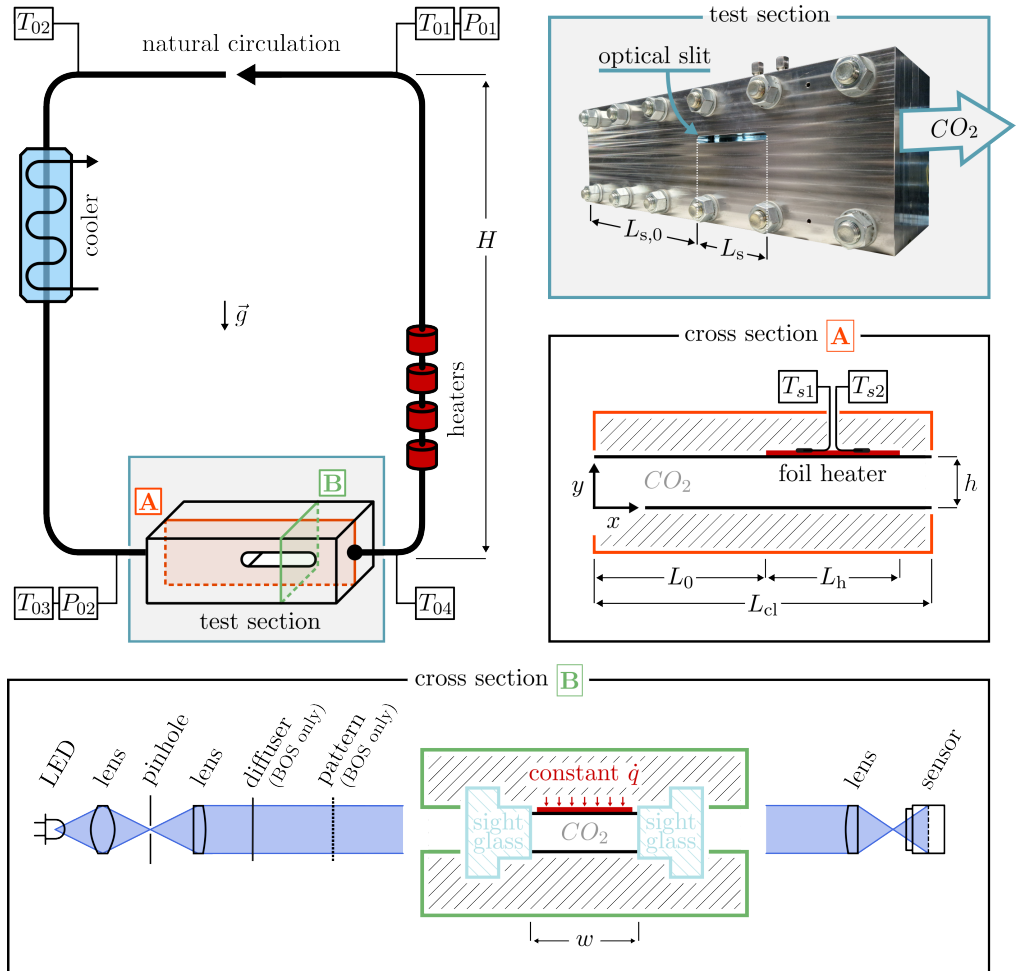
Figure 2.3: Schematic of the current experimental facility, in which carbon dioxide at supercritical pressures is naturally circulated to a test section that is bi-laterally optically accessible. An image of the test section is outlined in blue. In the image, any usually present thermal insulation (30 mm polyethylene foam) has been removed. A schematic of lateral cross section **A** is outlined in orange. In order to change the direction of the heating with respect to the schematic, the test section is inverted. The current optical configuration is shown alongside green-outlined cross section **B**. Any symbols in the figure are explained in the main text, and in table 2.1.

configuration is used for the experimental analysis presented in this thesis.

In the figure, cross section **A** shows the side-view of the current flow path - a rectangular channel - between two gradual round-to-rectangular reducers. The reducers connect the channel to the round pipe-connections of the experimental facility. The top surface of the rectangular channel is heated after a length L_0. For the current conditions and flow rates (specified later in chapter 5), the flow within the channel is expected to fully develop before it is heated. Consequently, the internal geometry of the test section facilitates studies on the development of mixed stratification in hydrodynamically developed channel flows. In order to apply heat from the opposite, bottom surface, the test section is flipped in its entirety. However, in the flipped, bottom-up heating configuration the origin of the considered coordinate system remains on the bottom surface of the test section, consistent with cross section **A** of figure 2.3. The heating is provided by a self-adhesive 40 W polyimide foil resistance heater that spans the full width of the channel. In order to avoid a forward facing step of the surface, the foil heater is bonded to the rear side of a removable surface plate that spans the full top surface, as indicated using the top black line in cross section **A** of figure 2.3. The surface plate, a 0.8mm thick polished aluminium surface mirror, is oriented towards the carbon dioxide with its polished side. The rear-side surface temperature of the foil heater is measured using two K-type thermocouple probes, mounted in the lateral middle of the channel at different streamwise locations, as indicated with T_{s1} and T_{s2} in cross section **A** of figure 2.3. The thermocouple probes are embedded in a small cavity behind the aluminium plate, and therefore do not directly capture the near-wall temperature of the carbon dioxide. Instead, sensors T_{s1} and T_{s2} reflect the thermal response of the heater itself. Given the high thermal resistance between the cavity and the surroundings, nearly all of the heat imposed by the heaters is expected to be transferred to the working fluid.

2.3.2   Optical configuration

In this thesis, two distinct optical techniques are employed to observe the behavior of supercritical pressure CO_2. Both methods, described in the following paragraphs, visualize flow motion by exploiting variations in the refractive index of carbon dioxide.

2.3.2.1   Shadowgraphy

A parallel-light shadowgraphy configuration is used to yield shadowgrams, as is shown schematically in cross section **B** of figure 2.3. The object plane for the shadowgraphy is at the right channel surface in the figure. The brightness of the resulting shadowgram varies proportionally to the second spatial derivative of the path-integrated

parameter & description		value	unit
h	channel height	7.5	mm
w	channel width	50	mm
L_{cl}	inter-reducer channel length	375	mm
L_0	initial unheated length	300	mm
L_h	heated length	50	mm
$L_{s,0}$	reducer-to-optical slit distance	250	mm
L_s	optical slit length	140	mm

Table 2.2: Description of the experimental facility. The table gives the values of the parameters indicated in figure 2.3.

2

refractive index field (Settles, 2001; Merzkirch, 2012). As the refractive index is proportional to the fluid density (Michels and Hamers, 1937), variations in density of the carbon dioxide can be recorded. In the current setting, the shadowgrams outline the boundaries of depth-integrated thermal structures with consecutive maxima and minima in image brightness. In order to increase the sensitivity of the shadowgrams, to reduce the distortion of shadows, and to reduce geometric blur with respect to non-parallel light shadowgraphy (Settles, 2001), the light source (a monochromatic blue LED with a nominal wavelength of 455 nm) is collimated in the current optical setup. As imperfections in the sight glass surfaces can be perceived in these collimated-light shadowgrams, a spatial digital image filter is applied to the images shown in this work to highlight only the thermal structures of interest. The filter is further elaborated on in appendix 5.A.

A Pixelink PL-D755MU-T CMOS camera (2448×2048 pixels, monochromatic) is used to record images. The exposure time of the sensor is maintained at 20 μs for all shadowgrams. The contrast of the recorded images is stretched to cover the full brightness range. Both the image sensor and the light collimator are traversed in the streamwise direction using synchronised linear traversing stages on either side of the test section to visualize the CO_2 at any position along the optical slit.

2.3.2.2 Background Oriented Schlieren (BOS)

The magnitude of the vertical refractive index gradients across the test section can be evaluated by considering the deformation of a known pattern by the highly property-variant CO_2. In the current Background Oriented Schlieren (BOS) configuration, an in-focus background pattern is placed on the left side of the test section in cross

section **B** of figure 2.3. Here, a computer-generated and known dot pattern printed on a transparent plastic sheet is placed along the optical axis. By placing diffusing glass before the background pattern, the incoming light is decollimated. At the expense of the global image brightness, the diffuse light is found to produce a more homogeneously illuminated and globally sharp image when refractive index gradients are present in the test section channel. When a diffuser is used, the sensor exposure time is increased to 150 μs to provide sufficient illumination. Using the image correlation method previously used for shadow image velocimetry in this work, the apparent deformation $(\Delta x(x, y), \Delta y(x, y))$ of the background pattern in the image plane caused by gradients in refractive index in the test section can be measured. By assuming small deflection angles, the unidirectional, vertical deformation of the background pattern, and the presence of a schlieren object that is homogeneous across the full width of the channel, the path-integrated spatial refractive index gradient $\partial n / \partial y$ can be expressed as

$$\frac{\partial n}{\partial y} = \frac{n_0 \Delta y}{M Z_D w},$$

(2.1)

(Schröder et al., 2009; Raffel, 2015). Here, n_0 is the reference refractive index of the carbon dioxide when it is homogeneous in density. Furthermore, M is the magnification of the optical system, and Z_D is the distance from the middle of the channel to the background pattern. Unfortunately, large density gradients are present throughout the limited field of view of the current setup, and the exact magnitude of the path-integrated density is unknown within the imaged volume. As such, no appropriate set of boundary conditions can be posed for the calculation of a line-of-sight integrated density field for the current configuration (Venkatakrishnan and Meier, 2004). Nevertheless, the current BOS approach can be used for a relative comparison of density gradients in the channel, and for the evaluation of the applicability of particle-based optical diagnostics with the studied fluid.

2.4   Instrumentation

2.4.1   Sensor overview

To continuously monitor the facility, it is equipped with a series of sensors that are indicated throughout figures 2.1 and 2.3. To measure bulk temperatures throughout the natural circulation loop, cylindrical Pt100 thermometers with a 3 mm diameter are radially inserted into the flow. These resistance thermometers, labeled T_{01} - T_{04} in figure 2.3, have a nominal accuracy of $\pm 0.1°C$. A similar arrangement with the same resistance temperature transmitters is used to evaluate the coolant inlet temperature

$T_{c,i}$ and the coolant outlet temperature $T_{c,e}$, respectively. The external pipe surface temperature is measured at two points directly above the movable heaters with sensors T_{w1} and T_{w2}. Likewise, equivalent Pt100 thermometers with a nominal accuracy of $\pm 0.1°C$ are used. Measurements of absolute pressure p are taken using welded STS ATM.1st sensors P_{01} and P_{02}, with a nominal uncertainty of ± 0.16 bar or 0.1%. Thermocouples T_{s1} and T_{s2} yield measurements of the foil heater surface temperature with a nominal uncertainty of $\pm 0.5°C$. The thermocouples are calibrated and the readings are shifted to match the readings of resistance sensor T_{03} *in situ*. The loop also includes a Rheonik RHM08 Coriolis mass flow meter, which has a nominal uncertainty of 0.2%, at up to 0.2 g/s. To quantify viscous losses in the Coriolis meter and the regulating valve (when present in the facility), their pressure drops are measured using two Siemens SITRANS P420 differential pressure transmitters (dP1 and dP2 in figure 2.1). These transmitters have nominal uncertainties of 0.125% or ± 12.5 Pa for the current range. When the mass flow meter is removed from the NCL, the steady state mass flow rate $\dot{m}$ is inferred from the heating rate $\dot{Q}_{imp}$ imposed by the vertically placed heaters in figure 2.1 and the increase in enthalpy $\mathcal{H}$ across the heater, evaluated over the vertical leg of the NCL, i.e.

$$\dot{m} = \frac{\dot{Q}_{imp}}{\mathcal{H}(T_{01}, P_{01}) - \mathcal{H}(T_{04}, P_{02})}. \tag{2.2}$$

The value of $\mathcal{H}$, or any other thermophysical quantity, is interpolated from a table generated using the REFPROP database (Lemmon et al., 2018) for given values of T and p. As found in the experiments of chapter 3, the mass flow rate estimated by equation (2.2) is in close agreement with the readings of a Coriolis mass flow meter (the estimated mass flow rate $\dot{m}_{est}$ exceeded the measured value by $7.1 \pm 4.0\%$) when the system is at a steady state, when the pressure drop over the horizontal sections of the NCL is limited at moderate bulk velocities, and when the loop is insulated with a 40 mm layer of mineral wool to minimize heat losses. During the optical experiments in chapter 5, these conditions are met. As such, the Coriolis mass flow meter is removed to avoid any unnecessary disturbances to the flow during the optical investigations, where equation (2.2) is used to determine the mass flow rate within the NCL.

All transducer data (excluding images) are acquired at up to 10 Hz using an NI cRIO-9074. A LabVIEW user interface was developed to provide real-time visualization of the thermodynamic state and performance of the natural circulation loop, complementing its data acquisition system. The interpolation of tabulated thermodynamic properties enables the live monitoring of various derived quantities.

2.4.2   Uncertainty quantification

The uncertainty of all results shown in this work is evaluated by assuming the independence of the respective quantities measured by the sensors in the system. As a result, the standard deviation of any considered quantity is evaluated from the standard deviations of sensor data used to determine the considered quantity. For instance, the standard deviation $\sigma_{\mathcal{H}}$ for $\mathcal{H}(T, P)$ is obtained using

$$\sigma_{\mathcal{H}} = \left[\left(\frac{\partial \mathcal{H}}{\partial T} \right)^2 \cdot \sigma_{\mathrm{T}}^2 + \left(\frac{\partial \mathcal{H}}{\partial P} \right)^2 \cdot \sigma_{\mathrm{P}}^2 \right]^{1/2} . \qquad (2.3)$$

Here, σ_T and σ_P denote the standard deviations of process measurements T and P, respectively.

Chapter 3

Natural circulation at a supercritical pressure
steady state analysis[1]

Supercritical natural circulation loops (NCLs) are capable of achieving high flow rates, circulating their working fluid in a steady, pulseless manner—an essential feature for critical applications such as nuclear reactor cooling or for sensitive experiments. However, the steady-state mass flow rate of these systems remains insufficiently defined. This chapter explores the steady-state behavior of NCLs at supercritical pressures (80–120 bar) using carbon dioxide (CO_2). Distinct thermodynamic states are reached by traversing a set of isochors. An equation for the prediction of the steady state of NCLs at supercritical pressures is presented, and its performance is assessed using empirical data. Changes of mass flow rate as a result of independent hanges of thermodynamic state, heating rate, driving height and viscous losses are shown to be accurately captured by the proposed equation. Furthermore, close agreement between the predicted and measured mass flow rate is found when the measured equipment losses are taken into account for the comparison. The findings provide valuable insights for the development of safe and efficient supercritical natural circulation systems.

3.1 Introduction

When a flow loop is heated at one of its vertical legs and cooled at the other, a natural convection is induced. The flow- and cooling rates of single phase natural circulation facilities are generally orders of magnitude too small to serve a purpose in most industrial applications. However, if the operating fluid is in a thermodynamically supercritical state, considerable flow rates can be obtained due to strong density variations in the vicinity of the critical point. The flow rates generated with these simple systems can be used in settings in which an otherwise moderate flow rate is required, but where problems stemming from leakages, power outages and mechanical noise associated with forced convective flows need to be avoided. For instance, supercritical fluid NCLs can act as reliable, off-grid cooling solutions for nuclear reactors, in case large heat sinks are present. Additionally, these systems can be used for the passive removal of heat from solar heater assemblies, or for the generation of steady, pulseless flows for sensitive experiments. However, as the properties of supercritical media vary greatly with state, the prediction of the steady state of supercritical NCLs for their potential implementation is not straightforward.

The steady state of supercritical natural circulation loops has previously been investigated using both numerical and experimental approaches. In the literature on numerical studies, a one-dimensional transient model is most commonly used to predict both the steady and unsteady behavior of the considered loops (Sadhu et al., 2018b; Jain and Rizwan-uddin, 2008; Sharma et al., 2010a; Pegallapati et al., 2020), although three-dimensional approaches have also been undertaken (Sarkar and Basu, 2017). The mass flow rate of a natural convection loop is predicted to attain a maximum with varying heating rates (Sadhu et al., 2018b; Jain and Rizwan-uddin, 2008). Furthermore, a rise in mass flow rate is expected with increasing loop heights, and increasing channel diameters (Sadhu et al., 2018b; Sharma et al., 2010a; Sarkar and Basu, 2017). On the contrary, an increase of the loop length is expected to have a limiting effect on the flow rate of the loop (Sarkar and Basu, 2017). The influence of thermodynamic state on the steady behavior of supercritical NCLs is briefly touched upon in (Pegallapati et al., 2020). Here, increases in both the filling mass and the heating rate are predicted to result in an increase in loop pressure and subsequently loop flow rate for the range of considered parameters. Similar conclusions can be drawn from experimental investigations of NCLs with supercritical media. For instance, Tokanai et al. (2010) report an increase in mass flow rate with increasing heating rates. The broader range of results presented in Liu et al. (2016) also show the previously discussed maximum in the mass flow rate with increasing heating. As predicted, an increase in system temperature yields an increase in static pressure at a

set charge (Chen et al., 2013; Sadhu et al., 2018a), and an increase in mass flow rate for the considered parameters in Sadhu et al. (2018a).

The above findings only consider and discuss an NCL's sensitivity to changes in specific parameters. A generalized consideration of all variables that affect the steady state is however needed in aid of the reliable design of future facilities. One such correlation of the flow rate of a liquid-like supercritical carbon dioxide NCL, in terms of Grashof and Prantl numbers, is presented by Yoshikawa et al. (2005). A more elaborate approach is put forward by Swapnalee et al. (2012), following the method of Vijayan and Austregesilo (1994); Vijayan (2002) for single-phase fluids. In their work, an expression for the mass flow rate is derived from the one-dimensional steady state momentum equation. In order to characterize the distribution of density in the equation that follows, the change in loop density has to be expressed as a function of the change in enthalpy in the heater. For this, the relationship between dimensionless density and dimensionless enthalpy introduced Ambrosini and Sharabi (2008) is used. There, the adequate overlap of the dimensionless quantities for a broad range of supercritical pressures makes that a single curve can be used to express the relationship between density and enthalpy. Swapnalee et al. (2012) use three distinct linear fits of the constitutive curve to express an expected change of density for three separate ranges of subcooling. From this, a straightforward equation for the NCL flow rate follows, which can be expressed in terms of a Grashof (Gr_D) and a Reynolds (Re_D) number, both based on the internal pipe diameter. A very similar approach is followed in the work of Liu et al. (2019), where a two-region linear fit of Ambrosini and Sharabi (2008) curve is used to derive an expression for the steady mass flow rate. As the true evolution with state is however continuous, the chosen discrete description of thermodynamic properties is expected to introduce significant errors in the prediction of the flow rate. Additionally, the absence of the characterization of experimental loop minor losses in both works makes that the found relationship between Gr_D and Re_D is configuration specific. As the driving forces are generally limited in comparison with forced convective systems, setup-specific pressure losses in equipment can be expected to considerably reduce the flow rates of NCLs.

A revised equation for the prediction of the steady flow rate of natural circulation loops with supercritical media is proposed in §3.2. Consequently, the formula is experimentally assessed in §3.4, with the experimental methodology described in §3.3. In order to find the causes for possible disagreement between theory and experiment, the contributions of state, heating rate, configuration and pressure losses are independently considered. Finally, a summary of the most important conclusions is presented in §3.5.

3.2 Steady state flow equation

Away from regions with considerable radial temperature gradients, the flow in a NCL is expected to display behavior similar to that of a developed pipe flow. As such, a generalized equation is sought from the mass- and momentum balance of a one-dimensional flow. Here, a pipe of constant internal diameter D and therefore constant area $A_{cs} = \pi D^2/4$ is assumed. Additionally, the viscous heating within the system is assumed to be negligible for the current mass flow rates. A geometry that can be described with figure 3.1 is considered. Here, a heater and a cooler are consecutively placed along a closed flow loop. In the figure, the heater and cooler are indicated with red and blue circles, respectively. The mass- and momentum balance equations for
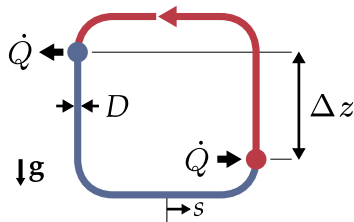
Figure 3.1: Schematic of simplified NCL. The low- and high density sections are indicated in red and blue, respectively. The preferential flow direction is indicated by the red arrow.

the considered system are described as a function of streamwise coordinate s, local density ρ, local pressure p, and mass flow rate $\dot{m}$:

$$\frac{1}{A_{cs}} \frac{d}{ds}(\dot{m}) = 0, \tag{3.1}$$

$$\frac{d}{ds}\left(\frac{1}{A_{cs}^2}\frac{\dot{m}^2}{\rho} + p\right) = \gamma \rho g - \frac{2f}{D}\frac{1}{A_{cs}^2}\frac{\dot{m}^2}{\rho}. \tag{3.2}$$

The coefficient $\gamma(s) \in [-1, 1]$ is used to account for the direction of the gravitational acceleration g with respect to the flow at coordinate s. The rightmost term in equation (3.2) describes viscous losses in the system, using dimensionless Fanning factor f. Given that the mass flow rate $\dot{m}$ is constant at each location, and that $\oint d(1/\rho)$ and $\oint dp$ are zero for a closed loop, the path integral of equation (3.2) reduces to

$$\oint \gamma \rho g \, ds = \frac{2}{D A_{cs}^2} \oint \frac{f \dot{m}^2}{\rho} \, ds. \tag{3.3}$$

The equation above is a force balance with contributions solely from the driving buoyancy and viscous losses in the loop. The system is ultimately driven by the

density difference $\Delta\rho = (\rho_c - \rho_h)$ over the vertical section between the cooler and heater with equivalent length Δz. There, subscripts c and h indicate the the property value at along the cold- and hot leg of the system, respectively. Additionally, Δz is the vertical distance between the cooler and the heater, if they were to be modeled as point sources and point sinks for heat transfer. In reality, a vertical distribution of ρ is found in both heat exchangers. As such, Δz depends on the heat transfer rate, and will attain a value close to the vertical centerline distance. Given the above, equation (3.3) can be rewritten to

$$\Delta\rho g \Delta z A_{cs} = \frac{1}{L} \frac{A_p}{A_{cs}^2} \frac{\dot{m}^2}{2\rho_m} \sum_{i=1}^{n} (f_i L_i), \tag{3.4}$$

where the viscous loss contributions of all sections i are to be summed. Here, the internal wall surface area A_p is expressed using the total loop length L as $A_p = \pi D L$. By linearizing the change in density with varying enthalpy $\mathcal{H}$ at the mean loop temperature $T_m = \int T(s)\mathrm{d}s/L$ and mean loop pressure p_m, and assuming constant pressure in all heat transfer equipment, $\Delta\rho$ can be expressed as a function of a change in enthalpy $(\mathcal{H}_c - \mathcal{H}_h)$:

$$\left.\frac{\partial\rho}{\partial\mathcal{H}}\right|_p (\mathcal{H}_c - \mathcal{H}_h) g\Delta z A_{cs} = \frac{A_p}{A_{cs}^2} \frac{\dot{m}^2}{2\rho_m} \frac{\Sigma (f_i L_i)}{L}. \tag{3.5}$$

Here, subscript m denotes a thermophysical quantity evaluated at T_m and p_m. The linearized expression $\partial\rho/\partial\mathcal{H}|_p (\mathcal{H}_c - \mathcal{H}_h)$ used to describe $\Delta\rho$ introduces an error when a large thermodynamic space with varying $\partial\rho/\partial\mathcal{H}|_p$ is traversed. Qualitatively, $\Delta\rho$ is overestimated as $\partial^2\rho/\partial\mathcal{H}^2|_p$ attains negative values, and $\Delta\rho$ is underestimated when $\partial^2\rho/\partial\mathcal{H}^2|_p$ is positive. As such, $\Delta\rho$ is overpredicted in the liquid-like region and most notably so in the vicinity of the pseudo-boiling curve, whereas it is underpredicted in the gas-like region. Within the considered thermodynamic range, the magnitude of the error remains within [-10,10] % for $|(\mathcal{H}_c - \mathcal{H}_h)|/\mathcal{H}_m \leq 0.25$. Furthermore, the inherent presence of viscous losses makes that the pressure does not remain constant within heat transfer equipment. However, the pressure losses that are generally obtained at the limited mass flow rates that NCLs can generate have a minimal influence on the local density. Instead, the density varies almost exclusively as a result of changes in enthalpy, induced in the heat exchangers of these systems, and evaluating thermodynamic quantities at constant pressure introduces little error to the prediction.

Using the chain rule, the thermodynamic quantity $\partial\rho/\partial\mathcal{H}|_p$ can be rewritten to $-\rho_m\beta_m/c_{p,m}$, where β_m and $c_{p,m}$ are the volumetric expansivity and the specific heat at T_m and p_m, respectively. Lastly, given that the heater enthalpy increase $\Delta\mathcal{H} = (\mathcal{H}_h - \mathcal{H}_c)$ can be expressed as a function of the applied loop heating rate $\dot{Q}$,

i.e. $\Delta\mathcal{H} = \dot{Q}/\dot{m}$, an equation for the steady state flow rate of NCLs at supercritical pressures follows as a function of several design parameters:

$$\dot{m}^3 = \frac{\pi^2 g}{32} \cdot \underbrace{\frac{\rho_m^2 \beta_m}{c_{p,m}}}_{\text{Fluid properties}} \cdot \underbrace{\dot{Q}\Delta z D^5}_{\text{Configuration}} \cdot \underbrace{\frac{1}{\Sigma(f_i L_i)}}_{\text{Viscous losses}} \cdot \tag{3.6}$$

Equation (3.6) expresses expected mass flow rate $\dot{m}$ as a function of a state dependent group of variables, a configuration and geometry specific group, and a viscous loss term. The viscous loss term $\Sigma(f_i L_i)$ accounts for both viscous losses in developed sections, and for additional losses in loop equipment and bends. Equation (3.6) has to be iteratively solved, since the viscous loss term is a function of mass flow rate $\dot{m}$. Furthermore, as the Reynolds numbers for the warm and the cold leg of the system differ at constant $\dot{m}$, their viscous losses have to be solved for independently. The thermodynamic properties of the hot- and cold leg can be found at $\mathcal{H}_{h,c} = \mathcal{H}_m \pm \frac{1}{2}\Delta\mathcal{H}|_p$, respectively. Here, the values of $\mathcal{H}_{h,c}$ follow from the guess for $\dot{m}$.

In order to allow for ease of experimental fitting, equation (3.6) can be rewritten in dimensionless form. For this purpose, dimensionless quantities Gr_D and Re_D are introduced:

$$Gr_D = \frac{\rho_m^2 \beta_m}{c_{p,m}\mu_m^2} \frac{\dot{Q}g D^3}{\dot{m}}, \quad Re_D = \frac{\rho_m U D}{\mu_m}, \tag{3.7}$$

where μ is the dynamic viscosity, and U is the bulk velocity with $U = \dot{m}/(\rho A_{cs})$. Consequently, the Grashof number Gr_D can be expressed as a function of the Reynolds number Re_D:

$$Gr_D = 2\frac{\Sigma(f_i L_i)}{\Delta z} \cdot Re_D^2. \tag{3.8}$$

In case the pressure losses in loop equipment attain negligible magnitudes, and a fanning factor expression of the form $f = a/Re_D^b$ is used where a and b are constants, equation (3.8) reduces to

$$Re_D = \left(\frac{\Delta z}{2aL} \cdot Gr_D\right)^{\frac{1}{2-b}}. \tag{3.9}$$

Despite having different means to generate a driving force with, both natural and forced convective flows are driven by steady pressure gradients. Hence, ideal fluid friction factor models for forced developed pipe flows are considered for the prediction of $\dot{m}$ in this work. As all values of Re_D for the current empirical data lie within $[10^4, 10^5]$, and as the pipe wall surface is hydrodynamically smooth, the simplistic Blasius turbulent friction correlation with constants $a = 0.25$ and $b = 0.0791$ is used for a comparison

Parameter & Description		Value/Range	Unit
$\dot{Q}$	Heating rate	≤ 2	kW
ρ_m	Mass density	$250 \leq \rho_m \leq 750$	$kg\ m^{-3}$
p_m	Operating pressure	$81 \leq p_m \leq 111$	bar
T_m	Operating temperature	$20 \leq T_m \leq 60$	°C

Table 3.1: Operating range

with experimental data (Zigrang and Sylvester, 1985; Taler, 2016). Whilst ideal fluid models perform well when a flow of supercritical carbon dioxide is isothermal (Wang et al., 2014b), they underpredict the viscous losses when radial temperature gradients are present for the current heat transfer configuration, in which an upward flow is heated and a downward flow is cooled. However, as the loop length far exceeds the total length for which heat is exchanged in the current system, the underprediction of friction by the ideal fluid model is expected to be limited for moderate heating rates. Certainly, a friction model that captures the modulated shear rates of non-isothermal supercritical media is recommended to obtain an accurate prediction of the mass flow rate in smaller, higher power natural circulation loops.

3.3 Experimental methodology

In this chapter, the natural circulation configuration as specified in figure 2.1 is used for the experiments. The range of thermodynamic states considered in the analysis are shown in figure 3.2, where the mean system pressure, p_m, is expressed as the reduced pressure, p_r, relative to the critical pressure of CO_2, $p_c = 73.8$ bar. During operation, the coolant temperature is adjusted at a constant volume to establish the desired steady-state pressure. This approach ensures that a constant mean thermodynamic state is maintained across different heating rates. The mean state is continuously monitored and retrospectively evaluated by assuming a linear temperature distribution within the heat transfer equipment. The range of thermodynamic states achieved in this study is summarized in Table 3.1. These states were attained at heating rates of 400 W and 800 W and serve as the basis for analyzing the dependence of mass flow rate on thermodynamic state, as well as for assessing the performance of the steady-state equation.
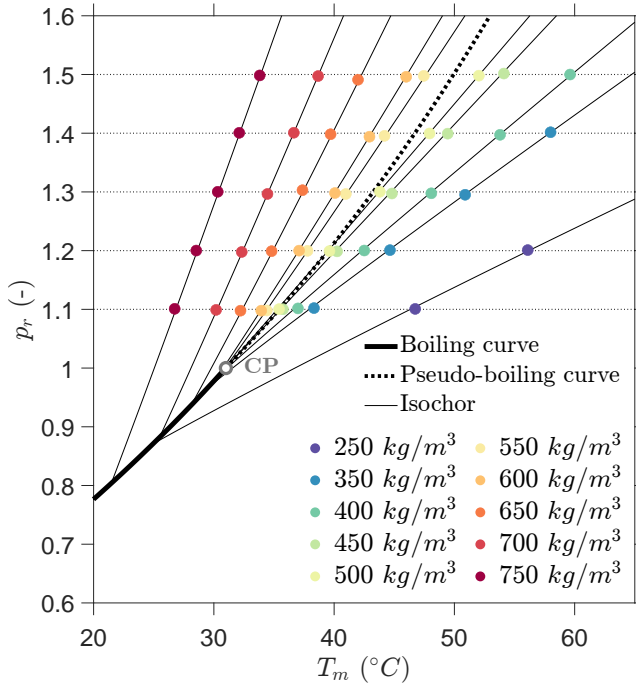
Figure 3.2: Lines of constant mass at set system volumes for carbon dioxide at supercritical pressure. All current experimental data points are indicated at the measured T_m and p_m for all considered nominal densities ρ_{nom}. The boiling- and pseudo-boiling curves are indicated with thick solid and dashed lines, respectively. The critical point is indicated in the figure with CP.

3.4 Results & discussion

During the steady operation of the natural circulation loop, the loop temperature distribution varies with thermodynamic state. The loop temperature distribution for an assortment of states within the considered range is depicted in figure 3.3. Here, the size of the horizontally shown temperature ranges corresponds with the magnitude of the difference in temperature between the hot- and cold sections of the loop. The natural flow is driven by moderate temperature differences, especially in the vicinity of the pseudo-critical line. With increasing pressure beyond the critical point, the pseudo-critical curve gradually transforms from a point of near-discrete phase transition to a gradually increasing region of mild property gradients. Additionally, as the fluid's specific heat near this curve decreases with pressure, less variation of
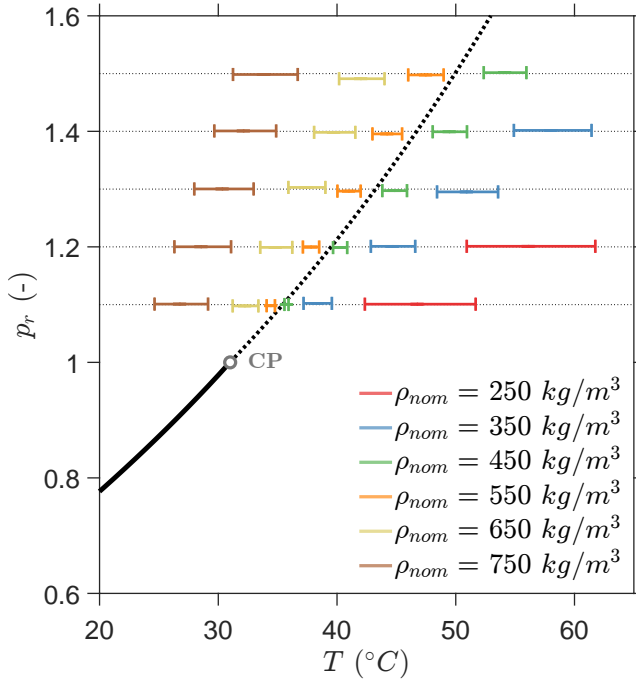
Figure 3.3: System temperature ranges for selected loop filling masses, at $\dot{Q} = 800$ W, $\Delta z = 2.5$ m. The shown ranges (horizontal in the figure) are bound by the greatest and lowest measured temperatures along the loop during operation at a certain steady state. The boiling- and pseudo-boiling curves are indicated with solid and dashed lines, respectively. The critical point is indicated in the figure with CP.

driving temperature gradient is found along isobars of greater magnitudes. Of course, a quantitative assessment of the loop temperature distribution follows from the steady state mass flow rate. If the loop mass flow rate is known, the loop temperature maxima and minima can be obtained using $T_{\text{max,min}} = T_{\text{m}} \pm \dot{Q}/(2\dot{m}c_{\text{p,m}})$. Using the experimental mass flow rate $\dot{m}_{\text{exp}}$, close agreement with experimental data is found for the considered range of thermodynamic states.

In this work, equations (3.6) and (3.9) are proposed for the prediction of steady mass flow rate $\dot{m}$. A comparison of equation (3.9) with experimental data is given in figure 3.4. The experimental data for this figure is obtained in the absence of the regulating valve depicted in figure 2.1. As it is for now not yet clear whether the viscous losses in the system have been accurately captured by the used friction model, the predicted mass flow rate is not yet corrected for the measured pressure losses in
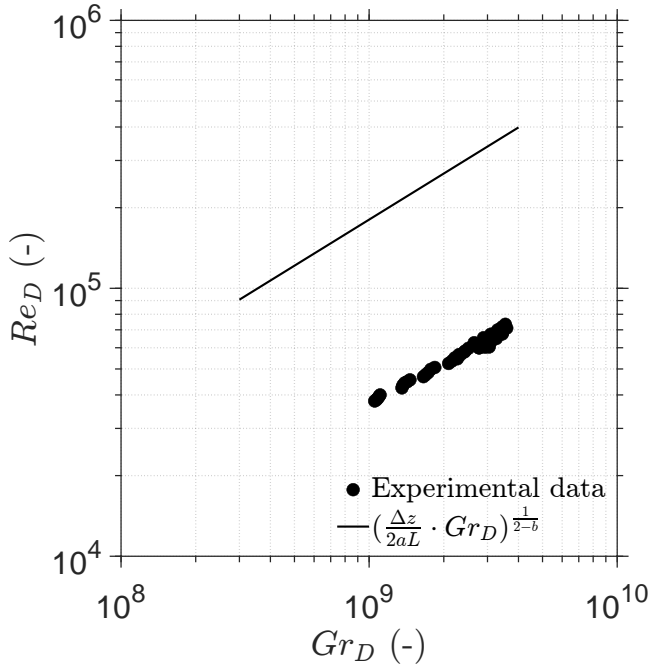
Figure 3.4: Re_D as function of Gr_D for experimental data in the range of the operating values indicated in table 3.1. The prediction of equation (3.9) is indicated in the figure with the solid curve.

the mass flow meter. Whereas the measured flow rates are consistently overpredicted in the figure, a comparable trend can be observed between the prediction and the experimental data. In search of generality, the validity of the assumptions and modelling choices made in the derivation of dimensional equation (3.6) are to be independently tested. As such, the contributions of the individual terms in equation (3.6) are further investigated in this work.

In order to consider the independent contribution of $\dot{Q}$ in equation (3.6), all other terms have to attain constant values when $\dot{Q}$ is varied. Through variation of the coolant temperature, a constant thermodynamic mean state can be maintained with varying heating rates. As the measured value of $\Sigma(f_i L_i)$ is however nonconstant due to variation in U, $\dot{m}_{\text{exp}}$ has to be compensated for using

$$\dot{m}_{\text{cor,fl}} = \dot{m}_{\text{exp}} \cdot \left(\frac{C_{\text{fl}}}{\Sigma(f_i L_i)_{\text{exp}}}\right)^{1/3} . \tag{3.10}$$
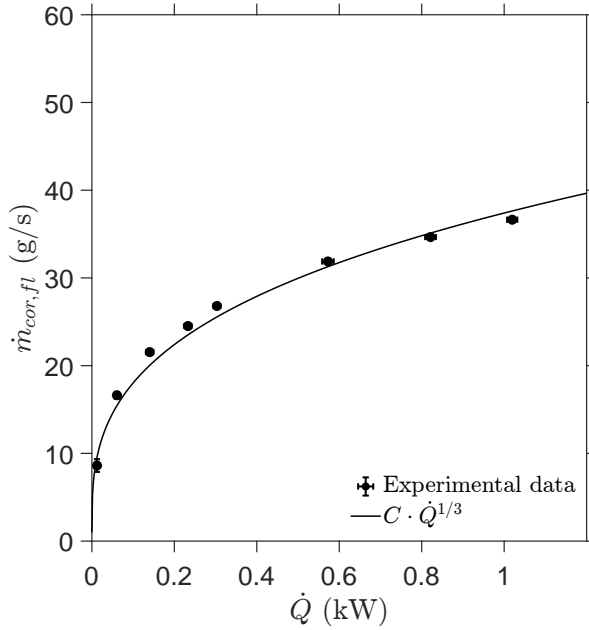
Figure 3.5: Variation of $\dot{m}_{\mathrm{cor,fl}}$ with $\dot{Q} = \dot{m}_{\mathrm{cor,fl}}\Delta h$, at $\rho_{\mathrm{nom}} = 700$ kg m^{-3}, $p_{\mathrm{r}} = 1.5$, $\Delta z = 2.5$ m, with 95% confidence intervals. Constant C is chosen as such that the leftmost data point coincides with the theoretical curve.

Here, $\dot{m}$ is assumed to scale with $\Sigma(f_i L_i)^{-1/3}$, following equation (3.6). The value of C_{fl} should be chosen such that it matches one of the values of $\Sigma(f_i L_i)$ within the considered experimental data set. As will be shown later in this work, the experimental uncertainty is the least for $\rho \geq 700$ kg m^{-3} and $p_{\mathrm{r}} \geq 1.3$ within the considered range of thermodynamic states. As such, this range of thermodynamic conditions is chosen for the assessment of the individual contributions of $\dot{Q}$, Δz, and $\Sigma(f_i L_i)$. In figure 3.5, the expected contribution of $\dot{Q}$ is compared to corrected empirical data. Here, the measured increase in heating rate $\dot{Q} = \dot{m}_{\mathrm{cor,fl}}\Delta\mathcal{H}$ is used rather than the imposed electrical heating rate $\dot{Q}_{\mathrm{imp}}$, in order to account for heating losses in the system. Close agreement is found between the predicted trend in mass flow rate and the experimental data for the considered range, hence $\dot{m}$ is assumed to scale with $\dot{Q}^{1/3}$ from this point onwards. As such, heating losses can be compensated for in investigations of data sets in which $\dot{Q}$ is to be kept constant using

$$\dot{m}_{\mathrm{cor},\dot{Q}} = \dot{m}_{\mathrm{exp}} \cdot \left(\frac{\dot{Q}_{\mathrm{imp}}}{\dot{m}\Delta\mathcal{H}} \right)^{1/3} . \tag{3.11}$$
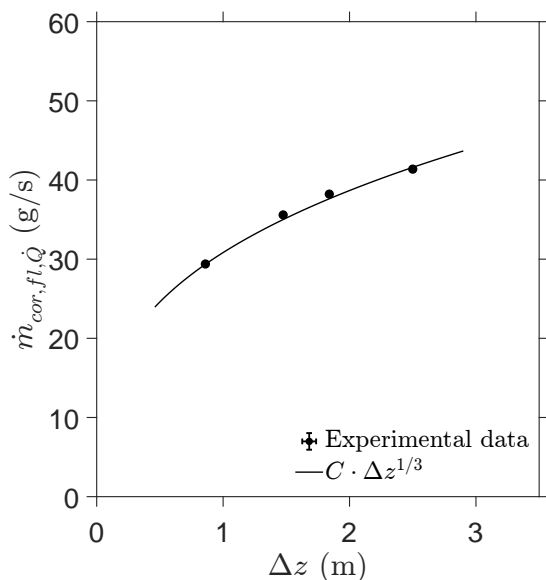
Figure 3.6:   Variation of $\dot{m}_{\mathrm{cor,fl},\dot{Q}}$ with Δz, at $\rho_{\mathrm{nom}} = 700\ \mathrm{kg\ m}^{-3}$, $p_{\mathrm{r}} = 1.3$, $\dot{Q} = 800\ \mathrm{W}$, with 95% confidence intervals. Constant C is chosen as such that the leftmost data point coincides with the theoretical curve. Error bars are present in the figure, but do not exceed the marker size.

One such corrected set of empirical data is shown in figure 3.6.   The depicted experimental data has been corrected for both variation in viscous losses, and variation in heating losses. Here, the expected change in $\dot{m}$ with variation in Δz is compared to data from experiments in which Δz is independently varied. Again, close agreement is found between the prediction and experiment.

An investigation of the influence of thermodynamic state follows in figure 3.7. For the current analysis, the measured value of $\Sigma(f_i L_i)$ has been found to vary with pressure, whereas its value remains predominantly constant along each isobar. Hence, the theoretical fluid property contribution of equation (3.6) is multiplied with $C_{f(p_{\mathrm{r}})}$. The value of this constant is chosen as such that the theoretical curve intersects with the lowest mean temperature data point for each reduced pressure. Heating losses are compensated for using equation (3.11), and the corrected mass flow rate values $\dot{m}_{\mathrm{cor},\dot{Q}}$ are shown in the figure. The proposed theoretical contribution of thermodynamic state is found to closely and continuously describe the corrected data for any degree of sub-cooling in the considered range of parameters. Note that the size of the confidence intervals of $\dot{m}_{\mathrm{cor},\dot{Q}}$ varies greatly with thermodynamic state. The
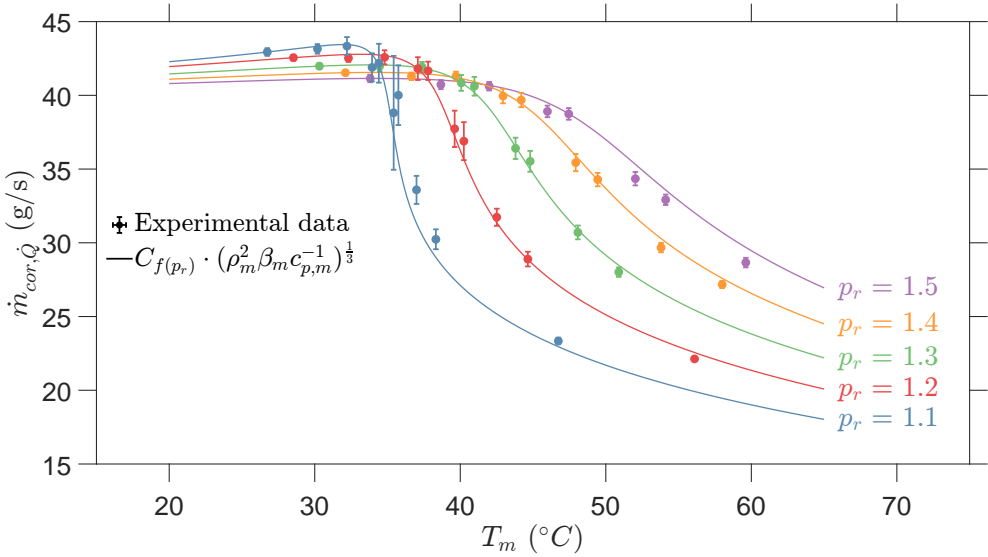
Figure 3.7: Variation of $\dot{m}_{\text{cor},\dot{Q}}$ with T_{m} and p_{m}, at $\Delta z = 2.5$ m, $\dot{Q} = 800$ W, with 95% confidence intervals. $C_{f(p_{\text{r}})}$ is chosen as such that the leftmost data point for each p_{r} coincides with the theoretical curve.

uncertainty in measurements of temperature and pressure is however mostly constant within the current range of experiments. As the sensitivity of enthalpy to temperature however varies with pressure, the uncertainty in enthalpy follows accordingly. This makes that the uncertainty in the determination of the fluid enthalpy used for the correction of heating losses is greatest near maxima of specific heat, hence at the pseudo-critical line at pressures in the vicinity of the critical pressure. Therefore, investigations of individual contributions of equation (3.6) should be performed away from the pseudo-critical curve, to reduce the uncertainty of the findings. As such, the more liquid-like, high pressure thermodynamic states are considered for these analyses, as previously elaborated on in this work.

Finally, the effect of pressure losses caused by equipment is investigated. For this, the joint pressure drop Δp_{e} over the flow meter and the regulating valve section is monitored. Pressure drop Δp_{e} is the summed value of the readings over both differential pressure transmitters indicated with (dP) in figure 2.1. A fully developed pipe flow is assumed along the loop, for which the viscous losses are approximated using an ideal fluid model, as elaborated on previously in this work. Figure 3.8 shows the loop mass flow rate as a function of the experimental values of Δp_{e}, and the relative magnitude of Δp_{e} with respect to the estimated total viscous pressure losses

in the system. The regulating valve is present in all but two data points of the current analysis, for which it is removed from the supercritical NCL. In the leftmost data point in the figure, both the valve and the mass flow meter are removed from the experimental facility. Here, the mass flow rate is estimated from the imposed heating rate and the measured enthalpy increase over the heater, i.e. $\dot{m}_{exp} = \dot{Q}_{imp}/(\mathcal{H}_{h,exp} - \mathcal{H}_{c,exp})$, where $\mathcal{H}_{c,exp}$ and $\mathcal{H}_{h,exp}$ are the enthalpies measured for the cold- and hot leg, respectively. The high sensitivity to temperature in deducing enthalpy makes that the uncertainty for this data point is significantly larger than for the data for which a mass flow meter is still present. Furthermore, as heating losses cannot be reliably estimated for this data point, they are not compensated for. The predictive curve is obtained by adding a fictitious equipment loss term $(fL)_e = (\Delta p_e D)/(2\rho_c U_c^2)$ in the viscous loss term in equation (3.6), where ρ_c and U_c are the cold-leg density and velocity, respectively. For each value of Δp_e, the distribution of the viscous losses in the system has to be iteratively solved for. As such, the presented theoretical curve in figure 3.8 is state- and configuration dependent and therewith only applicable to the current analysis.

The theoretical curve is found to closely resemble the experimental data, indicating that the used viscous model accurately captures the viscous losses for the current configuration and heating rate. The value of the predictive curve at a zero value of Δp_e corresponds to the expected mass flow rate in case no equipment losses are assumed. A comparison of the two leftmost points in the figure shows that a threefold decrease in mass flow rate is the direct consequence of the inclusion of a flow meter in the experimental loop. The difference in mass flow rate is of similar magnitude as the shift in figure 3.4, in which equipment pressure losses were not taken into account. As can be seen from figure 3.8, the losses in the flow meter alone are estimated to exceed the regular viscous losses in the loop. For all the considered experimental data points of this work, the total loop viscous losses are dominated by the equipment losses of a single Coriolis transmitter. The associated loss of flow rate is expected to be even more prevalent in facilities with less simple geometries, in which the flow is forced through a greater amount of instruments, or past series of turbine blades. Hence, the a priori characterization of the equipment minor losses is highly recommended for an accurate prediction of the steady mass flow rate of yet to be developed supercritical NCLs, which are generally inflexible to changes in maximum heat throughput. Without the proper portrayal of such losses, equation (3.6) will only serve as a qualitative measure of the sensitivity of $\dot{m}$ to changes in thermodynamic state, Δz and $\dot{Q}$.

Figure 3.9 shows the error in the prediction of the experimental steady state mass flow rate $\dot{m}_{exp}$, if the measured Δp_e is included in the viscous loss term of equation (3.6). Here, the imposed heating rate $\dot{Q}_{imp}$ is used in equation (3.6) to yield a predictive mass flow rate. As shown in the figure, close agreement is found with the predicted
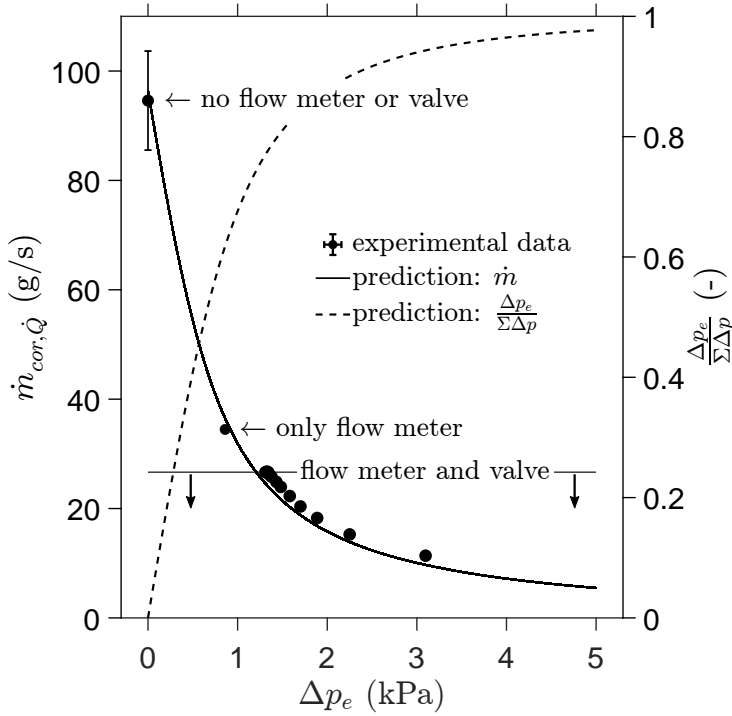
Figure 3.8: Left axis, full line and markers: variation of $\dot{m}_{cor,\dot{Q}}$ with Δp_e, at $\rho_{nom} = 730 \text{ kg m}^{-3}$, $p_r = 1.1$, $\Delta z = 2.5$ m, $\dot{Q} = 400$ W, with 95% confidence intervals. The predictive curve is found by varying the equipment loss term $(fL)_e$ in equation (3.6), and solving for $\dot{m}$. The leftmost data point has not been corrected to take heating losses into account. Right axis, dotted line: Δp_e as a fraction of the estimated total loop pressure losses $\Sigma\Delta p$.

mass flow rate $\dot{m}_p$ for the majority of the data.

For larger mass flow rates, the experimental flow rate is increasingly overpredicted. A likely cause for the above is an underprediction of the viscous losses in the flow in the non-adiabatic sections of the setup by the ideal fluid friction model used in the comparison. As qualitatively described in the work of Wahl et al. (2022), the alignment of the direction of both forced- and natural convection can result in near-wall velocities that are greater than in an adiabatic setting. For flows of supercritical media, the above applies to downward cooled and upward heated pipe flows. Since such alignment is present in both heat transfer configurations of the investigated loop
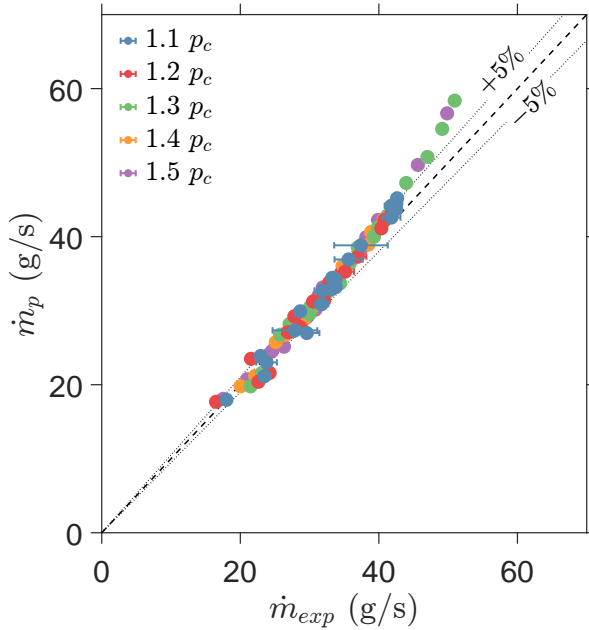
Figure 3.9: Steady state prediction error with inclusion of measured ΔP_e into equation (3.6), at $\Delta z = 2.5$ m, with 95% confidence intervals. Here, the imposed $\dot{Q}_{imp}$, Δz, D, and the measured T_m, p_m and Δp_e are used as input parameters for equation (3.6).

for the preferential flow direction, enhanced buoyancy-aided shear is expected in- and directly downstream of the cooler and heater. The deviation from ideal behavior is expected to increase for thermodynamic states that are more liquid-like, and at greater heating rates (Fang et al., 2020), at which larger mass flow rates are also expected. As such, the increasingly large over-prediction shown in figure 3.9 is expected. Closer agreement between equation (3.6) and empirical data would be found if a more complex friction model that captures the non-ideal modulation of shear in the heat exchangers would be used for the comparison. However, if aware of its caveats, a simple ideal fluid friction model can already be used to yield fair and quick predictions of the mass flow rate for a large parameter space, as can be deduced from figure 3.9.

3.5   Conclusions

The steady state behavior of a natural circulation loop that employs carbon dioxide at supercritical pressures is experimentally investigated in this chapter. In the experiments, the system's filling mass, its heating rate, the imposed driving height,

the external pressure drop, and the temperature of the coolant are varied. The temperature difference between the two vertical legs of the system which generates a vertical difference in density that drives the flow varies greatly within the considered thermodynamic range. This difference in temperature decreases with increasing proximity towards the critical point and the pseudo-boiling curve. It is here that the non-ideal thermodynamic behavior of the medium is the most significant. In order to systematically characterize the behavior of NCLs throughout the thermodynamically complex region, an equation for the prediction of the steady state mass flow of NCLs at supercritical pressures is proposed in this work. The analytical model is thereafter compared with experimental data. This assessment involves an evaluation of the equation's overall validity, as well as an analysis of its sensitivity to independently varied parameters, such as the heating rate, the differential heating height, the viscous losses and the thermodynamic state. Within the explored range of operational conditions and parameters, close agreement is observed between the predicted flow rate and experiment. Therewith, the mass flow rate of the supercritical NCL can be expected to scale with $\dot{Q}^{1/3}$, $\Delta z^{1/3}$ and $D^{5/3}$, the values of which are chosen during the design of an NCL. The mass flow rate is furthermore expected to scale with $(\rho^2 \beta / c_\mathrm{p})^{1/3}$, indicating that a higher flow rate is generated for more liquid-like than for more gas-like thermodynamic states, and that a maximum in mass flow rate is found just before the pseudo-boiling curve.

However, it is important to note the limitations of the proposed equation beyond the currently investigated parameter range. Practical applications of supercritical NCLs often demand significantly larger mass flow rates than those considered in this study. This is for instance true for the large-scale removal of heat from nuclear reactors. The current methodology linearizes gradients in thermodynamic properties at the mean system temperature T_m for a prediction of the mass flow rate. As the heating rate $\dot{Q}$ becomes relatively larger compared to mass flow rate $\dot{m}$, a larger thermodynamic space is traversed, and the true variations in thermodynamic properties across the system are less accurately captured. Moreover, the increasingly non-ideal shear stresses at higher $\dot{Q}$ may require the use of new, yet to be developed friction models for the considered heat transfer configurations, in order for the proposed equation to remain accurate. Additionally, higher heating rates can induce unwanted dynamic behavior both in the heater and throughout the NCL, such as heat transfer deterioration with wall temperature fluctuations and density wave oscillations, respectively. An understanding of the latter phenomenon is essential for scaling up NCLs at supercritical pressures in the context of large-scale, reliable heat removal devices. Considering the above factors, it is advisable to increase D and Δz as opposed to $\dot{Q}$ of a NCL at supercritical pressures if larger flow rates are desired, in favor of both the temporal

stability of the NCL and the predictive accuracy of the proposed equation.

3

Chapter 4

Natural circulation at a supercritical pressure
dynamic oscillations[1]

Supercritical natural circulation loops (NCLs) promise passive cooling for critical systems like nuclear reactors and solar collectors, eliminating the need for mechanical pumps. However, instabilities similar to those seen in two-phase systems can emerge in supercritical NCLs, leading to undesirable oscillatory behaviour, marked by system-wide fluctuations in density, temperature, pressure, and flow rate. This chapter investigates the stability of NCLs at supercritical pressures ($73.7 \leq p \leq 110.0$ bar) with CO_2 in our NCL facility with vertical cooling and vertically adjustable heaters to control convective flow rates and to oppose flow reversal. Oscillations were found to originate in the heater of the NCL, and demonstrated a high sensitivity to the thermodynamic state and proximity to the pseudo-critical line of the system. Increased mass flow rates and added resistance upstream of the heater suppressed the oscillations, while increased pressures and reduced heating rates dampened them. A static model which takes into account the non-ideality of the heat exchangers is introduced to assess the presence of multiple steady states. The oscillations are concluded to be dynamically induced. In particular, the modulation of the NCL velocity by the traversal of the current oscillations in density is assumed to periodically re-incite non-ideality in the heater. These findings refine our understanding of the stability boundaries in NCLs, to ensure a safer operation of prospective passive cooling and circulation systems employing fluids at supercritical pressure.

4.1   Introduction

Natural circulation loops are passive circulators, as they do not rely on mechanical propulsion for fluid flow. This makes them particularly attractive for off-grid cooling applications in critical systems, such as nuclear reactors and solar thermal systems, when nearby heat sinks are available for effective heat dissipation. When the induced mass flow rates of the reliable natural circulators are sufficient, they can potentially replace their existing forced convective counterparts.

Two-phase circulation loops, in particular, offer substantial potential for energy transport due to the significant volumetric expansion of their phase transitions. However, two-phase systems are often prone to dynamic instabilities, associated with the phase-change phenomena within the loop (Boure et al., 1973; Kakaç and Bon, 2008). These instabilities can lead to substantial flow oscillations and dry-out, limiting the reliability of potential passive circulators with large heating loads.

In response to these challenges, NCLs with fluids at supercritical pressures have emerged as a promising alternative. Much like two-phase systems, NCLs with working fluids at supercritical pressures can yield passive flow rates of a sufficient magnitude for the removal of nuclear and concentrated solar heat. However, whereas complex phase-change behaviour is in principle avoided at a supercritical pressure, supercritical pressure NCLs are still prone to several analogous instabilities.

For natural circulation loops, the classification of flow instabilities in two-phase systems is generally extended into the supercritical region (Wang et al., 2024; Rai et al., 2025). Therewith, a distinction is made between statically and dynamically unstable flow systems (Boure et al., 1973; Kakaç and Bon, 2008). When an NCL is statically unstable, multiple steady state solutions exist that satisfy the conservation equations. Then, perturbations within the NCL can lead to single-event or repeating excursions that shift the system between steady states. An instability is considered dynamic when the system requires a feedback mechanism to develop and sustain unsteady behaviour (Boure et al., 1973). As such feedback effects are not captured in static models, a model of the steady state by itself is not sufficient to predict a system's dynamic stability limits. So far, the dynamic stability of supercritical CO_2 NCLs has most commonly been studied in the context of Density Wave Oscillations (DWOs) and Pressure Density Oscillations (PDOs), whereas static instabilities have mainly been of the above-discussed Ledinegg type (Wang et al., 2024; Rai et al., 2025; Garg and Dutta, 2020).

The dynamic stability of natural circulation loops (NCLs) at supercritical pressures has been extensively modelled. Although three-dimensional analyses have been undertaken (Chen et al., 2014; Wahidi et al., 2021), most numerical studies model

NCLs using non-linear one-dimensional approaches. Most commonly, a boundary heating rate has been presented as the stability threshold, beyond which instabilities occur (Chatoorgoon, 2001; Jain and Rizwan-uddin, 2008; Sharma et al., 2010a,b; Debrah et al., 2013; Chen et al., 2014). This threshold has been found to be sensitive to several operating parameters, such as the heater inlet temperature (Chatoorgoon, 2001; Sharma et al., 2010a,b), the system pressure, its mass flow rate (Wahidi et al., 2021), and the loop diameter (Rai et al., 2021). Using linearized one-dimensional models, the thermodynamic dependence of the stability limit has been elaborated on (Ambrosini and Sharabi, 2008; Debrah et al., 2013). Furthermore, the dynamic stability of an NCL has been found to be strongly affected by the configuration of the heat exchangers. When all heat is exchanged along the horizontal legs of the system, the NCL has no preferential flow direction. Then, the NCL is prone to flow reversal. In a system with heat exchange along at least one of its vertical legs, the vertical line symmetry is broken. As a result, the risk of flow reversal instabilities is greatly reduced (Welander, 1967; Zhang et al., 2010; Sharma et al., 2013; Chen et al., 2014; Wahidi et al., 2021), substantially increasing the stable heating threshold.

Moreover, to assess whether static instabilities can prevail in a supercritical pressure NCL, the system can be investigated for the presence of multiple steady states. The driving pressure of a loop (resulting from a density difference over its vertical legs) balances with its viscous friction (Δp_v) throughout the system to circulate CO_2. At any possible steady state, the two quantities are equal. If multiple steady states exist - at multiple mass flow rates - the system may transition to different steady states upon a perturbation, or alternate between various steady states, resulting in limit cycle oscillations (Kakaç and Bon, 2008; Rahman and Singh, 2019; Wang et al., 2024). When an ideal sub-critical friction model is used in the static model, ignoring the effects of thermodynamic property variations, the CO_2 NCL is predicted to be statically stable (Yu et al., 2011; Swapnalee et al., 2012; Garg and Dutta, 2020; Huang et al., 2024).

The stability of NCLs at supercritical pressures has also been explored experimentally. The earliest reports of unstable behaviour in the supercritical pressure NCL considered the symmetric horizontal-heater-horizontal-cooler (HHHC) configuration(Vijayan et al., 2007; Elton et al., 2020), for which the mass flow rate is maximized, but flow reversal are more prevalent (Swapnalee et al., 2012). Most investigations of non-HHHC loops that followed reported stable behaviour within the considered parameter ranges when the NCL was not externally forced (T'Joen and Rohde, 2012; Sharma et al., 2013; Li et al., 2022). However, Liu et al. (2017); Huang et al. (2024) later reported oscillations in this non-HHHC setting, in which heat is transferred along the vertical legs of the system. In Huang et al. (2024), a parallel-channel ver-

4

tical heater within an NCL was investigated for instabilities. The authors reported irregular PDO's in the vicinity of the pseudo-critical curve that were strongly influenced by the presence and position of a large pressurizer. In the work of Liu et al. (2017), a departure from stability was observed in a single-channel supercritical CO_2 NCL. Unlike system-wide density-wave oscillations, the temperature oscillations were limited to the NCL heater outlet. The oscillations were most predominantly found in the vicinity of the pseudo-critical curve. Similarly to Huang et al. (2024), an increase in pressure was found to stabilize the system, likely due to a reduction in thermal property variations near the pseudo-critical line. Additionally, the presence of a local resistance was reported to enhance or lessen the stability of the NCL, depending on the placement of the local loss (Liu et al., 2017).

The current chapter experimentally investigates the stability of a natural circulation loop at supercritical pressure. In particular, an NCL with all heat exchange along its vertical legs is considered. Given its enhanced stability and its reduced sensitivity to flow reversal, this configuration in particular is promising for stable passive circulators and coolers with large throughputs for high-energy application. Nevertheless, even for this most stable heating configuration, an eventual limit to the stability of an NCL has been predicted in simulations. However, these predictions are largely based on one-dimensional models that necessarily rely on strong simplifications—particularly in the treatment of wall friction and heat transfer under highly non-ideal conditions. As such, experimental validation is essential to support these models and assess the accuracy of their predicted stability limits. To date, little experimental evidence of unsteady behavior has been presented. While substantial local oscillations in heat exchangers have been reported (Liu et al., 2017; Huang et al., 2024), global, system-wide oscillations in a single-channel NCL that resemble the predictions from numerical modelling have not yet been demonstrated in experiment. Therefore, the current experiments aim to identify and cross the stability limits of a supercritical NCL in the present configuration, to ultimately support the development of mitigation strategies and help prevent potentially catastrophic thermal fatigue in full-scale systems.

Our experimental setup facilitates substantial non-ideal expansions of carbon dioxide at supercritical pressures, with which the previously predicted limits of stability are approached. Contrary to other existing systems, the current facility employs heaters that can be moved vertically. By decreasing the vertical distance between the heating and cooling elements the mass flow rate of the NCL can be controlled and greatly reduced, even without a local resistance in the system. As such, the strong pseudo phase-change behaviour within full-scale high-energy natural circulation loops can be emulated with heating rates attainable in a laboratory setting, without local restrictors that may delay the onset of instability. Consequently, we have successfully

incited system-wide sustained oscillations in temperature, pressure and mass flow rate in a natural circulation loop with CO_2 at supercritical pressures. The current experiments consider the system's sensitivity to operating conditions and inputs, to explore the stability of large throughput passive circulators previously not touched upon in experiment.

A description of the experimental methodology is given in §4.2. Moreover, a simplified static model of the heater with which the stability mechanism is explored is proposed in 4.2.2 of §4.2. In §4.3, the perceived saturated oscillations are first described. Thereafter, the system's sensitivity to its operating conditions and inputs is assessed, and oscillation mitigation measures are proposed. Thereafter, possible instability mechanisms are discussed in §4.4. Finally, a summary of the most important conclusions is presented in §4.5.

4.2   Methodology

In this work, the oscillatory behaviour of the supercritical natural circulation loop is studied experimentally. Additionally, the heat exchangers are analyzed with a one-dimensional static model to support the discussion of the perceived instability. Hereafter, the current experimental facility and the static model are introduced in respective sub-sections.

4.2.1   Experimental methodology

4.2.1.1   Experimental facility

In this chapter, the natural circulation configuration as specified in figure 2.1 is used for the experiments.

4.2.1.2   Oscillation trigger procedure

To incite oscillations in the natural circulation loop, the system is first brought to a stable, non oscillatory state. At a given filling mass, the system pressure is increased to beyond 100 bar. Figure 2.2 shows the corresponding temperature for a selection of isochors. During this process, only the circulation heaters (*ch* in figure 2.1) are active to ensure stability of the system. Once a steady and stable circulation is achieved, the circulation heaters are disconnected, and the movable heaters are enabled. Consequently, the mass flow rate decreases, and the temperature difference between the two vertical legs increases. Thereafter, changes in the coolant temperature may lead to oscillatory behaviour in the natural circulation loop.

4.2.2   One-dimensional static model

Using a static model of the heat exchangers in particular, the system is examined for the presence of multiple steady states. In a static model, both the driving pressure and the viscous pressure loss are expressed as a function of the mass flow rate $\dot{m}$. Much like under forced convection, the flow through the NCL heat exchangers is assumed to be driven by constant pressure gradients, independent of the mass flow rate. Then, the criterion for multiple intersections with the viscous pressure loss is

$$\frac{\partial \Delta p_{\mathrm{v}}(\dot{m})}{\partial \dot{m}} < 0, \tag{4.1}$$

consistent with Swapnalee et al. (2012) and Rai et al. (2021). Essentially, the NCL is statically unstable when its viscous losses decrease as the mass flow rate increases.
In the unheated sections of the NCL the flow of CO_2 has constant thermophysical properties, and therefore approaches an ideal sub-critical adiabatic flow. However, ideal friction models for sub-critical fluids do not satisfy the criterion of equation. (4.1), as their friction factors f are weak functions of $\dot{m}$. On the contrary, when a flow of CO_2 is heated or cooled at a supercritical pressure, its viscous friction may depend strongly on buoyancy and property variations (Fang et al., 2012; Ehsan et al., 2018; Fang et al., 2020) and therefore vary significantly from an ideal approximation. It is only under such conditions, that the criterion in equation. (4.1) may be satisfied. Therefore, only the heat exchangers of the NCL are expected to be susceptible to static instability, if sufficiently non-ideal.
The following paragraphs present a simplistic one-dimensional model of the viscous losses in the heat exchangers of the current system that qualitatively and phenomenologically captures the effects of variations in several thermophysical properties to a variable extent. Using the model, the degree of non-ideality within the heat exchangers can be varied and compared to existing viscous models to evaluate the susceptibility of the system to static instabilities.

4.2.2.1   Heat exchanger model

A one-dimensional model is used to approximate the viscous losses Δp_{v} within the heat exchangers of the supercritical NCL. Figure 4.1 shows the numerical grid along which the heat exchangers are discretized with N elements with lengths L. Here, nodes [0,N] span the full length of the heat exchanger. At node 0, the mass flow rate $\dot{m}$, the pressure p and the bulk enthalpy h_{b} are imposed.
For the successive nodes i, the bulk enthalpy is determined using

$$h_{\mathrm{b(i)}} = h_{\mathrm{b(i-1)}} \pm \frac{\dot{Q}}{\dot{m}N}, \tag{4.2}$$
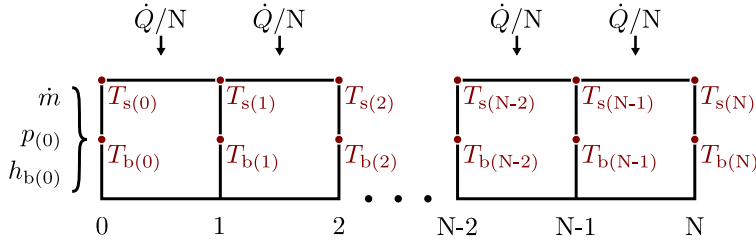
Figure 4.1: Schematic of static 1-D model of viscous pressure drop $P_v(\dot{m})$. The CO_2 temperature is evaluated at the bulk (T_b) and the surface (T_s) for all N cells.

where $\dot{Q}$ is the heating rate. The sign of $\pm$ depends on whether the movable heaters (+) are considered, or whether the cooler (-) is modelled. The viscous loss for each cell can be estimated using

$$\Delta p_{v(i)} = \frac{\left(f\dot{m}^2\right)L}{2\rho_{b(i-1)}A_{cs}^2 D}, \text{ where } f = f_{ni} \cdot f_{iso}. \tag{4.3}$$

Here, A_{cs} is the cross-sectional area of the heat exchanger with inner diameter D and length L. The friction factor f is a multiplication of the ideal and isothermal friction factor f_{iso} and a coefficient of non-ideality f_{ni}. The values of f_{iso} and f_{ni} are discussed in section 4.2.2.2. Using the pressure drop $\Delta p_{v(i)}$ and bulk enthalpy $h_{b(i)}$, the thermophysical properties of node i can be evaluated as

$$T_{b(i)}, \rho_{b(i)}, \mu_{b(i)} = f\left(h_{b(i)}, p_{(0)} - \sum_{0}^{i} \Delta p_{v(i)}\right), \tag{4.4}$$

The bulk Reynolds number $Re_{b(i)}$, for the evaluation of f_{iso}, is then obtained with

$$Re_{b(i)} = \frac{\dot{m}D}{\mu_{b(i)}A_{cs}}. \tag{4.5}$$

Here, $\mu_{b(i)}$ is the bulk viscosity of node i. As will be elaborated on in section 4.2.2.2, f_{ni} is evaluated with material properties with the wall temperature $T_{s(i)}$, which can be determined with

$$T_{s(i)} = T_{b(i)} \pm \frac{\dot{Q}}{A_p U}. \tag{4.6}$$

Here, A_p is the surface area of the heat exchanger pipe, and U is the equivalent heat transfer coefficient. To isolate the effect of viscous losses on the static stability, the current model assumes a constant heat transfer coefficient with a value of

configuration	$\left(\dfrac{\rho_{\text{w}}}{\rho_{\text{b}}}\right)^{\alpha}$	$\left(\dfrac{\mu_{\text{w}}}{\mu_{\text{b}}}\right)^{\beta}$
cooled downward flow	> 1	> 1
heated upward flow	> 1	< 1

Table 4.1: Value of terms in f_{ni} for current heat exchanger configurations

$U = 5\,\text{kWm}^{-2}\text{K}^{-1}$. The chosen value of U is within the same order of magnitude as most proposed heat transfer correlations for the present configuration (Pitla et al., 1998; Yoo, 2013; Ehsan et al., 2018; Zhang et al., 2020; Wang et al., 2023a), among which there is large variability. The currently chosen and relatively low value of U ensures a sufficient temperature difference between the pipe surface and the bulk to emphasize the influence of property variation on the viscous losses.

4.2.2.2 Viscous models

The viscous drag in the loop is modelled using an ideal-fluid model f_{iso}, and a correction factor f_{ni} that considers non-ideal effects, as per equation. (4.3). When non-ideal effects are not considered, $f_{\text{ni}} = 1$. The Blasius friction law for smooth pipe flows is used to determine f_{iso}, with

$$f_{\text{iso}} = 0.3164 \cdot Re_{\text{b}}^{-1/4}, \quad Re_{\text{b}} < 10^5 \tag{4.7}$$

The non-ideality caused by non-linear variations in thermophysical properties is approximated using a model that is based on the correlation proposed by Petrov and Popov (1985). This revised friction model is given as

$$f_{\text{ni}} = \left(\frac{\rho_{\text{w}}}{\rho_{\text{b}}}\right)^{\alpha} \left(\frac{\mu_{\text{w}}}{\mu_{\text{b}}}\right)^{\beta}. \tag{4.8}$$

Equation. (4.8) qualitatively considers both the modulation of near-wall velocity by the strong dilation of CO_2 (Jiang et al., 2008; Nemati et al., 2015; Ehsan et al., 2018) through $(\rho_{\text{w}}/\rho_{\text{b}})$, and the variation in the near-wall viscosity through $(\mu_{\text{w}}/\mu_{\text{b}})$. Phenomenologically, when the CO_2 is heated, density decreases at the wall. In an upward heated flow, the buoyancy increases the near-wall velocity, resulting in a stronger shear rate. To capture this effect with f_{ni}, the exponent α must be negative. Conversely, in a downward cooled flow, the density increases near the wall, yet buoyancy continues to aid the near-wall flow, similarly leading to a stronger shear rate. Thus, for a cooled downward flow, α should be positive. In contrast, the modulation of

the friction factor by viscosity is independent of the flow direction. When supercritical CO_2 is heated, the viscosity decreases, reducing the wall shear stress and thereby lowering the friction factor. The opposite is true for the cooler, where the near-wall viscosity is increasing, resulting in a higher friction factor. Consequently, $\beta > 0$ applies to both heat exchangers.

Thus, the effects of buoyancy and viscosity compete only in the heated upward flow, while in the cooled downward flow both effects increase $f_{ni} > 1$, as summarized in Table 4.1. This has a significant implication for the heater: when $f_{ni} \ll 1$ the overall friction factor can decrease with increasing mass flow rate to satisfy the criterion in equation. (4.1).

It is important to note that turbulence further complicates the modulation of the friction factor. In an upward heated flow, turbulence may weaken due to buoyancy effects and the thermal expansion of the near-wall fluid (Yoo, 2013; Nemati et al., 2015), leading to an even greater reduction in the friction factor. This phenomenon, known as heat transfer deterioration, occurs when reduced turbulence results in a lower turbulent heat transfer rate. We have incorporated this effect indirectly when specifying the values for α and β in section 4.4.

4.3 Results

The susceptibility of a supercritical pressure NCL to unwanted oscillations is investigated by considering the parameter range given in gray in table 4.2. To characterize the instabilities that can occur, the behavior of the NCL is compared for two distinct conditions within the considered range in section 4.3.1. Thereafter, in section 4.3.2, the operating conditions and inputs of the NCL are independently varied to assess the validity of existing stability models and to propose oscillation mitigation measures in section 4.3.3. The operating conditions and the varied parameters for each of the sections hereafter are indicated in table 4.2.

4.3.1 Overall characterization of the observed NCL instabilities

Starting from the initial steady state described in section 4.2.1.2, a decrease in the coolant inlet temperature leads to increased cooling. As a result, the pressure decreases towards the critical pressure. For case 2 of table 4.2, the circulation loop remains stable upon this perturbation, and only produces low amplitude and low frequency fluctuations with a period of approximately 37 s. As shown in figure 4.2(c), the fluctuations of the stable NCL only slightly exceed the amplitude of the sensor noise for case 2. The oscillations are caused by periodic corrections of the coolant inlet

varied par.	sect.	Δz (m)	$\bar{\rho}$ (kgm^{-3})	$\dot{Q}$ (kW)	$\bar{p}$ (bar)	valve	accu.
full range	4.3	$0.4 \leq \Delta z \leq 2.5$	$450 \leq \rho \leq 750$	$0.8 \leq \dot{Q} \leq 2.0$	$p_c < p < 110$	✓/×	✓/×
case 1	4.3.1	0.4	700	2.0	$p_c < p < 80$	×	×
case 2	4.3.1	0.9	700	0.8	$p_c < p < 80$	×	×
driving height	4.3.2.2	$0.4 \leq \Delta z \leq 0.9$	700	$1.0 \leq \dot{Q} \leq 2.0$	$p_c < p < 110$	×	×
resistance	4.3.2.3	0.4	700	2.0	$p_c < p < 100$	✓	×
density	4.3.2.4	0.4	$450 \leq \rho \leq 750$	2.0	$p_c < p < 100$	×	×
heating rate	4.3.2.5	0.4	700	$1.0 \leq \dot{Q} \leq 2.0$	$p_c < p < 80$	×	×
pressure	4.3.2.6	0.4	700	2.0	$p_c < p < 110$	×	×
accumulator	4.3.2.7	0.4	700	2.0	$p_c < p < 80$	×	✓

Table 4.2: Overview of the operating conditions of the current experiments. "valve" and "accu." indicate the inclusion of the cold-leg valve and the piston accumulator, respectively. If the column under "valve" lists ×, the Coriolis mass flow meter is also excluded from the facility.

temperature by the controller of the refrigerated circulator, as will be briefly elaborated in the paragraph hereafter. As the moderate fluctuations are only the consequence of the applied external forcing by the cooler, the system is considered stable.

Conversely, for case 1 of table 4.2, sustained oscillations eventually occur when the system is disturbed. As illustrated in figure 4.2(a), a rapid increase in the oscillation amplitude is observed below a mean pressure of $\bar{P} = 80$ bar. Subsequently, the pressure decreases quickly along the current isochor until the thermodynamic state stabilizes at a mean pressure of $\bar{P} = 76$ bar. At this new 'equilibrium,' the natural circulation loop exhibits oscillations in temperature and pressure with constant amplitude and frequency, as shown in figure 4.2(b) for a selection of pressure and temperature sensors along the loop.

Under oscillatory conditions, the natural circulation loop is characterized by system-wide signal fluctuations of a larger amplitude and higher frequency than during stable conditions. As shown in figure 4.2(b), the respective signals vary in amplitude and phase when the system is in a oscillatory state. However, as can be deducted from figure 4.3, all primary loop oscillations have the same dominant frequency. Figure 4.3 shows the power spectra of all sensors for a single case, and indicates their global peaks. For the loop temperature, pressure, and wall temperature data the global maxima are indicated with ∇. For these sensors, the global spectrum maxima coincide at F_d. Therewith, the oscillations in temperature and pressure are assumed to originate from the same phenomenon, despite their respective phase lags. For coolant sensors $T_{c,i}$ and $T_{c,e}$, the global maximum is indicated with $\circ$. The frequency at which $T_{c,i}$ and $T_{c,e}$ oscillate is significantly lower than for the other sensors in the system, and coincides with the frequency at which the coolant temperature is controlled. It is also this frequency that drives the moderate oscillations seen during the steady operation of the loop, as shown in figure 4.2(c).

The natural circulation loop displays both synchronized and non-synchronized fluctuations when it is oscillating. In line with case 2 of figure 4.2(c), the fluctuations in temperature are always out of phase. There, the relative phase lag between the temperature signals varies among the experiments. In figure 4.4, the respective phase lags of the temperature signals of case 1 of table 4.2 are shown in a space-time diagram. The figure indicates an approximation of the local circulation velocities in both the hot- and cold sections of the system, U_h and U_c, with

$$U_h = \frac{\dot{m}_{est}}{\rho_h \frac{\pi}{4} D^2}, \quad \rho_h = \rho \left(P_{01}, \frac{T_{01}}{2} + \frac{T_{02}}{2} \right), \tag{4.9}$$

and

$$U_c = \frac{\dot{m}_{est}}{\rho_c \frac{\pi}{4} D^2}, \quad \rho_c = \rho \left(P_{02}, \frac{T_{03}}{2} + \frac{T_{04}}{2} \right). \tag{4.10}$$
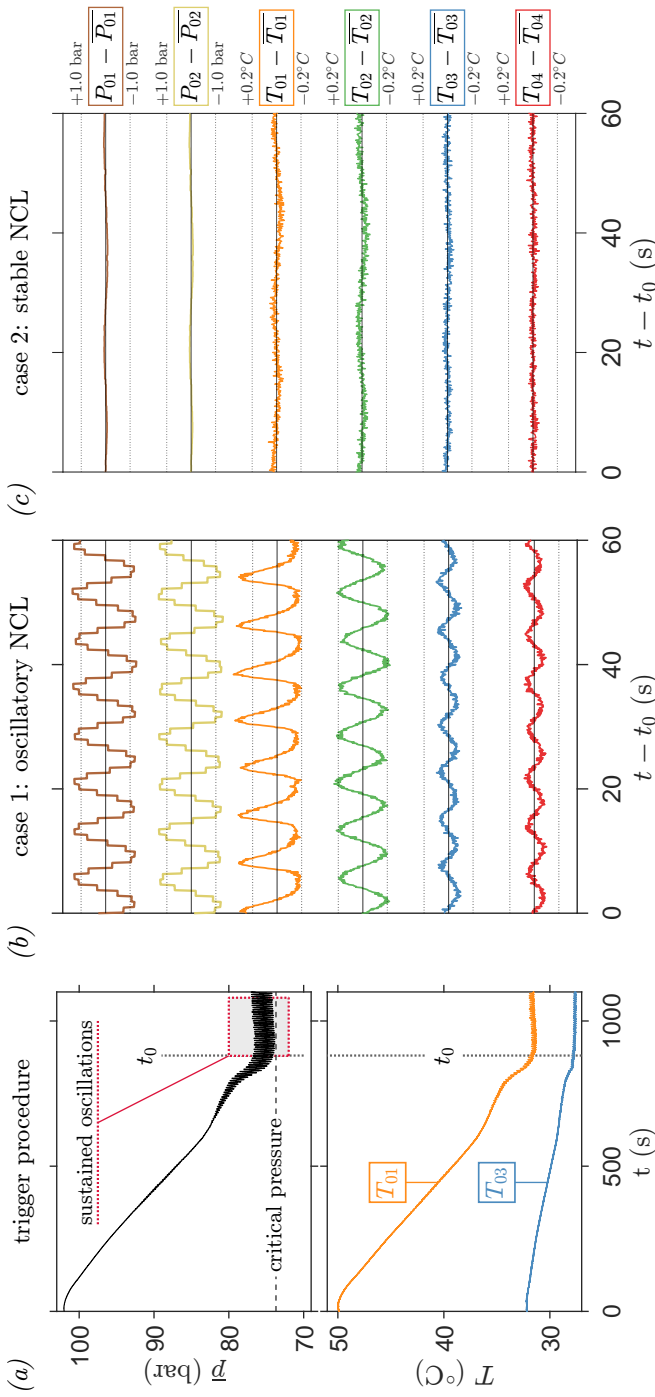
Figure 4.2: Sustained dynamic oscillations in the supercritical carbon dioxide natural circulation loop. (a): shows the phase leading up to the onset of oscillations in the system. At $t = 0$ s, the temperature of the coolant is reduced, and the pressure of the initially steady system decreases along an isochor. Subsequently, the system displays finite oscillations in both temperature and pressure, at a mean absolute pressure $\bar{p} = 76$ bar and nominal density $\rho = 700$ kgm^{-3}. (b) and (c) compare the normalized signal of several transmitters throughout the system for a case in which the NCL is oscillatory (b) to a case in which the NCL is stable (c), corresponding to case 1 and case 2 of table 4.2, respectively. The y-axis values of both (b) and (c) are given in (c).
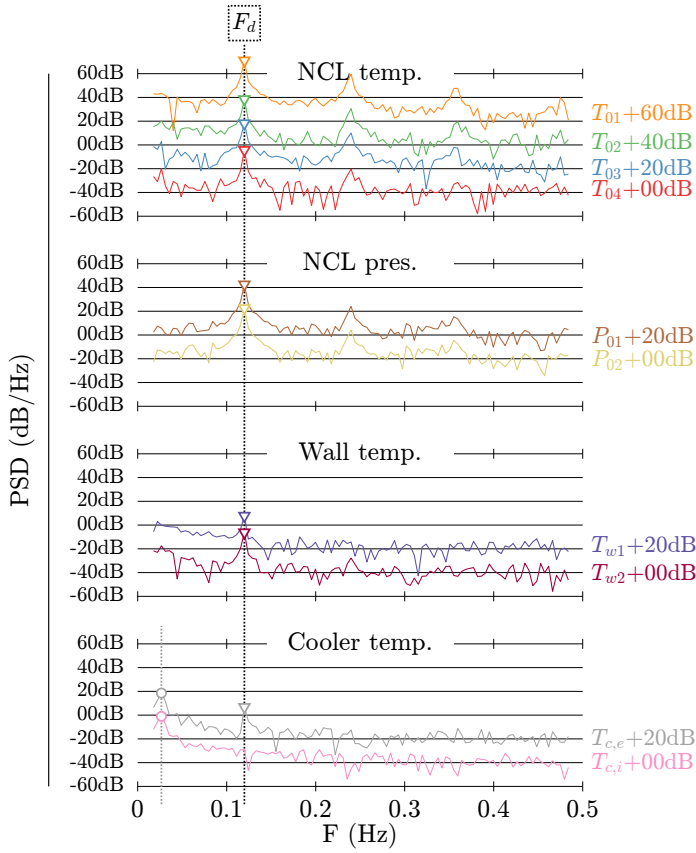
Figure 4.3: Power spectra of sensor data under oscillatory conditions (case 1 of table 4.2). Maxima in the spectra for internal temperature data (NCL temp.), absolute pressure data (NCL pres.) and external wall temperature data (Wall temp.) are indicated with ∇. The locations of ∇ coincide on dominant frequency F_d. Maxima in the spectra of the coolant temperatures (Cooler temp.) are indicated with $\circ$, and with the grey dotted line. An additional local maximum in the spectrum of cooler outlet temperature $T_{c,e}$ is indicated with ∇.

There, the advection velocities are assessed using the estimated mass flow rate $\dot{m}_{est}$, and the densities for the hot- and cold sections ρ_h and ρ_c. In figure 4.4, lines of U_h and U_c are superimposed upon the temperature signals. These lines are drawn for every period $1/F_d$, the period of the dominant oscillation of case 1. In the figure, lines of constant U_h that intersect the signal of T_{01} at a wave crest also intersect a subsequent wave crest of T_{02}. Similarly, lines of constant U_c intersect fluctuation crests of both
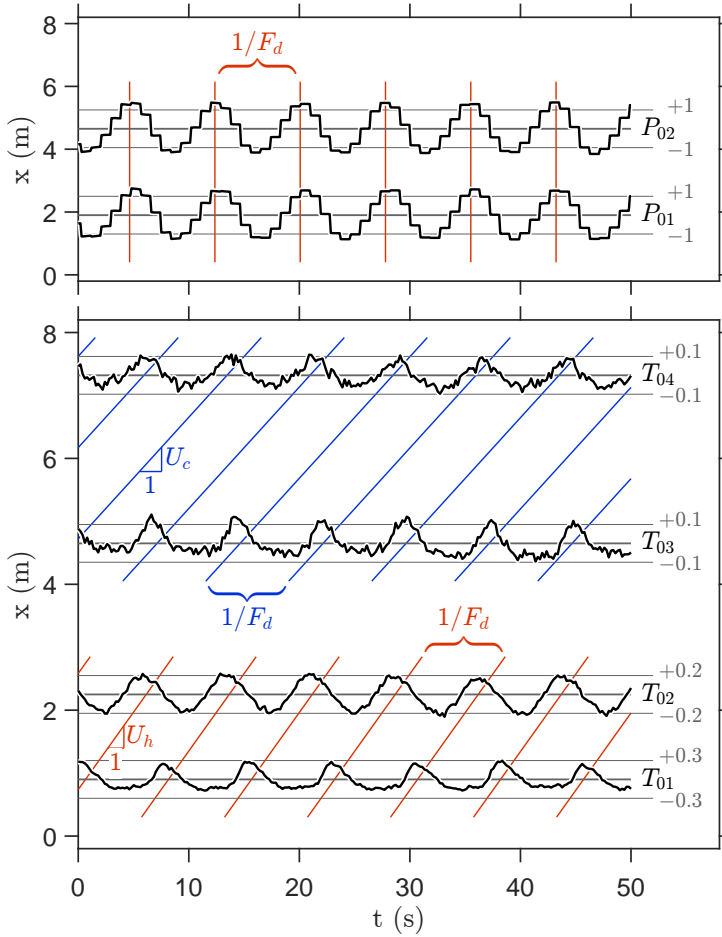
Figure 4.4: Space-time comparison of respective phase lag of NCL signals with respect to the dominant frequency F_d and the hot- and cold leg advection velocities U_h and U_c, respectively. For the case shown in the figure (case 1 of table 4.2), $\dot{m}_{exp} = 48.2$ gs^{-1}, $U_h = 0.25$ ms^{-1}, and $U_c = 0.19$ ms^{-1}. The normalized values of the sensor outputs are shown at their respective positions x along the loop.

T_{03} and T_{04}. Therewith, figure 4.4 suggests the presence of thermal waves that are advected through the natural circulation loop at the local circulation velocity. Then, the relative phase lags of oscillations at the temperature sensors vary as the mass flow rate of the system changes. On the contrary, the pressure oscillations are always in phase within the considered parameter range. This synchronization of the pressure

signals suggests the occurrence of a global thermal (de)compression of the system, upon which the pressure is redistributed almost instantaneously at the local speed of sound. When heat is transferred to- or from the loop, the pressure of the system varies along the red isochoric arrow in figure 2.2. However, as the thermal diffusivity and the mixing of the carbon dioxide is finite, the temperature of the CO_2 is not redistributed instantaneously. Instead, the temperature of the CO_2 near the source of the heat imbalance builds, and a 'pocket' of carbon dioxide with a different density than the fluid it is surrounded by is formed. As these thermal pockets are advected by the flow, they assume the form of the currently observed thermal fluctuations, and induce system-wide oscillations.

4.3.2 Sensitivity to operating parameters

To explore the stability boundary between the oscillations in case 1, and the steady circulation of case 2, the operating parameters of the NCL are varied independently hereafter. Therewith, we aim to approach and cross the most widely accepted stability boundaries of supercritical pressure NCLs proposed by Ambrosini and Sharabi (2008); Debrah et al. (2013) in experiment. The operating conditions and independently varied parameters for each of the subsections hereafter are given in table 4.2.

4.3.2.1 Stability map

Based on the linearized one-dimensional numerical analysis of the supercritical pressure NCL, Ambrosini and Sharabi (2008); Debrah et al. (2013) have proposed maps of the stability of the current system. The stability boundaries of the NCL are expressed using dimensionless quantities N_{SUBPC} and N_{TPC}, with

$$N_{\text{SUBPC}} = \frac{\beta_{\text{pc}}}{C_{p,\text{pc}}}(h_{\text{pc}} - h_{\text{b,h}}), \qquad N_{\text{TPC}} = \frac{\beta_{pc}}{C_{p,\text{pc}}}\frac{\dot{Q}}{\dot{m}}. \tag{4.11}$$

In equation. (4.11), β_{pc}, $C_{p,\text{pc}}$ and h_{pc} are the volumetric coefficient of thermal expansion, the specific heat and the enthalpy of CO_2 at the p-c curve for the considered pressure, respectively. Furthermore, $h_{\text{b,h}}$ is the bulk enthalpy at the heater inlet. Dimensionless parameter N_{SUBPC} quantifies the relative distance of the operating point to the pseudo-critical line at the current pressure, or the degree of pseudo sub-cooling. At $N_{SUBPC} = 0$, the heater inlet flow would be at pseudo-critical temperature. N_{TPC} conveys the extent of the energy exchange with the CO_2 relative to the energy rate initially present in the flow. Effectively, N_{TPC} communicates the relative change in energy of the medium through the heat exchangers. Ambrosini and Sharabi (2008); Debrah et al. (2013) predict that beyond a certain value of N_{TPC},

where the thermophysical properties of the CO_2 change dramatically within the heat exchangers, the system is prone to unstable behaviour.

In the sections that follow, N_{TPC} and N_{SUBPC} are varied by adjusting the operating conditions and input parameters of the experimental facility to approach the stability boundaries discussed above.

4.3.2.2   Driving height (Δz)

To increase N_{TPC} towards the predicted boundaries of stability at a given thermody-namic point, either $\dot{Q}$ should be increased or $\dot{m}$ should be decreased. As the available heating rate $\dot{Q}$ is limited in the current facility, $\dot{m}$ was varied instead to substantially increase N_{TPC}. In this work, the mass flow rate of an NCL with a set diameter is inde-pendently decreased either by decreasing Δz, or by increasing the frictional resistance of the system by introducing a local loss.

The current section discusses the influence of reducing the mass flow rate $\dot{m}$ solely by varying Δz. The sensitivity to the inclusion of local resistances is discussed in section 4.3.2.3. To vary Δz in the current experiments, the moveable heaters (*mh* in figure 2.1) are moved vertically to impose various driving heights. Currently, driving heights of $\Delta z = 0.4, 0.6$, and 0.9 m are considered. Figure 4.5 shows the present experimental data in comparison with the stability maps presented in Debrah et al. (2013); Ambrosini and Sharabi (2008). As Δz is decreased, the mean value of N_{TPC} increases. Eventually, when Δz is reduced to 0.4 m, oscillatory behaviour is perceived throughout the system. For $\Delta z = 0.6$ or 0.9 m, a steady circulation results from the operation of the supercritical NCL. Therefore, in qualitative agreement with the linear stability maps shown in figure 4.5, increasing $\dot{m}$ by increasing Δz suppresses oscillations. However, the current limits of stability do not directly coincide with the numerically predicted boundaries. The present experiments show oscillations at lower values of N_{TPC}, outside of the unstable regions of figure 4.5. Therefore, a departure from stability of supercritical NCLs may occur before the predicted one-dimensional model limits are reached under the current conditions.

4.3.2.3   Local resistance (valve)

By including a local resistance to the natural circulation loop to reduce its mass flow rate, the system becomes stable. With a regulating valve in the NCL's cold section (immediately downstream of the cooler in figure 2.1), no oscillations could be induced in the system, regardless of the degree to which the valve was opened. Similarly, placing the Coriolis mass flow meter in the cold leg (below the valve in figure 2.1) prevented oscillations. As such, sustained oscillations were only observed
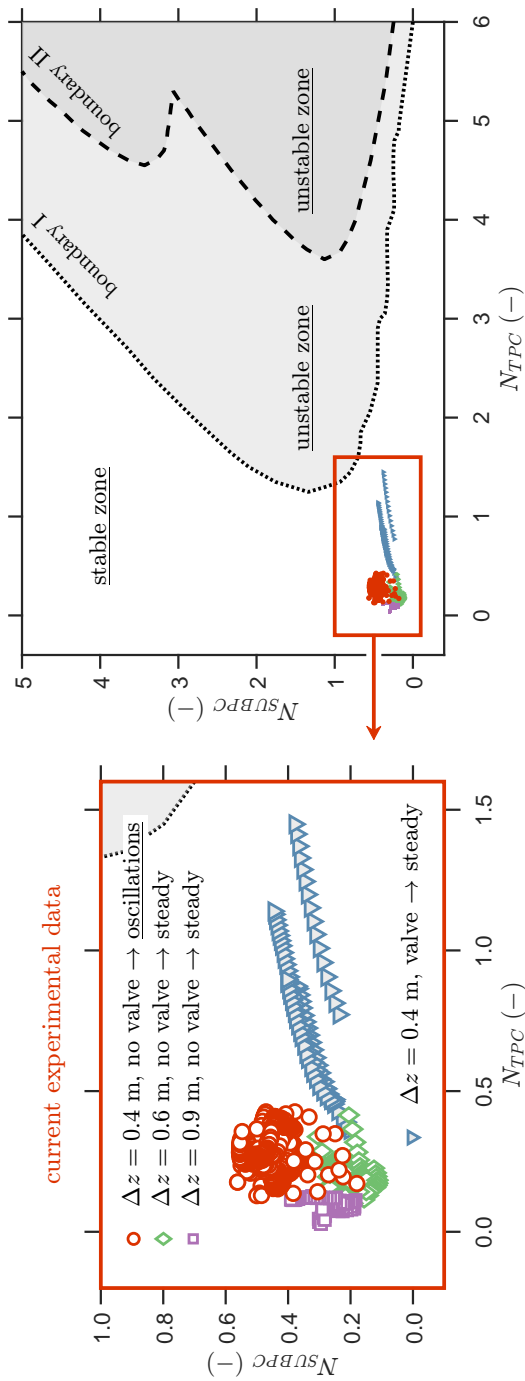
Figure 4.5: Non-dimensionalized parameter space map. The current experimental data is compared to the linear stability maps presented in Debrah et al. (2013) (boundary I) and Ambrosini and Sharabi (2008) (boundary II).
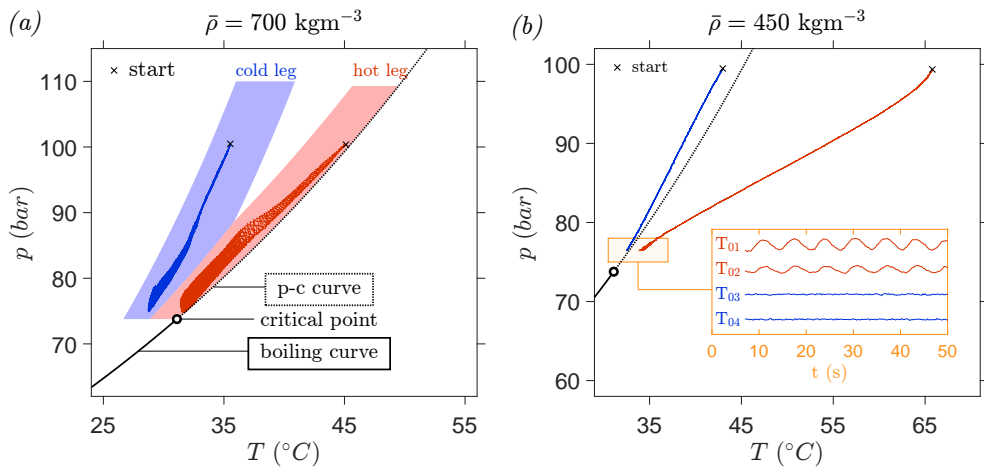
4

Figure 4.6: Example of oscillations in the hot leg (T_{01} & P_{01}, red) and the cold leg (T_{03} & P_{02}, blue) of the NCL at a mean density of *(a)* $\bar{\rho} = 700$ kgm^{-3} and *(b)* $\bar{\rho} = 450$ kgm^{-3}. *(b)* highlights the oscillations in T_{01}-T_{04} for $\bar{\rho} = 450$ kgm^{-3}. Within *(b)*, the y-scales ranges of T_{01}-T_{04} are identical. The cases show the growth of dynamic oscillations within the parameter space upon their inception at 100 bar. The coloured region in *(a)* indicates the thermodynamic region within which the sensitivity of the NCL is evaluated in this work.

when no resistive elements or flow obstructions were present. Therefore, the cold-side valve and the mass flow meter (both outlined in green in figure 2.1) were removed from the system for all other sensitivity experiments in this work.

The sensitivity of the NCL's transient to a local resistance highlights limitations to the established descriptions of the stability boundary, in which the boundary is only expressed using N_{TPC} and N_{SUBPC}. The experiments without resistive elements match the predicted trend in N_{TPC} qualitatively: a decrease in Δz increases N_{TPC} to a threshold value beyond which the natural circulation loop is no longer steady. However, as can be seen in figure 4.5, stability is maintained at significantly higher values of N_{TPC} upon the inclusion of a cold leg valve for the same driving height. Therewith, whereas the inclusion of a local resistance reduces the mass flow rate $\dot{m}$ effectively to increase N_{TPC}, it also affects the stability of the loop. Therefore, an additional parameter beyond N_{TPC} and N_{SUBPC} that takes into account the increased friction or mixing by the local resistance should be considered to describe the stability boundary of the supercritical pressure NCL.

4.3.2.4 Density (ρ)

The degree of pseudo-sub-cooling affects the stability of the system and the relative amplitude of the oscillations in the NCL. In this work, the density of the CO_2 is varied to change the degree of pseudo-sub-cooling, considering $450 \leq \bar{\rho} \leq 750$ kgm^{-3}. Digure 4.6 highlights the evolution of the oscillations along two distinct isochors within this parameter space. The two isochors are chosen such that the outlet conditions of either one of the two heat exchangers are in the direct vicinity of the pseudo-critical curve. At $\times$ in the figure, the oscillations are incited similarly to figure 4.2(a).

In figure 4.6(a), an oscillatory case with a mean NCL density of $\bar{\rho} = 700$ kgm^{-3} is considered. The figure shows the evolution of the fluctuations in temperature and pressure for the hot (T_{01}, P_{01}) and cold (T_{03}, P_{02}) sections of the loop, respectively. For the current isochor the heater outlet temperature T_{01} approaches the p-c curve. Under these conditions, the CO_2 is liquid-like, expanding rapidly upon its heating. Large oscillations arise from the non-ideal heater, propagating through the system to the cold leg, in accordance with figure 4.2(b). The thermodynamic range within which these system-wide oscillations are perceived for the current experiments is indicated using the coloured areas of figure 4.6(a). All data presented in this work, apart from the data shown in figure 4.6(b), were recorded within the indicated coloured region.

When the system density is reduced to $\bar{\rho} = 450$ kgm^{-3}, the NCL is less susceptible to oscillations. Figure 4.6(b) shows a typical attempt to incite oscillations in the natural circulation loop, consistent with the methods used for figures. 4.6(a) and 4.2(a). At the conditions of figure 4.6(b), the CO_2 is cooled towards (and across) the p-c curve. The magnitude of the fluctuations - if at all present - do not exceed the measurement noise of the sensors at $p \geq 80$bar. Below 80 bar, when the CO_2 is sufficiently non-ideal in the vicinity of the p-c curve at near-critical pressures, finite oscillations do appear. However, these oscillations are confined to the hot leg of the supercritical NCL, as is shown by the orange-outlined insert of figure 4.6(b). None of the current experiments show oscillations limited only to the cold section of the circulation loop.

As the density is changed from 700 kgm^{-3} to 450 kgm^{-3}, N_{SUBPC} is reduced to a near-zero value. The consequent stabilization of the system is therefore in qualitative agreement with the stability maps proposed by (Ambrosini and Sharabi, 2008; Debrah et al., 2013), which show an increased boundary value for N_{TPC} as N_{SUBPC} converges to zero.

4.3.2.5 Heating rate ($\dot{Q}$)

Changes to the applied heating rate modulate both the amplitude of the measured fluctuations, and their frequency. Figure 4.7 shows the evolution of the mean amplitudes
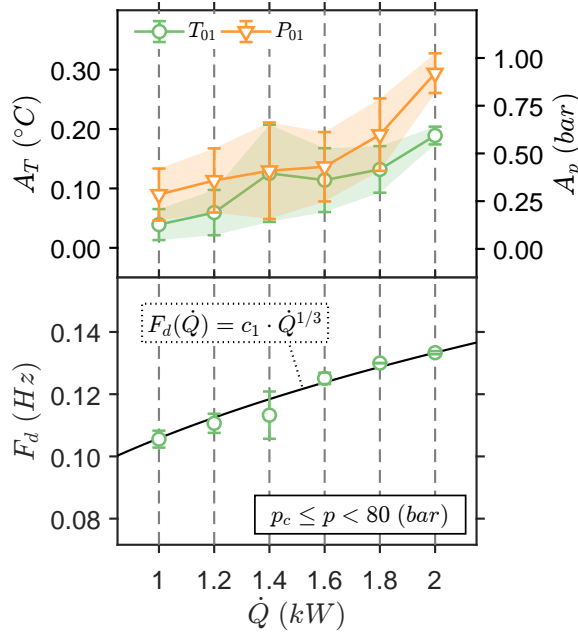
Figure 4.7: Sensitivity of oscillation amplitude in temperature data of T_{01} (green, left vertical axis) and pressure data of P_{01} (orange, right vertical axis) to the imposed heating rate $\dot{Q}$ in top subfigure. The bottom subfigure shows the sensitivity of the dominant oscillation frequency (evaluated for T_{01}) to the imposed heating rate $\dot{Q}$. The shaded region and the errorbars indicate the standard deviation ($\pm\sigma$) of the data.

A_{p} and A_{T} in temperature (T_{01}) and pressure (P_{01}) respectively, and the dominant oscillation frequency F_{d} when the heating rate in the heater $\dot{Q}$ is varied. As the heating rate $\dot{Q}$ is decreased from $\dot{Q} = 2$ kW, the value of N_{TPC} decreases. Consequently, the oscillation amplitudes decrease accordingly. Within the current parameter range, the amplitudes of the thermal and pressure oscillations decrease by approximately threefold when the applied heating rate is halved.

Any change in $\dot{Q}$ is furthermore observed to modulate the mean oscillation frequency throughout the loop, as shown in the bottom panel of figure 4.7 for NCL pressures within $p_{\mathrm{c}} < p < 80$ bar. As established in Swapnalee et al. (2012) and Draskic et al. (2024), the mass flow rate of an NCL at a supercritical pressure scales with $\dot{Q}^{1/3}$. In figure 4.7, the evolution of F_{d} is compared to $\dot{Q}^{1/3}$, by including curve $c_1 \cdot \dot{Q}^{1/3}$, where the value of c_1 is chosen such that the curve coincides with the mean experimental
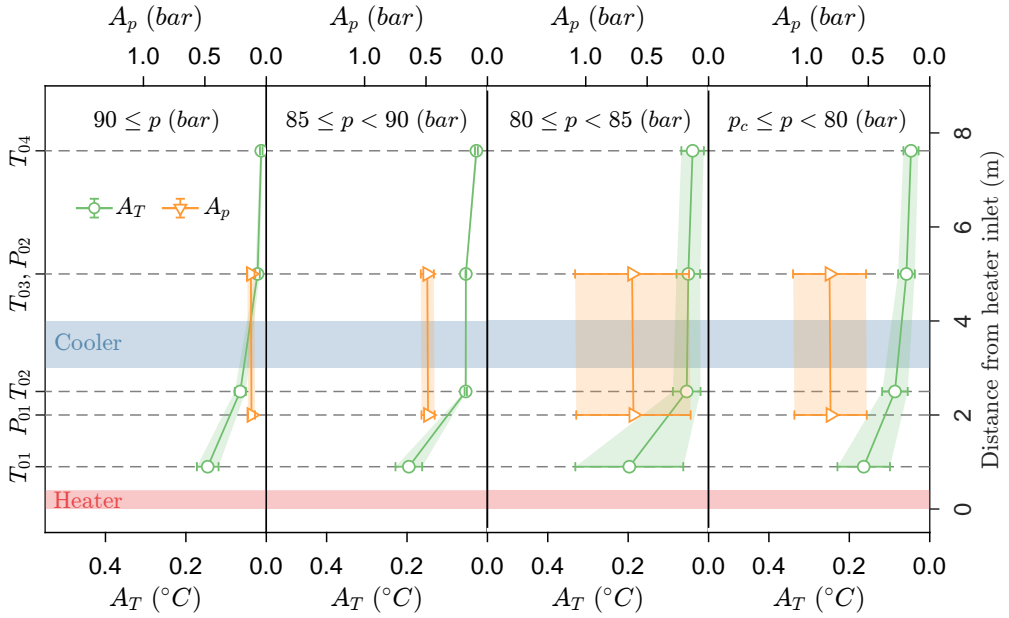
Figure 4.8: Mean oscillation amplitudes A_T of T_{01}-T_{04} (green, left vertical axis) and A_P of P_{01}-P_{02} (orange, right vertical axis), for $\dot{Q}$ = 2 kW. The shaded region and the errorbars indicate the standard deviation ($\pm\sigma$) of the data.

frequency at $\dot{Q}$ = 2 kW. Within the considered parameter range, the empirical oscillation frequency shows close agreement with the theoretical curve. For these conditions, the frequency of the NCL oscillations is assumed to scale with the mass flow rate of the CO_2.

4.3.2.6 Operating pressure (p)

An increase in operating pressure beyond the critical point increasingly dampens the oscillations in the NCL. Figure 4.8 shows the amplitude variations of temperature and pressure along the loop for various imposed pressure ranges. Consistent with the singular cases shown in figures. 4.2(a) and 4.6(a), the mean oscillation amplitudes throughout the loop shown in figure 4.8 decrease as the operating pressure of the system is increased. By increasing the pressure along an isochor, the value of N_{SUBPC} decreases, increasing the theoretical boundary value in N_{TPC} (Ambrosini and Sharabi, 2008; Debrah et al., 2013). Therewith, the current data is in qualitative agreement with the predicted stability boundaries. The decrease in oscillation amplitude is most notable in the pressure data for the current experiments. As thermodynamic

property gradients decrease with increasing pressures within the considered range (as is shown in figures 1.3(b)-(d)), the non-ideality in the heat exchangers decreases, consequently reducing the magnitude of the oscillations. The dampening of the temperature fluctuations is less apparent. Most notably, the cold-leg temperature amplitudes at T_{03} and T_{04} decrease beyond 90 bar. There, the oscillation amplitudes are of an equivalent magnitude as the measurement noise.

The oscillation amplitudes vary with increasing distance away from the heaters. Figure 4.8 shows the mean oscillation amplitudes as a function of the streamwise distance from the heater outlet for the respective pressure ranges. In line with case 1 of table 4.2 (shown in figure 4.2), the temperature sensor directly downstream of the heater (T_{01}) always shows the largest temperature fluctuations in the present study. Therewith, the previous hypothesis of traveling thermal waves is further supported. As the thermal fluctuations are advected away from T_{01}, they exchange heat with the thermally inert pipe walls and their surrounding CO_2, and experience turbulent mixing. As such, the temperature oscillation amplitudes (in green in figure 4.8) decay with increasing distance from the movable heaters. On the contrary, the pressure amplitude remains constant among P_{01} and P_{02}. A constant pressure amplitude is in support of the instantaneous redistribution of pressure resulting from a thermal imbalance of the system, as previously elaborated on in section 4.3.1.

4.3.2.7   Accumulator (accu.)

The inclusion of a piston accumulator to the current experiments results in minimal changes to the perceived oscillations. In figure 4.9, the influence of the accumulator on the NCL pressure is considered. Initially, the piston accumulator is connected to the main system which experiences system-wide oscillations similar to those shown in figure 4.2(b). At first, the accumulator contains approximately 0.95 l of compressible N_2. At $t = 256$ s, the CO_2 level within the accumulator is suddenly increased through the rapid removal of N_2. Consequently, the mean pressure of the system decreases quickly along the isentrope indicated in blue in figure 2.2. Thereafter, oscillations of equal frequency as the initial fluctuations emerge, and a new thermodynamic mean state is reached. Subsequently, at $t = 525$ s, the piston accumulator is disconnected from the NCL by abruptly closing the ball valve connecting the accumulator and the main loop in figure 2.1. As a result, an instantaneous but moderate increase in oscillation amplitude is observed. Nevertheless, the frequency of the oscillations within the NCL remains constant. As such, the presence of a compressible volume has led to negligible modulation of the stability of a supercritical NCL in the current experiments. However, the total accumulator volume with respect to the NCL volume is moderate in the current work. In Huang et al. (2024), a much larger accumulator
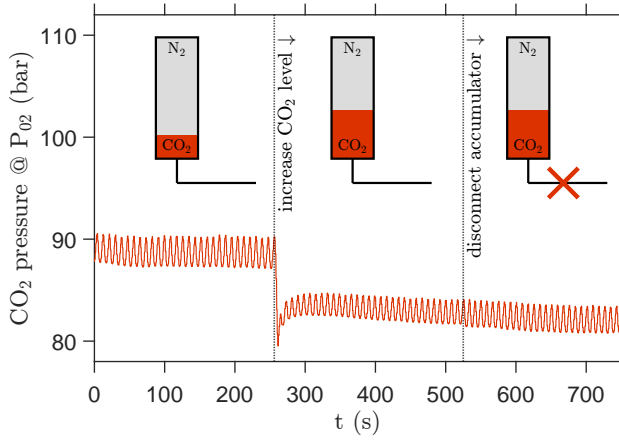
Figure 4.9: Typical effect of the movement of the accumulator piston on the oscillations within the NCL. Initially, at and before $t = 0$ s, the accumulator is connected to an oscillatory loop. At $t = 256$ s, N_2 is suddenly removed from the accumulator and the CO_2 level and vertical piston position consequently increase. At $t = 525$ s, the ball valve between the accumulator and the NCL is closed, disconnecting the accumulator from the rest of the system.

is used than in the current study, with 55 l of N_2 capacity. The oscillations in their experiments - albeit of a different type than the ones observed in the current study - were strongly affected by the inclusion of a pressurization accumulator.

4.3.3 Instability mitigation measures

The current experiments provide valuable insights into preventing and mitigating prolonged oscillations that can lead to equipment fatigue in high-throughput passive circulators at supercritical pressures. In oscillation-prone environments, narrowing the thermodynamic range that is spanned within the heater eventually stabilizes the supercritical NCL. Effectively, this is achieved by reducing N_{TPC}. The value of N_{TPC} can be reduced in experiments by increasing the mass flow rate (through an increase in Δz), or by decreasing $\dot{Q}$. Furthermore, the present variation in oscillation amplitudes suggests their dependence on the thermodynamic conditions. Within the considered thermophysical range of $450 \leq \bar{\rho} \leq 750$ kgm^{-3} and $73.7 \leq \bar{p} \leq 110.0$ bar, the oscillations were significantly weakened at higher pressures ($\bar{p} \geq 90$ bar) and lower densities ($\bar{\rho} \leq 500$ kgm^{-3}), where the value of N_{SUBPC} approached zero. There, the property gradients within the heater are reduced by moving away from the p-c curve to a lower density, or by increasing the pressure. A more substantial stabilization of

the system is achieved through the impedance of the travelling thermal waves within the system. If the thermal pockets are diffused within the system, for instance by mixing in a parallel-channel plate heat exchanger (T'Joen and Rohde, 2012), they no longer affect the NCL velocity to incite a subsequent pocket, and the oscillations are not sustained. Furthermore, the inclusion of a local resistance (a valve or a mass flow meter) decreases the system's sensitivity to accelerations by the thermal waves, beside inducing additional diffusion by mixing near the valve. Thereafter, the formation of the thermal waves is no longer re-incited.

4.4   Proposed instability mechanism

The observed traveling thermal waves are driven by non-ideality in the heaters. With increasing streamwise distance from the movable heaters in figure 4.7, the amplitude of the temperature oscillations consistently decrease. Within the loop, the oscillations are the strongest directly after the heaters at sensor T_{01}, regardless of the operating pressure, heating rate and density. Furthermore, the current experiments never show oscillations that are limited only to the cold leg of the NCL. On the contrary, as is shown in figure 4.6, oscillations exclusive to the hot leg do occur. As discussed in section 4.3.1, the in-phase pressure oscillations are believed to be induced by the thermal (de)compression of the supercritical pressure CO_2. In the heaters, a constant heat flux is electrically applied. For such a constant $\dot{q}$, the heat transfer must deteriorate and enhance subsequently to cause the heat imbalance that drives the thermal (de)compression of the system. Upon the deterioration of the heat transfer, heat is removed less effectively from the heater, and the heater wall temperature increases. As the heat transfer is restored thereafter, the CO_2 is heated at an increased rate, and a low-density 'pocket' is formed. At the same time, the system is thermally compressed, increasing the pressure along the current isochor.

The process through which non-ideality is induced in the heaters is not of the static type. Using the steady model introduced in section 4.2.2, the static stability of the NCL heat exchangers is assessed. Figure 4.10 shows the viscous drag curves of the heat exchangers for several discrete heating rates within the experimentally considered range. As shown in figure 4.10(a), the criterion of equation. (4.1) is not satisfied when an ideal viscous model for which $f_{ni} = 1$ is used within the movable heaters. Then, Δp_v increases progressively for all considered values of $\dot{Q}$, and only one steady state exists for a constant driving pressure. However, the criterion of equation. (4.1) can be satisfied with a sufficiently non-ideal viscous loss model. Given equation. (4.3), the overall friction coefficient f should scale with $\dot{m}^\gamma$, where $\gamma \leq -2$, to model viscous losses that decrease as a function of $\dot{m}$ and therefore satisfy
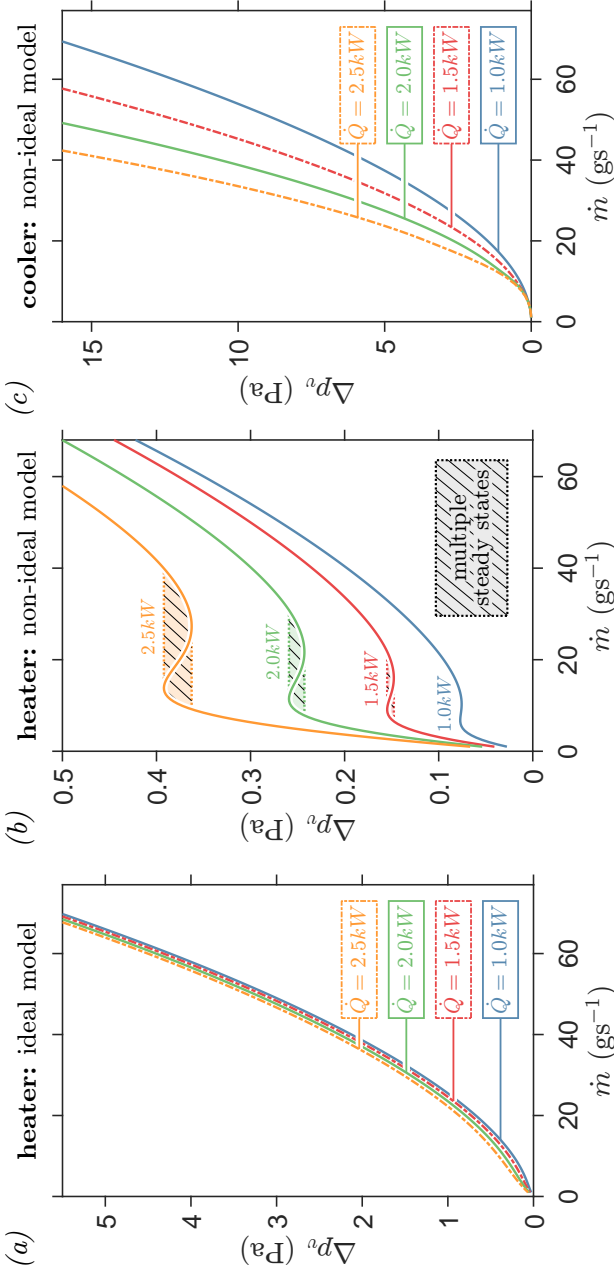
Figure 4.10: Steady state analysis of forced flow through movable heaters (mh), with inlet pressure $P_{\text{in}} = 80$ bar and inlet bulk density $\rho_{\text{b,in}} = 700$ kgm^{-3}. The values of the viscous drag through the heater, as modelled using an ideal friction model ($f_{\text{ni}} = 1$ in equation. (4.3)) or a simplified non-ideal friction model (f_{ni} from equation. (4.8)) are shown in subfigures (a) and (b), respectively. The viscous drag through the cooler, as modelled using an equivalent simplified non-ideal friction model is shown in subfigure (c).

the criterion in equation. (4.1). Figure 4.10(b) shows a hypothetical viscous loss model for which the heater has multiple steady states. The model assumes $\alpha = -0.2$ and $\beta = 3.0$ (satisfying $\gamma < -2$) for f_{ni} in equation. (4.8), for which the modulation of the viscous losses is dominated by the near-wall decrease in viscosity. Given an environment with sufficient perturbations, the steady curves shown in figure 4.10(b) could yield behaviour that is qualitatively similar to the current oscillations. The limit cycle oscillations between steady states within the hatched areas of figure 4.10(b) would increase in amplitude for increasing heating rates $\dot{Q}$, in line with the results of figure 4.7. Additionally, the extension of the model to the cooler with $\alpha = 0.2$ and $\beta = 3.0$ (shown in figure 4.10(c)) yields the static stability of the cooler under the same operating conditions, in line with the current experiments in which fluctuations only arise from the movable heaters. However, the values of coefficients α and β required to achieve a static instability are far beyond what has been empirically reported to date (Fang et al., 2012; Ehsan et al., 2018; Fang et al., 2020). Additionally, the static model of the heater does not change upon the inclusion of the regulating valve, although the stability is greatly affected by the addition of the local resistance in experiment. Therefore, the current oscillations cannot be the direct consequence of only a static instability.

Instead, the non-ideality in the movable heaters is likely triggered by a dynamic feedback mechanism within the system. One such feedback mechanism was proposed by Welander (1967) for a sub-critical fluid. There, sustained oscillations arise from the subsequent acceleration and deceleration of the NCL after the formation of thermal waves. A full oscillation cycle is completed when a thermal wave, that is formed by the modulation of the heater residence time, passes through the system. Therewith, the oscillation frequency depends on the mass flow rate of the system. As argued in section 4.3.2.5 and with the bottom panel of figure 4.7, the current oscillation frequency scales with the NCL mass flow rate, in support of the mechanism. Furthermore, the present density waves affect the distribution of density within the vertical legs of the NCL, modulating the velocity of the natural circulation. There, a sudden system-wide deceleration of CO_2 could trigger a deterioration of the heat transfer in the heaters. Subsequently, as the resulting density wave reaches the cold vertical leg, the system accelerates and the heat transfer would recover. Once the density wave reaches the hot leg again, a system-wide deceleration follows, inducing the current cyclic behaviour. Additionally, the inclusion of a local loss reduces the acceleration of the system upon a redistribution of its driving density. Furthermore, the local loss increases mixing, diffusing the traveling thermal wave as it passes. Therewith, the initial conditions for the cyclic deterioration may no longer be met when a valve is present, in line with the current experiments.

4.5   Conclusions

In this chapter, the stability of a natural circulation loop (NCL) with carbon dioxide at supercritical pressures is experimentally investigated. Such supercritical pressure NCLs offer high-throughput passive circulation without mechanical propulsion, making them highly desirable for cooling in critical applications, including nuclear reactors and solar thermal systems. However, instabilities similar to those seen in two-phase systems can arise in supercritical NCLs at large throughputs, leading to undesirable oscillatory behaviour. Such prolonged oscillations can lead to mechanical fatigue, which is particularly dangerous given the high-pressure environment of supercritical NCLs.

The current work employs an NCL with a vertical-heater-vertical-cooler configuration in which CO_2 is circulated at supercritical pressures. To study the transient of the system, its temperature and pressure are recorded at multiple locations throughout the loop. In search of oscillations, the vertical position of the heaters, the system's thermodynamic state and heating rate, and the presence of a compressible volume or local resistance are varied within the current experiments. Additionally, the experimental results are compared to a static analysis of the NCL to assess whether the potential existence of multiple steady states in the non-ideal heat exchangers in particular drives the recorded fluctuations.

When sufficiently large thermophysical variations are induced in the heat exchangers of the NCL, the loop converges to a system-wide oscillatory state. To reach an oscillatory state in the present study, the mass flow rate of the NCL is decreased by reducing the vertical distance between the cooler and the movable heaters. Then, oscillations are recorded even before the stability limits as predicted by linear one-dimensional analyses are reached. The structural decay in temperature fluctuation amplitudes away from the movable heaters for any of the considered isochors indicates that the fluctuations are initiated at the heaters. The transient heat transfer that occurs in the heaters generates system-wide pressure oscillations, and travelling density waves that manifest as out-of-phase fluctuations in temperature throughout the loop. As the pressure of the system is increased to less non-ideal isobars, the oscillation amplitudes decrease. Conversely, the oscillations intensify at larger heating rates. Furthermore, an increase in heating rate increases the oscillation frequency at a rate equal to the increase in mass flow rate. Qualitatively, the present experiments match the behaviour of a system with multiple steady states. However, as the non-ideality in the heaters that is required to induce multiple steady states under the current conditions exceeds any previous reports, the oscillations are not believed to be incited by a static stability. Instead, the current oscillations are argued to be dynamic. There, the feedback

4

between the heat transfer in the heaters and the velocity of the NCL, modulated by a transient redistribution of density along its vertical legs, is believed to incite the current oscillations. The full stabilization of the system upon the inclusion of a local resistance in its cold leg supports the presence of a dynamic feedback mechanism.

The present work emphasizes the necessity for further investigations into the mechanism that triggers the current Density Wave Oscillations (DWOs). Whereas the current results suggest the presence of a dynamic feedback mechanism, the exact nature of the feedback mechanism is not directly measured in the experiments. A more in-depth understanding of the onset of the current oscillations and their interaction within the NCL could aid in developing effective mitigation strategies that ensure the safe and effective operation of prospective cooling systems of fluids at supercritical pressure. For instance, optical measurements or three-dimensional models of the heaters could aid in predicting the onset of the cyclic deterioration of their heat transfer. Furthermore, the existing non-linear models could be extended to include non-idealities in the heat exchangers and the decay and mixing of the density wave through the system. Additionally, further research on the use of accumulators with a substantial volume relative to the NCL would provide valuable insights into how compressible volumes impact and potentially reduce oscillatory behaviour.

4

Chapter 5

The stability of stratified horizontal flows of CO_2 at supercritical pressures[1]

Fluids at supercritical pressures exhibit large variations in density near the pseudo-critical line, such that buoyancy plays a crucial role in their fluid dynamics. In this chapter, we experimentally investigate heat transfer and turbulence in horizontal hydrodynamically developed channel flows of carbon dioxide at 88.5 bar and $32.6°C$, heated at either the top or bottom surface to induce a strong vertical density gradient. To visualize the flow and evaluate its heat transfer, shadowgraphy is used concurrently with surface temperature measurements. With moderate heating, the flow is found to strongly stratify for both heating configurations, with bulk Richardson numbers Ri reaching up to 100. When the carbon dioxide is heated from the bottom upwards, the resulting unstably stratified flow is found to be dominated by the increasingly prevalent secondary motion of thermal plumes, enhancing vertical mixing and progressively improving heat transfer compared to a neutrally buoyant setting. Conversely, stable stratification, induced by heating from the top, suppresses the vertical motion leading to deteriorated heat transfer. The optical results provide novel insights into the complex dynamics of the directionally dependent heat transfer in the near-pseudo-critical region. However, the results also highlight the need for further progress in the development of experimental techniques to generate reliable reference data for a broader range of non-ideal supercritical conditions.

5.1   Introduction

At a supercritical pressure, the fluid dynamics of heated or cooled fluids are often strongly affected by buoyancy. In this complex thermodynamic region, moderate heating rates can already induce significant variations in density that lead to sharp, local flow accelerations or mixed convection when buoyancy becomes significant. Therefore, heat transfer in engineering application, which operate with supercritical fluids, often depends on the direction of gravity. These effects can be significant, as noted in the review on heat transfer at supercritical pressure by Wang et al. (2023a). In their work, a comparison of the empirical heat transfer rates of various experimental facilities showed that heat transfer rates can either increase or decrease (depending on the direction of the heat transfer) by up to an order of magnitude with respect to a neutrally buoyant setting. This effect is most notably prevalent in horizontal flows with vertical gradients of density, in which turbulence can be either enhanced or suppressed by buoyancy. In such settings, in particular with fluids in proximity of the pseudo-critical region, it is essential to understand how buoyancy modulates the flow and turbulence to accurately capture and predict trends in heat transfer.

So far, mixed convection has been studied extensively (Pirozzoli et al., 2017; Zonta and Soldati, 2018; Caulfield, 2021) for fluids that follow the Oberbeck-Boussinesq (OB) approximation (Oberbeck, 1879; Boussinesq, 1897). Contrary to a fluid at a supercritical pressure, the density of OB fluids is assumed to vary only moderately and linearly with temperature. Therefore, large temperature differences or large length scales are required to induce strong stratifications in the conventional single-phase fluids that are accurately described with the OB approximation (Zonta and Soldati, 2018).

The unstable stratification of a horizontal flow of an OB fluid, in which a lighter layer is formed below a denser bulk flow, is characterized by ejections of warmer fluid away from the heated wall, and the concurrent sweeping of colder fluid in the opposite direction (Garai et al., 2014). However, unlike in purely convective flows, the ejected plumes form roll vortices towards the bulk of the channel in the direction of the forced convection (Garai et al., 2014; Scagliarini et al., 2014; Pirozzoli et al., 2017). In the direct numerical simulations (DNS) of Garai et al. (2014), the wide roll vortices are seen to align after one another in the streamwise direction. Furthermore, the DNS of both Li et al. (2017) and Zonta and Soldati (2014) have shown that the intensity of the near-wall turbulence and the mixing efficiency increase when roller ejection and sweep processes are incited in a previously neutrally buoyant channel flow. Here, the improvements in mixing efficiency are diminished as the relative strength of the forced convection is increased (Zonta and Soldati, 2014). Moreover, the concurrent

5

processes in which rollers are ejected from and swept towards the bottom surface become the dominant mechanism of wall-normal heat transfer in mixed convective flows (Garai et al., 2014; Blass et al., 2020). As such, the wall-fluid heat transfer of flows with buoyant plumes differs from - and far exceeds - the heat transfer of neutrally buoyant forced convection.

Distinctly different behaviour is observed and simulated in stably stratified flows of OB fluids, in which a lower density layer is formed on top of a denser bulk flow. Here, fluid parcels of a certain density are preferentially redistributed along the vertical density gradient that is imposed on the flow (Lienhard V and Van Atta, 1990). If the gradient is sharp enough, the potential energy required to stir fluid parcels away from their preferential vertical positions is not met (García-Villalba and Del Alamo, 2011). As a result, overturns and vertical thermal structures are elongated and eventually aligned with the direction of the flow (Williams et al., 2017; Smith et al., 2021; Zonta et al., 2022). The resulting restriction of vertical momentum transfer has been noted to greatly reduce turbulent mixing and near-wall heat transfer (Ohya et al., 1997; García-Villalba and Del Alamo, 2011; Williams et al., 2017), in both numerical studies and experiments. Often, the distinction is made between weak and strong stratification, following the findings of Gage and Reid (1968). In the weak limit, turbulence is sustained close to the wall where shear overcomes buoyancy (Zonta et al., 2022), as the latter preferentially acts on larger scales of vertical motion (Lienhard V and Van Atta, 1990; Zonta and Soldati, 2018). In the case of strong stratification, a global turbulent state cannot be sustained (Nieuwstadt, 2005; Zonta and Soldati, 2018). The flow is said to become intermittent, with regions of complete turbulence suppression. For higher values of the Reynolds number the formed laminar patches are more confined to the top wall, instead of spanning the entire domain, according to the results of Deusebio et al. (2015).

Unfortunately, the amount of works that consider the stratification of fluids with thermodynamic gradients beyond the limits of the Oberbeck-Boussinesq approximation has so far remained limited. However, it is with such fluids, most notably so for fluids at a supercritical pressure, that strong stratifications most readily prevail in practical applications. The influence of buoyancy on the flow of a fluid at a supercritical pressure have been studied in the context of vertical pipe flows (Bae et al., 2005; Nemati et al., 2015) and for vertical annular flows (Peeters et al., 2016). Additionally, Valori et al. (2019) have optically explored a purely convective flow of supercritical carbon dioxide. The effect of buoyancy on a horizontal supercritical flow has first been considered by Chu and Laurien (2016). In their work, Chu and Laurien (2016) have numerically (DNS) investigated the non-axisymmetric temperature profiles in heated horizontal pipe flows previously found in experimental investigations of pipe

5

surface temperatures (Adebiyi and Hall, 1976; Yu et al., 2013; Tian et al., 2021; Cheng et al., 2024). Here, the overall deterioration in heat transfer with respect to a neutrally buoyant flow (Theologou et al., 2022; Cheng et al., 2024) was attributed to the accumulation of a light, warmer layer at the top of the horizontal pipe (Chu and Laurien, 2016). Furthermore, the thermal stratification of the flow of a supercritical fluid through a heat exchanger channel has been touched upon in the DNS of Wang et al. (2023b). Here, the initially turbulent flow was predicted to laminarize along the imposed density gradient, subsequently deteriorating its wall-normal heat transfer. A first experimental investigation of horizontal buoyancy-affected flows of supercritical CO_2 was presented by Whitaker et al. (2024). Here, side-view schlieren imaging was used to study the flow within a heated microchannel. In their work, the optical signal was greatly affected by the direction of the heat transfer. Nevertheless, only a moderate difference between the heat transfer of the bottom-up heated surface and the top-down heated surface was measured for their operating conditions. Therewith, the effects of strong stratifications on the heat transfer of continuous, mixed convective flows at supercritical pressures remain experimentally unexplored.

The current chapter experimentally investigates horizontal flows of carbon dioxide at supercritical pressure in which buoyancy is non-negligible, or even becomes dominant. More specifically, initially hydrodynamically developed steady horizontal channel flows are considered, subject to one-sided heating such that vertical gradients of density are induced. The large, non-ideal variations in thermodynamic properties of the heated carbon dioxide make that the Oberbeck-Boussinesq approximation does not apply, and that significant buoyant contributions can be induced at the moderate heating rates that are attainable in laboratory scale experiments. As such, the modulation of turbulence in both stably and unstably stratified channel flows can be addressed in the current work.

To visualize the stratifications of carbon dioxide at supercritical pressure, the surface temperature measurements are complemented with optical diagnostics in this work. The optical tools exploit variations in refractive index in the working fluid to visualize the thermally inhomogeneous turbulent carbon dioxide. Contrary to the investigations of wall temperature, the resolution of these optical measurements is not limited in time by the thermal inertia of the system, or in space by the finite physical size of probes and probe wells. Therewith, the current optical methods can partially fill the knowledge gap left by the incompatibility of high-frequency hot-wires with non-ideal media (Vukoslavčević et al., 2005). As such, the qualitative visualisations are used to explain trends in the wall temperature data by revealing highly intermittent local flow patterns previously unexplored in experiments with fluids at supercritical pressures.

A description of the experimental methodology is given in §5.2. In §5.3.2, an

overview is given of the explored parameter range. In §5.4, the applicability of the optical diagnostics is first evaluated by considering the unheated base flow. Thereafter, visualisations of heated channel flows in both stably and unstably stratified configurations are presented and discussed. Furthermore, surface temperature data are presented for both configurations. Finally, a summary of the most important conclusions is presented in §5.5. At the end of this document, supplementary information on the used optical filters is given in appendix 5.A.

5.2 Methodology

5.2.1 Experimental facility

In this work, the stratification of a non-ideal fluid is studied experimentally in a novel test facility that provides optical access to a continuous flow of carbon dioxide at supercritical pressures. The flow to the optical test facility is provided by a natural circulation loop, as described in chapter 2. The experimental facility is shown schematically in figure 2.3 and an overview of the geometric parameters is given in table 2.2.

5.2.2 Shadow image velocimetry

A comparison of consecutive shadowgrams, captured with the configuration described in section 2.3.2.1, is used to reveal flow patterns within a compressible flow in this chapter. When the currently studied flow is both turbulent and refractive, it is naturally seeded by eddies that travel at the local convective speed of the flow. As such, the correlation of consecutive shadowgrams enables seedless velocity measurements of the flow (Jonassen et al., 2006; Hargather et al., 2011; Settles and Hargather, 2017). In order for the pseudo-tracers to be distinguishable in consecutive images, thermal gradients should be sparsely distributed along the optical axis, and the diffusive timescale of the flow should far exceed its advective timescale. The applicability of shadow image velocimetry to turbulent flows of carbon dioxide at supercritical pressure in particular was previously demonstrated by Okamoto et al. (2003). Whereas Particle Image Velocimetry (PIV) can yield near-planar velocities, the integrating property of shadowgraphy yields measurements of eddy motion across the full width of the test section when using shadow image velocimetry. Much like planar PIV, shadow image velocimetry only yields displacements in directions perpendicular to the optical axis. In the current work, a fast-Fourier-transform-based cross-correlation algorithm is used to yield displacements between consecutive shadowgrams. An interrogation window size of 128×128 pixels with 80% overlap is used to capture a

sufficient amount of property-variant structures in each correlation window (Jonassen et al., 2006). The qualitative descriptions of the shadowgram pair displacements in this work are supported by an additional assessment of the image correlation profiles themselves, as elaborated on in appendix 5.B

5.2.3   Experimental procedure

As carbon dioxide dilates strongly for the conditions and flow rates of the current study, all data is gathered by following a measurement procedure that aims to minimize thermal gradients within the test section block itself. The test section is initially at the ambient temperature. In order to increase its temperature to the desired value, a large mass flow rate of carbon dioxide at the appropriate temperature is forced through the thermally insulated test section for several hours. Over time, the measured temperature drop over the test section $(T_{03} - T_{04})$ reduces, as the temperature of the test section converges towards a steady state. When changing the inlet condition to reach different operating conditions, the procedure to reach steady state is repeated.

When the test section temperature reaches a value sufficiently close to the desired test section inlet temperature, therewith at a value of $(T_{03} - T_{04})$ within the nominal accurary of T_{03} and T_{04}, a measurement cycle is commenced. At a constant mass flow rate, the imposed foil heating rate is gradually increased in a stepwise manner. In order to maintain a constant pressure and mass flow rate $\dot{m}$, the applied heating rate to drive the natural circulation loop is gradually decreased. The acquisition of images and loop sensor data is started some time t_w after imposing each step in heating power. In the current work, $t_w = 120$ s. After the completion of all heating steps, the mass flow rate is changed, and the above process is repeated.

5.3   Cases and parameter space

5.3.1   Thermodynamic conditions

All presented results are recorded at the same thermodynamic conditions at the test section inlet, whereas the imposed heating rates and the applied mass flow rates are varied throughout this work. The nominal thermodynamic state of the test section inlet (T_{03} and P_{02} in figure 2.3) of the current study is indicated in figure 5.1. The full thermodynamic range that was initially explored is indicated in grey in figure 5.1.

Within the considered thermodynamic range, channel inlet conditions that are liquid-like provide the most distinguishable shadowgrams. Therefore, such conditions are chosen as the initial state for the current experiments. On the contrary, images of near-pseudo-critical and gas-like neutrally buoyant carbon dioxide reveal the intermittent
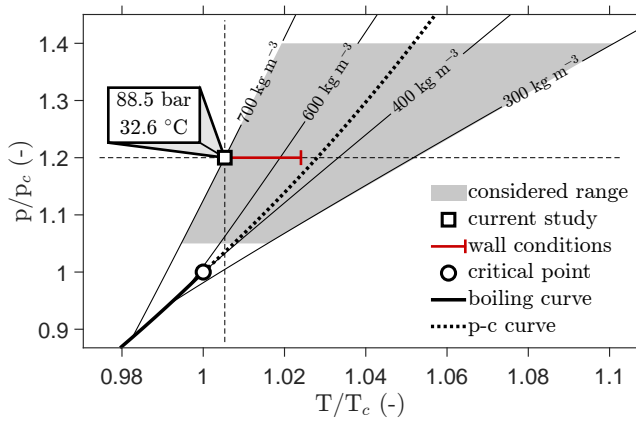
Figure 5.1: Range of thermodynamic conditions of carbon dioxide at the test section inlet for the current study. Any presented results are evaluated at a nominal density and a nominal pressure of $\rho = 700$ kg m^{-3} and $p = 1.2\ p_c$, respectively. Here, p_c is the critical pressure.

presence of blurry, irregular, downward moving structures. Whereas downward plumes are similarly perceived when the CO_2 is denser, they are less prevalent, their presence is more sporadic and their outlines remain sharp in a shadowgram. These secondary flows are likely the result of the moderate cooling of the carbon dioxide by the ambient air, either through the insulated walls of the test section, or via the less insulated optical visors. Within the considered domain, the temperature of the carbon dioxide at the test section inlet exceeds the ambient temperature. On the right side of the pseudo-critical curve in figure 5.1, the driving temperature difference with the surroundings is relatively large. Furthermore, the cooling of the gas-like medium brings about sharp changes in refractive index in the steep, non-linear near-pseudo-critical region. To the left of the p-c curve, both the driving temperature of the cooling by the ambient and the thermodynamic gradients induced by the cooling are significantly lower. Therewith, the moderately colder structures in the flow do not sufficiently distort the light through the channel to blur the resulting image in the liquid-like region of the considered thermodynamic parameter range.

Additionally, the large near-pseudo-critical gradients in density that are induced when the liquid-like carbon dioxide is heated, make that strong stratifications can be reached with the attainable experimental heating rates. The range of measured surface temperatures T_{s1} and T_{s2} is indicated using the red horizontally bounded line in figure 5.1. For the presented results, the pseudo-critical curve is not crossed in the near-wall region.
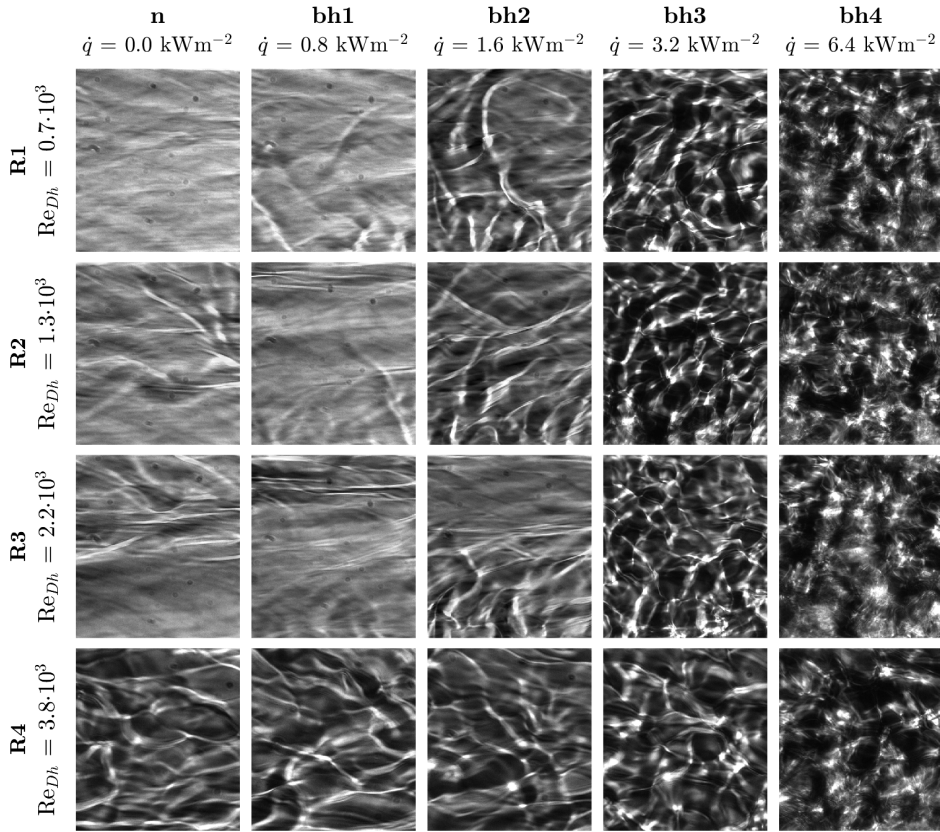
Figure 5.2: Instantaneous shadowgrams of bottom-heated channel flows of carbon dioxide at the thermodynamic conditions indicated in figure 5.1. The relevant nominal Reynolds numbers $_{Dh}$ and the nominal imposed heating rates $\dot{q}$ are displayed on the vertical and the horizontal axes, respectively. The cases, e.g. R2:bh1, are labeled by an indicator of the nominal Reynolds number (**R**) and an indicator of the applied heating (**n** or **bh**). Here, **n** represents an unheated flow, whereas **bh** implies that bottom-upward heating is applied. In all cases, the flow is from left to right.

5.3.2   Case overview

An overview of the cases considered in this work is given in figures 5.2 and 5.3. Both figures show instantaneous shadowgrams of carbon dioxide at supercritical pressure. In figure 5.3, the carbon dioxide is heated in the top-down configuration shown in orange outlined cross section **A** of figure 2.3. For the cases shown in figure 5.2, the test section is inverted and the bottom surface of the test section channel is heated. In
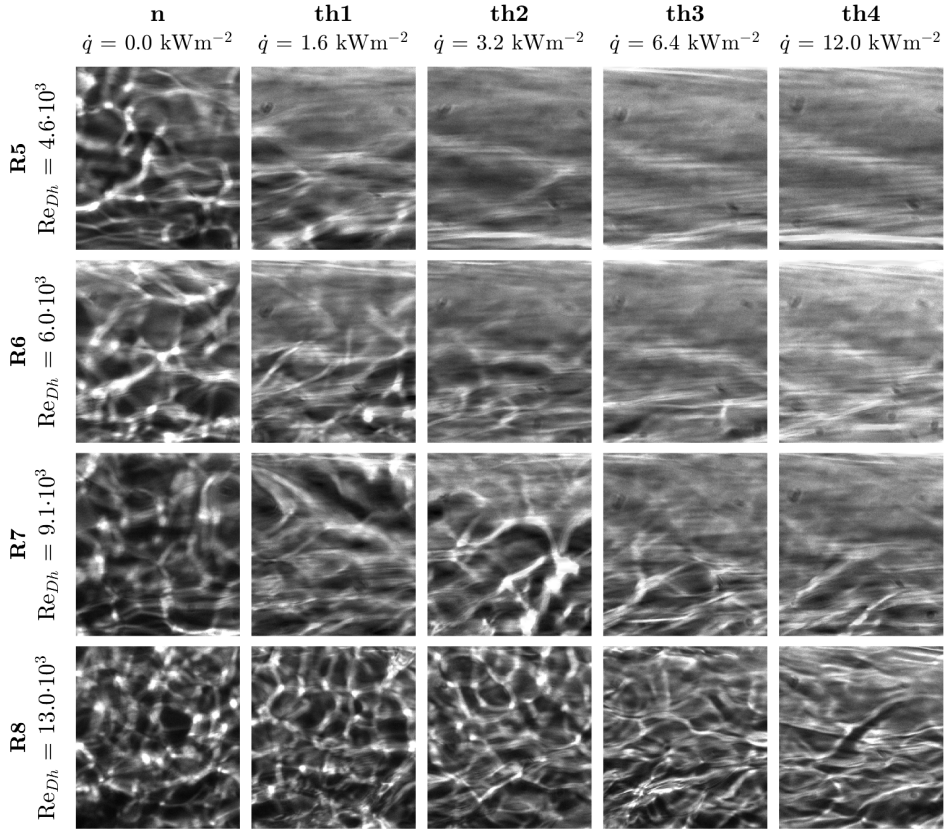
Figure 5.3: Instantaneous shadowgrams of top-heated channel flows of carbon dioxide at the thermodynamic conditions indicated in figure 5.1. The relevant nominal Reynolds numbers $_{Dh}$ and the nominal imposed heating rates $\dot{q}$ are displayed on the vertical and the horizontal axes, respectively The cases, e.g. R6:th1, are labeled by an indicator of the nominal Reynolds number (**R**) and an indicator of the applied heating (**n** or **th**). Here, **n** represents an unheated flow, whereas **th** implies that top-downward heating is applied. In all cases, the flow is from left to right.

both figures, the inlet mass flow rate $\dot{m}$ and the foil heating rate $\dot{q}$ are varied to yield twenty cases with varying hydraulic Reynolds numbers Re_{Dh} and bulk Richardson numbers Ri respectively, where

$$Re_{Dh} = \frac{\rho_{b1} U_{imp} D_h}{\mu_{b1}}, \quad Ri = \frac{\rho_{b1} - \rho_w}{\rho_{b1}} \cdot \frac{gh}{U_{imp}^2}. \tag{5.1}$$

Here, the inlet density ρ_{b1} and the inlet viscosity μ_{b1} are evaluated at the temperature

	bh1	bh2	bh3	bh4
R1	12.64 ± 2.42	15.53 ± 3.18	16.13 ± 4.03	19.48 ± 5.57
R2	3.33 ± 1.80	6.41 ± 1.85	12.13 ± 1.96	14.91 ± 1.98
R3	4.13 ± 0.89	4.96 ± 0.69	7.90 ± 0.91	9.69 ± 0.67
R4	0.86 ± 0.45	1.66 ± 0.68	2.62 ± 0.37	3.58 ± 0.37
	th1	**th2**	**th3**	**th4**
R5	1.49 ± 0.23	2.38 ± 0.15	5.28 ± 0.23	11.51 ± 0.34
R6	0.78 ± 0.14	1.19 ± 0.09	2.75 ± 0.17	6.69 ± 0.24
R7	0.35 ± 0.07	0.61 ± 0.06	1.05 ± 0.07	2.54 ± 0.11
R8	0.15 ± 0.03	0.26 ± 0.03	0.48 ± 0.02	1.26 ± 0.05

Table 5.1: Values of Ri for the non-neutrally buoyant snapshots shown in figures 5.2 and 5.3. The cases, e.g. R1:bh1, are labeled by an indicator of the nominal Reynolds number (**R**) and an indicator of the applied heating (**bh** or **th**). Here, **bh** represents a flow to which bottom-upward heating is applied, whereas **th** indicates that top-downward heating is applied. The data is shown with intervals of $\pm 2\sigma$.
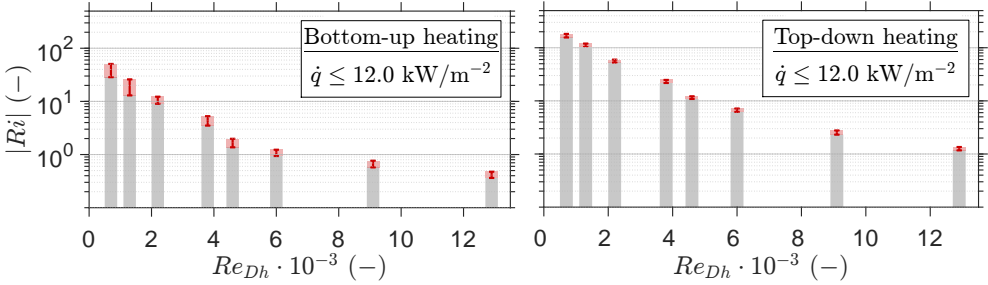

Figure 5.4: Range of Ri considered in this work for the nominal Reynolds numbers Re_{Dh} indicated in figures 5.2 and 5.3. The carbon dioxide is heated in the unstably stratified configuration on the left, whereas a stably stratified configuration is considered for the data on the right. The errorbars correspond to $\pm 2\sigma_{Ri}$ of the time series with the largest value of Ri.

and pressure of sensors T_{03} and P_{02} of figure 2.3, respectively. Thereafter, ρ_{b1} is used to evaluate the imposed bulk velocity U_{imp}, with

$$U_{\mathrm{imp}} = \frac{\dot{m}}{\rho_{b1} A_{\mathrm{cs}}}. \tag{5.2}$$

Here, the test section cross-sectional flow area is defined as $A_{cs} = hw$. The bulk Richardson number is evaluated using wall density ρ_w. Under the assumption of constant test section pressure, ρ_w is evaluated at P_{02} and the mean wall temperature T_w, where

$$T_w = \frac{1}{2}\left(T_{s1} + T_{s2}\right). \tag{5.3}$$

The corresponding values of Ri for the non-neutrally buoyant cases shown in figures 5.2 and 5.3 are given in table 5.1. The complete range of Ri obtained with the available surface heating power is presented in figure 5.4. As the hydraulic Reynolds number Re_{Dh} is increased, the attained value of Ri decreases. Furthermore, at a constant heating rate, the measured value of Ri is consistently higher for the top-down heated configuration than it is for bottom-up heating.

5.4 Results

5.4.1 Characterisation of unheated base flow

For the conditions considered in this work, structures that are naturally present in the channel can be perceived in the shadowgrams and persist throughout consecutive frames. Due to turbulent mixing and the thermal heterogeneity of the fluid, the density of the operating fluid changes locally. Consequently, the refractive index also changes. The variation in the (second derivative of the) refractive index in the carbon dioxide throughout the channel is then registered by the shadowgraphy. In the shadowgrams, the variations manifest as fluctuations in the image brightness. These structures have a finite lifetime while being advected by the flow; they appear then as 'thermal tracers' that visualize the fluid motion. Provided that these structures remain to exist over at least one imaging frame pair, they can be considered as (nearly) passive tracers in the fluid that can be used to measure the fluid motion, like in conventional particle image velocimetry (Adrian and Westerweel, 2011). In some of the current results, the fluctuations maintain a consistent shape throughout consecutive frames, indicating that their timescale of mixing exceeds the interval between consecutive recordings. Therefore, their motion can be distinguished. The axial evolution of the fluctuations is shown in figure 5.5. Here, the shadowgrams shown in the lefmost columns of figures 5.2 and 5.3 are considered, in which the CO_2 is neutrally buoyant. In figure 5.5, the parameter b describes the achieved image width for the current frame rates. The optical signal of the shadowgraphy is shown over time at the red horizontal line of the snapshot that is indicated in figure 5.5a. The resulting space-time graphs show the passage of thermal structures in the form of angled streaks of constant brightness. The nominal angle of the streaks in the space-time graphs is indicated by green dashed
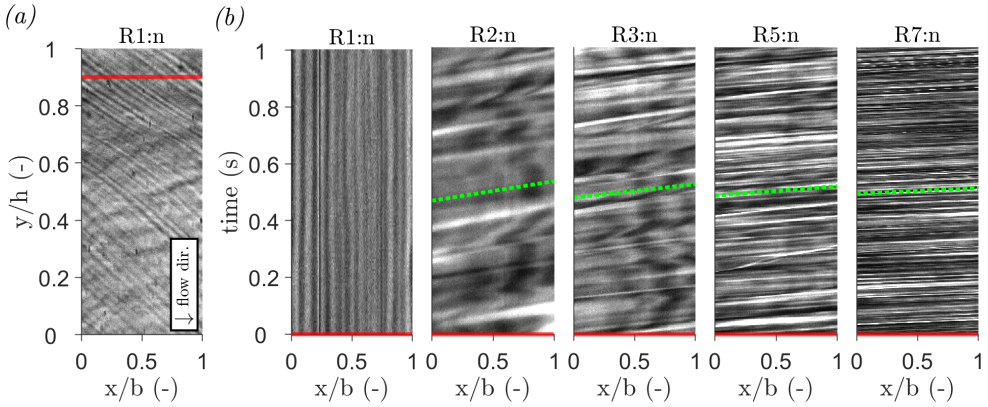
Figure 5.5: Space-time (b) representation of the optical signal at the horizontal line that is indicated in the instantaneous shadowgram shown in (a). The value of Dh is progressively increased by increasing the mass flow rate for the cases shown in (b).

lines for each case. Given that no structures are perceived over time along the red curve for case R1:n, a nominal angle cannot be inferred from the graph. As the imposed Reynolds number is increased for the other cases, the observed structures pass the red line in a shorter time span, and the angle of the streaks with the horizontal axis decreases. Evidently, a velocity-like quantity can be deducted from the streak angles of passing thermal structures in the current representation.

In order to determine whether the movement of the image brightness fluctuations corresponds to the movement of the fluid, the correlated velocity of the fluctuations U_C is measured and subsequently compared to the the velocity imposed by the natural circulation loop U_{imp}. In order to measure U_C, consecutive shadowgrams are correlated to yield the instantaneous displacements of the distinctly shaped image brightness fluctuations in all directions perpendicular to the optical axis. Here, the total image height is assumed to correspond to h. Furthermore, the averaged image is assumed to correspond linearly to the object plane when the CO_2 remains unheated. As such, the means of image-plane displacements Δx and Δy can be divided by the optical magnification M to yield the physical displacements within the test section. Therewith, U_C can be approximated using

$$U_C = \frac{\Delta x}{M \Delta t},$$
(5.4)

where Δt is equal to the period between consecutive frames. However, when the carbon dioxide is heated, the averaged image deforms as a result of large local gradients in refractive index. Therefore, the imaged displacements no longer linearly correspond
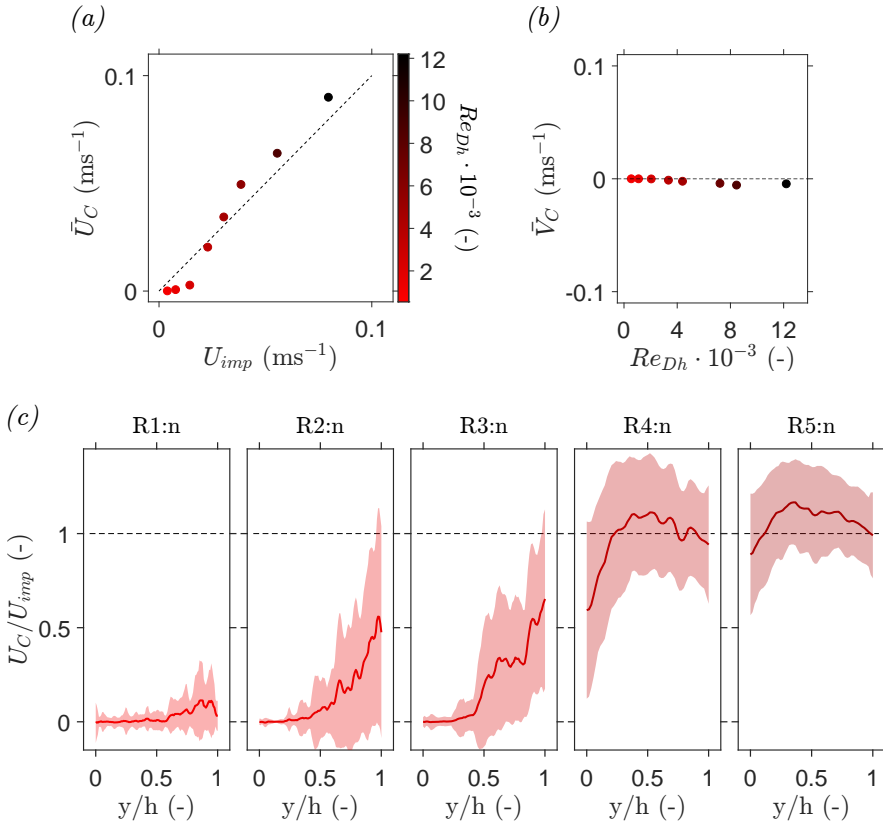
Figure 5.6: Comparison of the correlated velocity with the imposed velocity. Subfigure (a) shows the correlated mean velocity $\bar{U}_C$ with respect to the measured velocity. Subfigure (b) shows the mean value of the vertical component $\bar{V}_C$. A comparison of several instantaneous profiles of U_C with the measured bulk velocity is shown in (c). The data in (a) and (b) are shown with errorbars of $\pm 2\sigma/\sqrt{N}$, where N is the number of frame pairs. The data in (c) contains errorbars of $\pm\sigma$.

to the physical displacements as M is no longer constant throughout the image, and an accurate average value of U_C can no longer be directly deduced. As such, only image-plane displacements are reported for the cases with heating.

The correlated velocity of the refractive structures corresponds conditionally to the imposed velocity of the system. Figure 5.6 shows a comparison of the correlated velocities of the structures in the shadowgrams with the velocities of the natural circulation for unheated flows. In Figure 5.6a, the correlated mean x-direction velocity U_C (deducted from 2999 frame pairs) is compared to U_{imp}. The magnitude of the
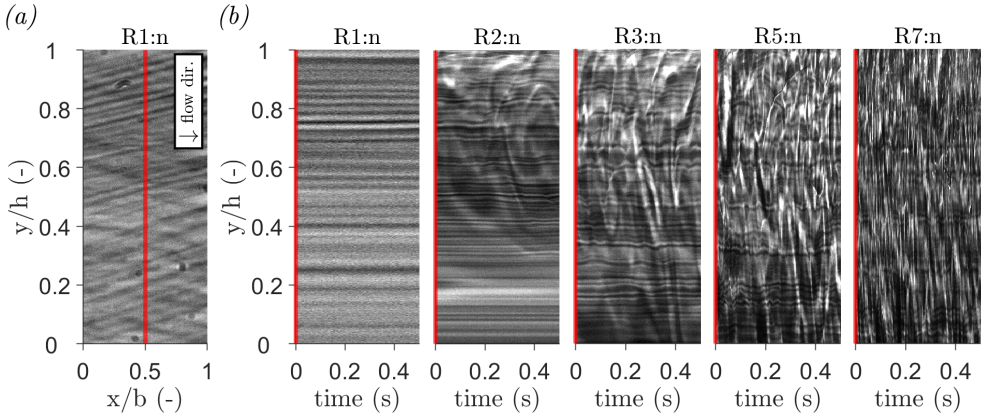
Figure 5.7: Space-time (b) representation of the optical signal at the vertical line that is indicated in the instantaneous shadowgrams shown in (a). The value of $_{Dh}$ is progressively increased by increasing the mass flow rate for the cases shown in (b).

mean reconstructed velocity $\bar{U}_C$ corresponds to the actual bulk velocity U_{imp} for sufficiently large Reynolds numbers, i.e. $Re_{Dh} \geq 3 \times 10^3$.

As shown in the two rightmost plots of figure 5.6c, a mean velocity profile of U_C is reconstructed in which the center-line velocity exceeds the correlated velocity near the channel walls. Furthermore, as expected for a hydrodynamically developed flow, the center-line velocity exceeds the bulk velocity of the channel. As such, the imaged structures are assumed to travel at the local velocity of the flow. Hence, the fluctuations in image brightness can serve as 'pseudo-tracers' of the flow field when it is turbulent for the current thermodynamic conditions. However, the integrating property of shadowgraphy makes that variations of refractive index at any lateral location in the channel are imaged. As a result, the resulting instantaneous displacement fields do not directly correspond to instantaneous, planar flow fields. Instead, the movement of all refractive structures throughout the channel is superimposed. Therefore, as the streamwise velocity of the pseudo-tracers varies laterally, their image velocimetry is characterized by relatively large fluctuations.

At low velocities the structures may decorrelate, yielding no contribution to the displacement correlation, and therewith biasing the result to lower displacements. Figure 5.6c shows this under-reconstruction of the bulk velocity in detail. In the figure, a range of reconstructed mean profiles of U_C is presented, normalized with U_{imp}. NCL velocity U_{imp} is increasingly under-captured for $Re_{Dh} \leq 3 \times 10^3$, most notably so near the bottom channel surface. Figure 5.7 elucidates the cause of this inadequate characterization of the channel bulk velocity. Here, figure 5.7b shows the

optical data captured over time along the vertical red line in figure 5.7a. In the figure, strong fluctuations in image brightness are shown throughout the channel for large Reynolds number cases R5:n and R7:n, indicative of the passage of pseudo-tracers. As the Reynolds number is decreased, the flow becomes more sparsely 'seeded.' Initially, for R3:n and R2:n, fluctuations of the optical signal only persist in the region confined to the upper wall. In these cases the channel flow is likely thermally stratified, in which a separate layer that is lighter and more turbulent is formed on top of a denser, laminar layer. In figure 5.7b, the latter is characterized by an optical signal that is predominantly constant in brightness over time. Whereas this quiescent region is confined to the bottom wall for cases R3:n and R2:n, it spans the full channel height for case R1:n. As such, the channel flow in case R1:n is assumed to be entirely laminar. As the laminar layer is largely homogeneous in density, its shadowgraphy will not portray the passage of thermal structures. As a result, the correlation of consecutive images underestimates the actual motion of the fluid. Therefore, only where sufficient turbulent mixing is present in cases R2:n and R3:n, near the top boundary of the channel, a velocity in the order of magnitude of U_C is captured in figure 5.6c. As the flow is sufficiently mixed such that no stratified layers appear throughout the channel for cases R4:n and beyond, a more appropriate mean flow field is captured throughout the channel.

Lastly, the characterization of the mean flow field shows a moderately negative mean y-direction velocity $\bar{V}_C$ for the larger values of Re_{Dh} within the considered range. Here, the downward motion of sporadic cold plumes within the channel is captured by the image velocimetry. The downdraughts, likely caused by the slight cooling of the CO_2 by the ambient in the vicinity of the visors, have previously been discussed.

The visualisation of the flow field using thermal turbulence as tracers has revealed a mean streamwise flow field characterized by features similar to those of hydrody-namically developed flows with subcritical fluids. However, the large uncertainty of the current method, and its inability to reconstruct a flow field when the flow is in a thermally homogeneous laminar flow state makes its applicability limited. As such, the complete characterisation of instantaneous, planar flow fields at supercritical and thermally heterogeneous conditions requires additional and yet to be developed ex-perimental techniques. Nevertheless, the shadowgrams and the velocimetry thereof can reveal instantaneous fluid motion and flow patterns (or the lack thereof) across the channel at high spatial and temporal frequencies when there is sufficient turbu-lent mixing in the property-variant working fluid. As such, shadowgrams reveal the transient, local phenomena underlying the greatly atypical heat transfer correlations reported in open experimental literature. Therefore, shadowgraphy is used to study the modulation of the channel flow by thermal stratification from here onwards.
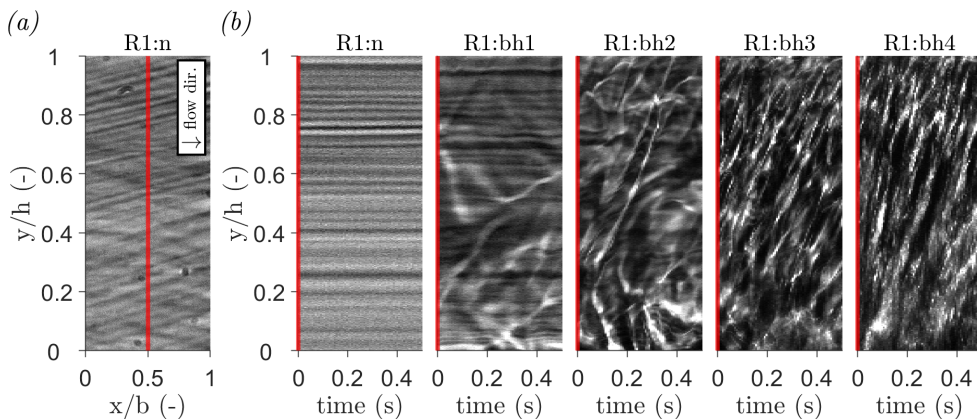
5

Figure 5.8: Space-time (b) representation of the optical signal at the vertical line that is indicated in the instantaneous shadowgram shown in (a). The bottom-up heating rate is progressively increased for the consecutive cases shown in (b).

5.4.2   Unstable stratification

When the rectangular channel is heated in the bottom-upward configuration, the perceived flow field within it is characterized by increased, mostly vertical movement. Currently, the cases shown in figure 5.2 are considered. Figure 5.8 shows the evolution of the shadowgraphy signal of the vertical red line indicated in figure 5.8a in figure 5.8b. Here, the initially quiescent flow of case R1:n is disturbed by movement induced by the unstably stratified CO_2, and images of fluctuating brightness follow. Initially, for R1:bh1, the upward motion in the shadowgrams is predominantly confined to the near-wall region at the bottom of the channel. As warm, lighter plumes rise towards the top of the channel when buoyancy is moderate, they are advected by the bulk flow in the streamwise direction. For this process, the angle of a streak of constant brightness with respect to the vertical axis increases over time in a space-time graph. The process of plume advection by the mean flow is more clearly shown in figure 5.9. Here, the channel is imaged in the period after which the heating state is instantaneously changed from R1:n to R1:bh5. For R1:bh5, a heat flux of $\dot{q} = 12.0 \, \mathrm{kWm}^{-2}$ is applied. Mushroom-like plumes arise from the bottom of the channel in figures 5.9a and 5.9b, as part of a wide, turbulent front. The plumes at the top of the front are overturned in the streamwise direction of the flow as they near the top of the domain in figures 5.9d-f. As such, they form rollers that are ordered one after another in the streamwise direction of the flow, similar to those simulated by Garai et al. (2014) and Pirozzoli et al. (2017) for mixed unstable convection in ideal

$t_0 + 1.401$ s $t_0 + 1.568$ s $t_0 + 1.717$ s $t_0 + 1.771$ s $t_0 + 1.858$ s $t_0 + 1.931$ s $t_0 + 2.903$ s
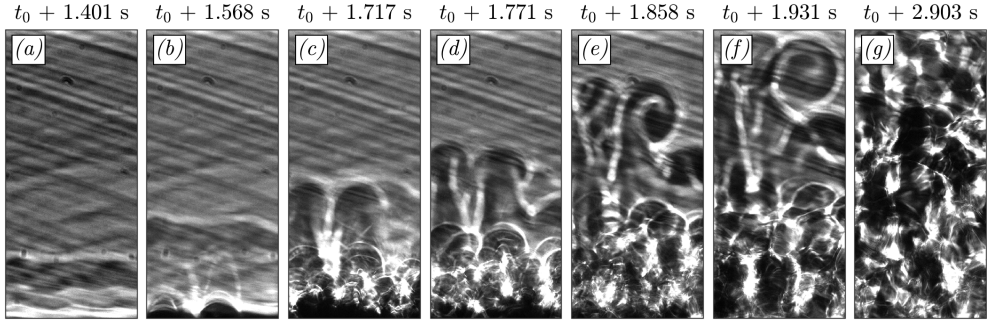
Figure 5.9: Series of shadowgrams that show the evolution of the flow after an instantaneous step in bottom-upwards heating from case R1:n to R1:bh5. For R1:bh5, a heat flux of $\dot{q} = 12.0$ kWm^{-2} is applied. At time t_0, the heating is commenced.

fluids. For the conditions in case R1:bh1, the rollers are exclusively confined to the bottom two-thirds of the channel.

As the heating rate is increased from R1:bh1 to R1:bh2, the thermal structures originating from the heated bottom wall sporadically reach the top surface of the channel. The movement of these updrafts is characterized by straight lines of constant brightness at an angle with the vertical axis in figure 5.8b. As the heating rate is further increased for cases R1:bh3 and R1:bh4, the relative amount of plumes that traverse the channel in its entirety increases, and the image is eventually dominated entirely by the presence of these upward moving structures. Whereas shadowgraphy yields images of mostly constant brightness (see figure 5.8a) when no heating is applied, instantaneous shadowgrams show a chaotic superposition of many plumes for cases R1:bh3 and R1:bh4, as shown in figure 5.9f. In this buoyancy-dominated limit, the natural convection dominates the shadowgraphy, and the natural flow rates far exceeds the forced convection. Instead, the flow much resembles purely natural convection.

Figure 5.10 shows the reconstruction of the x-component of the velocity for cases R1 - R3 for a selection of heating rates. As explained in appendix 5.B, the flow field is reconstructed more accurately as the plumes act as traceable structures in the shadowgrams at moderate heating rates, e.g. bh1 and bh2. Conversely, in the limit of dominant natural convection at bh3 and beyond in the current experiments, the uncertainty in deducing image pair displacements increases due to the rapid decorrelation of the superimposed thermal structures. Initially, a near-zero magnitude flow velocity is reconstructed for a large fraction of the channel for neutrally buoyant case n in figure 5.10a. Here, the mean downstream flow imposed by the natural circulation loop is not captured by the shadow image velocimetry as it lacks contrast
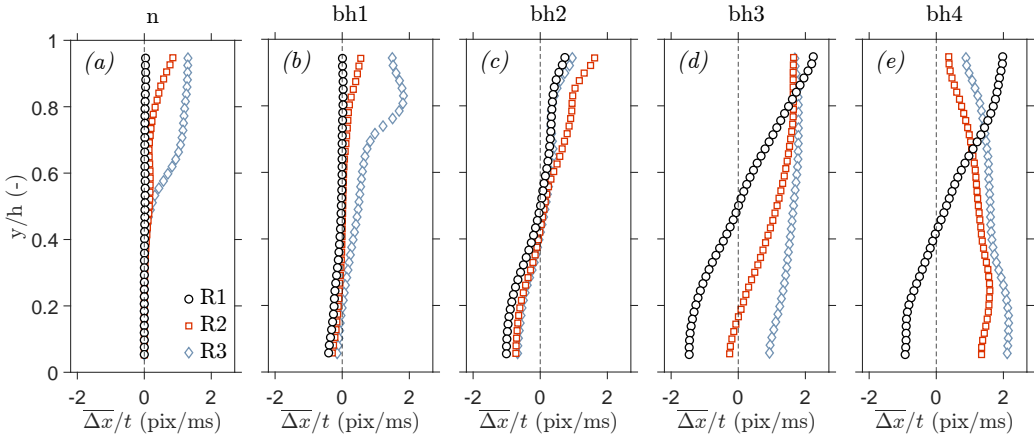
Figure 5.10: Mean perceived horizontal displacement rates $\overline{\Delta x}/t$ for cases R1 - R3, with progressively increased bottom-up heating rates in the consecutive subfigures.

due to the absence of any fluctuations in intensity. As heating is applied the bottom surface, the channel flow is characterized by increasingly strong secondary flows. At first, for case bh1, moderate counter flow can be observed near the heated bottom surface. Eventually, for cases bh2 and beyond, a positive flow rate in the downstream direction is perceived near the opposite wall. Here, thermal plumes that reach the top of the channel act effectively as tracers of fluid motion, yielding a non-zero displacement field throughout the domain. As can be seen in figures 5.10c-e, the two near-wall regions show velocities of opposite signs. Here, the significant dilation of the carbon dioxide has led to the formation of a cell in which the fluid recirculates continuously, with a cell width much larger than the current field of view.

In the unstably stratified configuration, the velocity of the upward plumes depends on the applied heating rate. The mean displacement rates of the plume motion is shown in figure 5.11. For cases bh1 and bh2, moderate and positive non-zero motion is only observed in the vicinity of the heated wall, in which plumes are perceived in the shadowgrams. The vertical velocity of the plumes increases as the heating rate is increased from bh1 to bh2. As the heating rate is further incremented to case bh3, finite upward motion is seen throughout the channel. Here, the thermal plumes traverse the test section channel at a larger velocity than for cases bh1 and bh2. As the amount of plumes that is produced increases further, the uncertainty in the deduction of their mean velocity also increases. Eventually, for case bh4, the upward displacement rates of a similar magnitude as the maximum x-direction displacement rates for R1 and R2, as can be deduced from a comparison between figures 5.10e
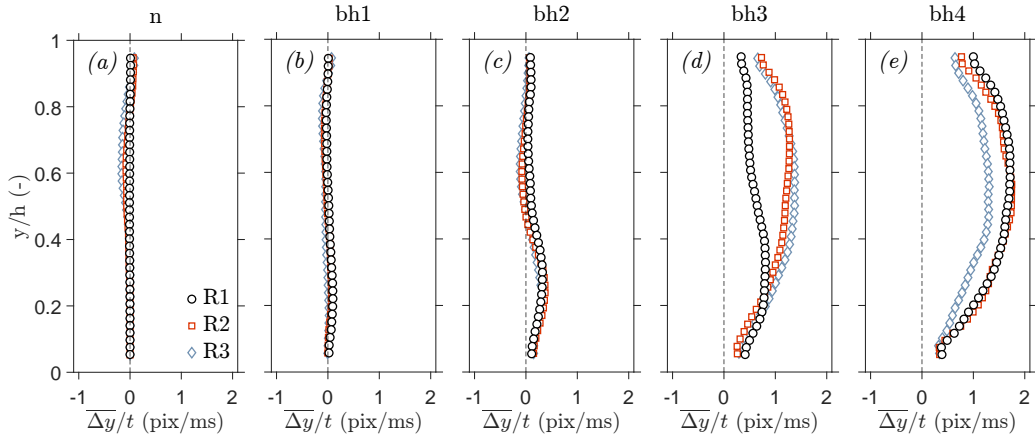
Figure 5.11: Mean perceived vertical displacements $\overline{\Delta y}/t$ for cases R1 - R3, with progressively increased bottom-up heating rates in the consecutive subfigures.

and 5.11e. Importantly, the results of figure 5.11 do not necessarily imply that a net upward flow is present in the channel. Instead, figure 5.11 shows the motion of refractive structures somewhere within the channel.

5.4.3 Stable stratification

5.4.3.1 Turbulence attenuation

A process in which fluctuations and vertical movement are diminished follows from the top-down heating of the highly property-variant fluid for the cases in figure 5.3. Therewith, the flow of carbon dioxide is modulated in a distinctly dissimilar manner than for bottom-up heating. The sharp contrast between the response of flows subject to either stratification type can be highlighted by considering several points at different vertical positions within the channel. Figure 5.12 shows the normalized shadowgram intensity of the points over time. Initially, cases R2:n and R5:n are considered in figures 5.12a and 5.12b, respectively. Here, the fluid in the channel remains unheated. Whereas the variability in the signal of case R2:n is larger in its lighter top-layer than in its denser bulk, its brightness (and therefore its density) is relatively homogeneous in time. After 9.3 seconds, a heating rate $\dot{q}$ with a magnitude of 12.0 kWm^{-2} is applied to the channel surface in the bottom-upwards configuration in figure 5.12a. Some time after the heating has started, the unstably stratified density interface that is formed near the heated wall breaks down. A plume-laden front rises to the top of the channel follows, as is shown in figure 5.9. Eventually, the signal is saturated
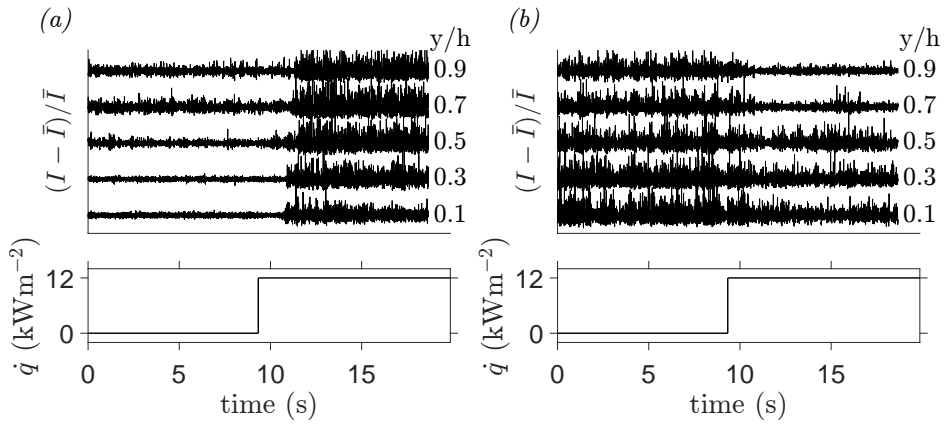
Figure 5.12: Image brightness I over time. In subfigure (a) the carbon dioxide is heated from the bottom upwards from an initial state R2:n. In subfigure (b) the carbon dioxide is heated from the top downwards from an initial state R5:n.
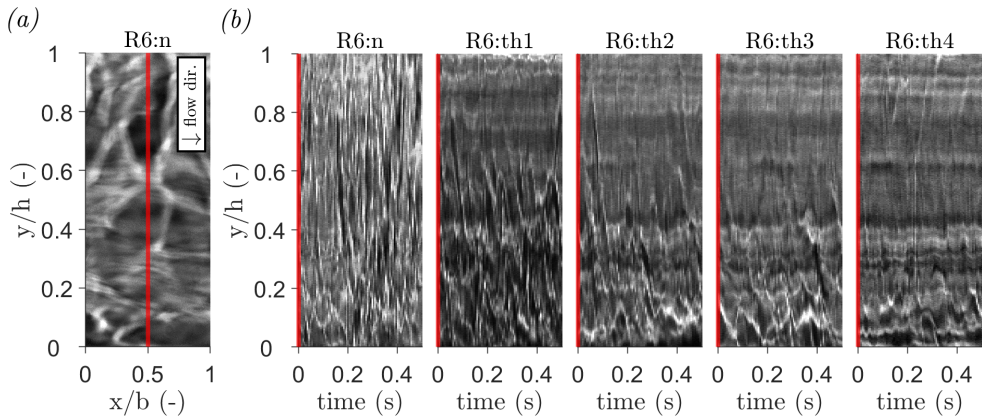

Figure 5.13: Space-time (b) representation of the optical signal at the vertical line that is indicated in the instantaneous shadowgram shown in (a). The top-down heating rate is progressively increased for the consecutive cases shown in (b).

with frequent passages of rising plumes, evidenced by a large variability in image brightness over time.

Shadowgrams of case R5:n, in which a larger mass flow rate is applied through the test section, are characterized by the intermittent passage of shadowgraph structures in an unheated setting. As the passage of refractive structures corresponds with consecutive maxima and minima in image brightness, the variability of the signal far exceeds that
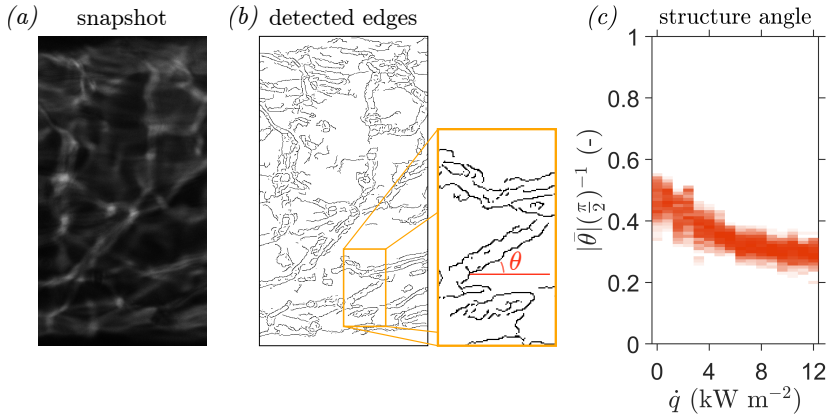
Figure 5.14: Thermal structure orientation as a function of the applied top-down heating rate. The edges (b) within any instantaneous shadowgraph (a) are detected as per Lefauve and Couchman (2024), and their local angle θ with the x-axis is evaluated. In (c), the mean absolute angles $|\bar{\theta}|$ of 300 snapshots are superimposed for each increment in $\dot{q}$ for case R7.

of case R2:n. Similarly, a heating rate $\dot{q}$ with a magnitude of 12.0 kWm^{-2} is applied to the channel surface in the top-down configuration after 9.3 seconds. Consequently, the variation in shadowgraphy signal in the region near the heated wall decreases significantly. Here, a region that is mostly homogeneous in brightness (and hence density) is formed. The layer is characterized by a near-complete suppression of fluctuations, with the occasional passage of a single refractive streak at moderate heating rates. Given its apparent homogeneity in density in both space and time, the flow of CO_2 within the homogeneous layer is considered to have relaminarized. The emergence of a homogeneous layer can also be observed in figure 5.13b, in which the signal along the red, vertical line in figure 5.13a is shown over time. Here, the top-down heating rate is incrementally increased from R6:n to R6:th4. As the heating rate is increased, the non-fluctuating region expands away from the heated wall to cover a greater fraction of the channel height. As can be deduced from figure 5.3, the thickness of the layer furthermore depends on the imposed Reynolds number. There, the homogeneous layer becomes more limited in size as the Reynolds number is increased.

When the top surface of the flow is heated, the shape of the refractive structures in the shadowgrams changes. The orientation of the structures in the channel flow under unstable stratification for the cases shown in figure 5.3 is considered in figure 5.14. The boundaries of the refractive structures for the instantaneous shadowgram shown
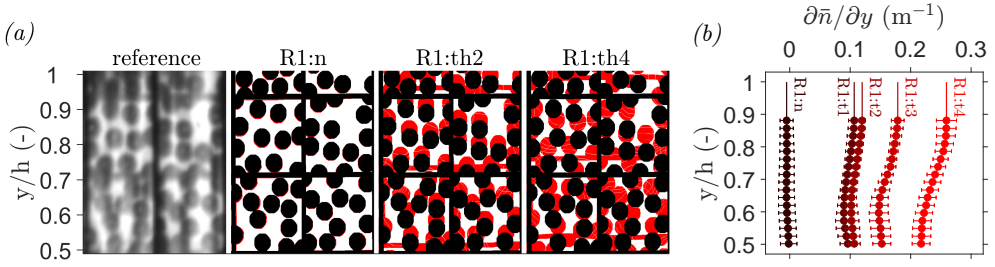
Figure 5.15: The displaced state of an in-focus pattern that is imaged through carbon dioxide at supercritical pressure is shown for various top-down heating rates for case R1 in (a). The original pattern is shown in black. The mean, interpolated local displacement for each point is used to shift the black pattern, yielding the pattern shown in red. Profiles of the path-integrated vertical gradients in refractive index are shown in (b). The data in (b) is shown with errorbars of $\pm 2\sigma$.

in figure 5.14a are presented in figure 5.14b. An edge detection algorithm, similar to the one described by Lefauve and Couchman (2024), is used to detect the structure boundaries in the shadowgrams. Thereafter, the angle of all edges with the x-axis $\theta(x, y)$ is evaluated. The normalized value of $\bar{\theta}$, averaged over 300 images, is presented in figure 5.14c. When unheated, the flow contains structures of any shape and orientation, exhibiting gradients in density in any direction. Then, the value of $\bar{\theta}$ approaches $\pi/2$. After heating is applied, the imaged streaks are found to re-orient within the channel. Structures that represent a constant density that initially span a finite vertical height, are increasingly stretched in the streamwise direction. As a result, $\bar{\theta}$ reduces. As such, the fraction of the height of a channel spanned by a structure of constant density decreases. In the near-wall layer, vertically oriented streaks disappear altogether, revealing an axially homogeneous density field. Here, the originally irregular density field is assumed to be redistributed in the channel as the flow is heated.

Figure 5.15 reveals that the initial density field is redistributed along a mean density gradient, imposed by the top-down heating. For the purpose of highlighting such mean gradients in refractive index, the BOS configuration indicated in cross section **B** of figure 2.3 is considered. In figure 5.15, the deformation of a background pattern by the refractive CO_2 is considered. Only under stable stratification do the fluctuations in the optical signal attenuate sufficiently to get a clear BOS image. The considered reference pattern, shown in black in figure 5.15a, is printed onto a transparent sheet and placed behind the CO_2. As the carbon dioxide is heated, the pattern's image deforms. The deformed images for cases R1:n, R1:th2 and R1:th4 are shown in red in figure 5.15a.
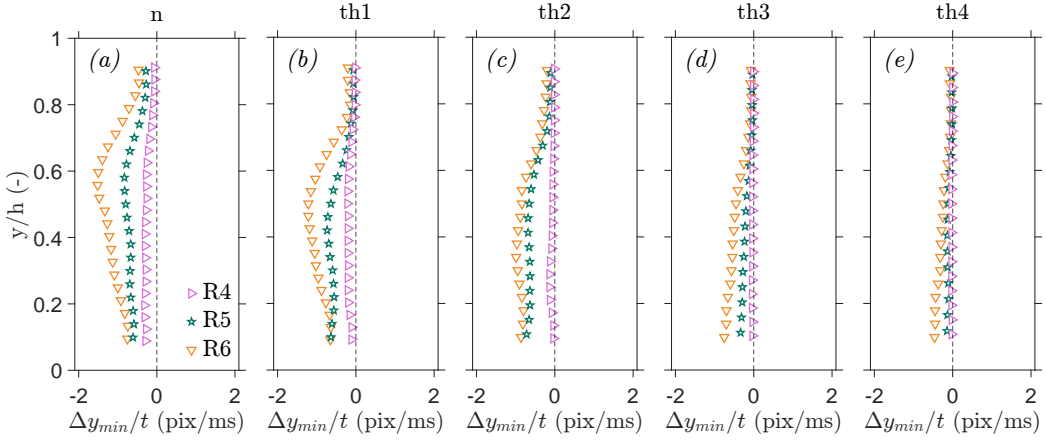
Figure 5.16: Maximum instantaneous vertical displacements in the negative y-direction for cases R4 - R6, with progressively increased top-down heating rates in the consecutive subfigures.

Here, the black pattern is shifted with the correlated deformation displacements at any point, yielding the deformed pattern shown in red. In neutrally buoyant case R1:n, the imaged pattern remains in a predominantly undeformed state. As heating is applied to the top of the channel in cases R1:th2 and R1:th4, the dot pattern in the top half of the channel is stretched by variations in the refractive index. Here, the background pattern is deformed to a greater extent when the applied heating rate is increased. Figure 5.15b shows the vertical gradients in path-integrated refractive index that are deducted from the dot pattern displacements. Here, $n_0 = 1.17$, $M = 0.5$, and $Z_D = 8.9 \cdot 10^{-2}$ m. The magnitude of the refractive index gradients are found to increase as greater heating rates are applied to the channel flow. Furthermore, the gradients are the largest in the near-wall region for all considered cases. The presence of a strong vertical gradient in $\bar{n}$ suggests the existence of an equivalent gradient in CO_2 density $\bar{\rho}$ in the current top-down heated configuration. Given the positive values of $\partial \bar{n}/\partial y$ in figure 5.15b, the density of the carbon dioxide increases away from the heated wall. The imposed vertical gradient in $\bar{\rho}$ imposes a buoyant force on the fluid in the channel. As discussed by García-Villalba and Del Alamo (2011), fluid parcels of a certain density are pushed towards a preferential vertical position along the constant gradient. If the buoyant force exceeds the inertial forces of a fluid parcel, its vertical movement is diminished once it is at its preferential position. This is true for an increasingly large density range and for an increasingly large portion of the channel as the imposed density gradient becomes sharper when the heating rate

is increased. As a result, vertical motion is increasingly diminished in the near-wall region when heating is applied, as also shown in figure 5.16. In the figure, the largest instantaneous downward shadow displacements within the considered measurement interval are shown for cases R4 - R6. Initially, for unheated case n, the flow is characterized by the sporadic vertical movement of eddies with a variable density. As moderate heating is applied for th1 and th2, vertical motion in the near-wall region is suppressed along the vertical density gradient. The region within which the vertical motion of turbulent eddies is suppressed grows as the heating rate is increased towards case th3. Eventually, most vertical motion is suppressed in case th4. The suppression of vertical motion is supported by the vertical thinning of the averaged correlation profiles, as shown in figure 5.21 of appendix 5.B.

5.4.3.2   Implications on PIV

The large deformation of the background pattern reveals limitations to the further characterization of the flow at a near-pseudo-critical state beyond the spatial resolution that the current thermal tracers allow for. In particular, the large image distortions affect the applicability of Particle Image Velocimetry (PIV), where a correlation of the displacements of tracer particles is used to re-construct a flow field. The images of carbon dioxide at the current near-pseudo-critical conditions are characterized by large deformations both when the CO_2 is heated locally, and when refractive structures that correlate with the fluid motion are present in an unheated turbulent flow. Furthermore, the gradients of these deformations can be particularly large for heated turbulent flows, leading to image blur. Additionally, total internal reflections across stratified layers can lead to the local compression of the object in the image plane, obscuring its features. As a result, the apparent displacements of the particles may not correspond to their actual displacements. This is most prevalent as the tracers move across density gradients within the flow. The current back-projected error in determining the particle positions within the channel can be of the order of 100 μm. Therewith, it can exceed the particle diameters of the tracers (Valori et al., 2019; Michelis et al., 2024) that are relatively small to reduce slip velocities with the property-variant working fluid. As such, PIV systems may prove to be particularly difficult to calibrate when a flow displays large local variations in thermodynamic properties.

5.4.4   Overall heat transfer

5.4.4.1   Thermal response data

Measurements of the surface temperature of the heated walls serve to provide a quantitative context to the optical results presented in this work. Figure 5.17a shows the
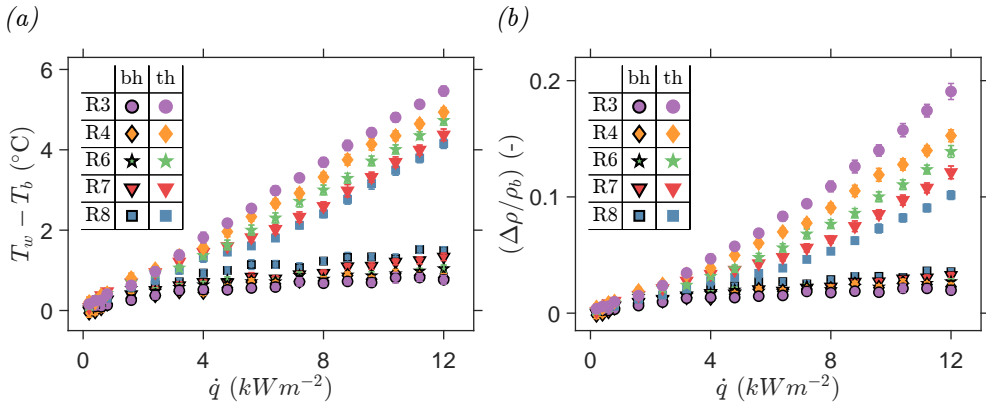
(a)   *(b)*

Figure 5.17: Wall temperature (a) and deducted wall density data (b) for a selection of cases with different nominal Reynolds numbers from figures 5.2 and 5.3. Bottom-up (bh) heating data points are shown with black-outlined markers, whereas top-down (th) heating data points are shown with homogenous markers. The data is shown with errorbars of $\pm 2\sigma$.

mean increase in heater temperature T_w with respect to the constant bulk temperature T_b for a selection of cases of either configuration. When the CO_2 is unstably stratified, the increase in surface temperature remains within $1.5°C$ for the shown parameter range. Furthermore, the measured step in wall temperature decreases as the imposed heat flux is increased. Therefore, the heat transfer rate is expected to progressively improve as greater heating rates are imposed. Initially, a qualitatively similar trend is observed when the top surface of the channel is heated. However, beyond a threshold heat flux, a near-linear increase in wall temperatures (indicative of a predominantly constant heat transfer coefficient) is found for increasing heating rates. This threshold heat flux decreases with decreasing Reynolds numbers. Beyond $\dot{q} = 4 \text{ kWm}^{-2}$, the near-wall temperatures of the two heating configurations start to significantly differ for any of the considered Reynolds numbers. Eventually, for the largest heating rate considered in this work, the increase in surface temperature of the stable stratification exceeds the unstable stratification's temperature increase by twofold. As such, heat is removed much more effectively from the heated wall in the unstably stratified setting than it is in a stably stratified configuration for the current experimental conditions of supercritical pressure CO_2.

Figure 5.17b shows the relative expansion of the carbon dioxide in the vicinity of the heated wall, as deducted from the wall temperature data of figure 5.17a. In accordance with the wall temperature data, the heating-induced density change is

significantly larger for stable stratification than it is for unstable stratification. As
such, the degree of stratification (expressed by the Richardson number) is greater
when the stratification is stable than when it is unstable under equivalent heating,
as previously noted in figure 5.4. The relative difference in dilation even exceeds
the relative difference in surface temperature increase, as can be deduced from the
increasingly superlinear trend in density variation during stable stratification. Here,
the carbon dioxide exhibits increasingly large variations in density as it is heated
towards the non-linear pseudo-critical curve from the liquid-like test section inlet
conditions.

5.4.4.2   Characterization of heat transfer

The analysis of the current experimental heat transfer data reveals trends that are
in qualitative agreement with findings from open literature, and with the optical
data presented in this work. When sub-pseudo-critical CO_2 is heated, its heat transfer
changes through changes in the near-wall heat capacity, viscosity, thermal conduction,
and density (Hall et al., 1967; Yoo, 2013). To understand the current experimental
results, we first focus on the influence of variations in the former three thermophys-
ical properties, which dominate when buoyancy effects are negligible at moderate
heating rates in forced convection (Jackson, 1979). As the fluid is heated towards
the pseudo-critical curve at a set bulk Reynolds number, its near-wall viscosity and
thermal conductivity decrease. These reductions lead to a decrease in the skin fric-
tion coefficient and wall-normal conduction, worsening the convective heat transfer
(Nemati et al., 2015). However, this effect is overshadowed (Jackson, 1979; Licht
et al., 2008; Nemati et al., 2015) by the stronger increase in near-wall heat capacity,
c_p, as is illustrated in figure 1.3, resulting in an overall enhancement of heat transfer
(Yamagata et al., 1972; Jackson, 1979; Licht et al., 2008). The rise in near-wall
heat capacity limits the temperature increase of the near-wall CO_2 at a constant heat
flux, reducing the temperature difference between the bulk and the near-wall region
(Licht et al., 2008). Consequently, the apparent convective heat transfer coefficient
and the Nusselt number increase (Jackson, 1979; Licht et al., 2008). The heat transfer
of the initially liquid-like carbon dioxide continues to improve until the near-wall
temperature reaches the pseudo-critical curve, where c_p peaks.
Variations in near-wall density affect the behavior of fluids at supercritical pressures
in two distinct ways. The strong expansion of the fluid upon heating can accelerate
the near-wall flow, depending on both the direction of the fluid flow and the direction
of the heat transfer (Nemati et al., 2015; Wahl et al., 2022). This modulation of
shear rates increases skin friction, thereby enhancing the overall heat transfer rate. In
the current experiment, such acceleration is expected only in the top-down heating

5

configuration. There, stable stratification counteracts the vertical transport of the lighter, hotter fluid throughout the channel, accelerating the near-wall layer of fluid at the top (Jackson, 2013; Chu and Laurien, 2016). However, limitations of the current 'shadow velocimetry' prevent reliable measurements of this acceleration when the homogeneous layer forms under stable stratification. Therefore, the remainder of the present discussion on the measured heat transfer instead only considers the consequences of the modulation of the flow by buoyancy when sufficiently large variation in density is induced (Jackson, 2013). These buoyant effects either aid or oppose the heat transfer enhancement by the increasing magnitude of c_p, depending on the heat transfer configuration.

To highlight the influence of buoyancy on the measured heat transfer, the mean Nusselt number Nu_w is shown as a function of the Richardson number Ri in figure 5.18, for a selection of cases of either configuration. There,

$$Nu_w = \alpha \cdot \frac{h}{\lambda_w} = \frac{\dot{q}}{T_w - T_b} \cdot \frac{h}{\lambda_w}, \tag{5.5}$$

with α as the convective heat transfer coefficient, evaluated in experiment using the imposed heat flux $\dot{q}$ and the temperature difference over the channel. Moreover, λ_w is the near-wall thermal conductivity, evaluated at T_w and P_{02}. When buoyancy is non-dominant, at $Ri \lesssim 0.1$, the empirical heat transfer coefficients of the two considered heat transfer orientations are of a similar magnitude. However, as buoyancy becomes non-negligible for larger heating rates, the values for Nu_w diverge.

When the carbon dioxide is heated from the bottom upwards at the current thermodynamic conditions, both buoyancy effects and an increase in specific heat act to enhance its heat transfer, increasing Nu_w with respect to its neutrally buoyant value. The shadowgrams of unstably stratified CO_2 (shown in figure 5.2) are characterized by the strong secondary flows that are elaborated on in figures 5.8-5.11. In the limit of small Reynolds numbers, plume motion is observed to form recirculation cells that locally counteract the imposed forced convection. For any Re_{Dh}, the expansion of CO_2 causes motion in the wall-normal direction, in which parcels of lighter fluid are locally lifted towards the denser bulk flow. Here, hotter fluid is continuously carried away from the heated wall, replacing it with a denser and colder fluid that is recirculated. Therewith, the mean near-wall fluid temperature decreases with respect to an equivalent neutrally buoyant setting, leading to the sub-linear increase of $(T_w - T_b)$ in figure 5.17a. Furthermore, the vertical plume motion increases the wall-normal momentum transport in the channel. Consequently, the vertical energy transport also increases with respect to purely forced convection, as characterized by the enhancement of Nu_w in figure 5.18. However, this effect diminishes as the relative inertial contributions increase. Therefore, Nu_w decreases with increasing Re_{Dh} at a set heat-
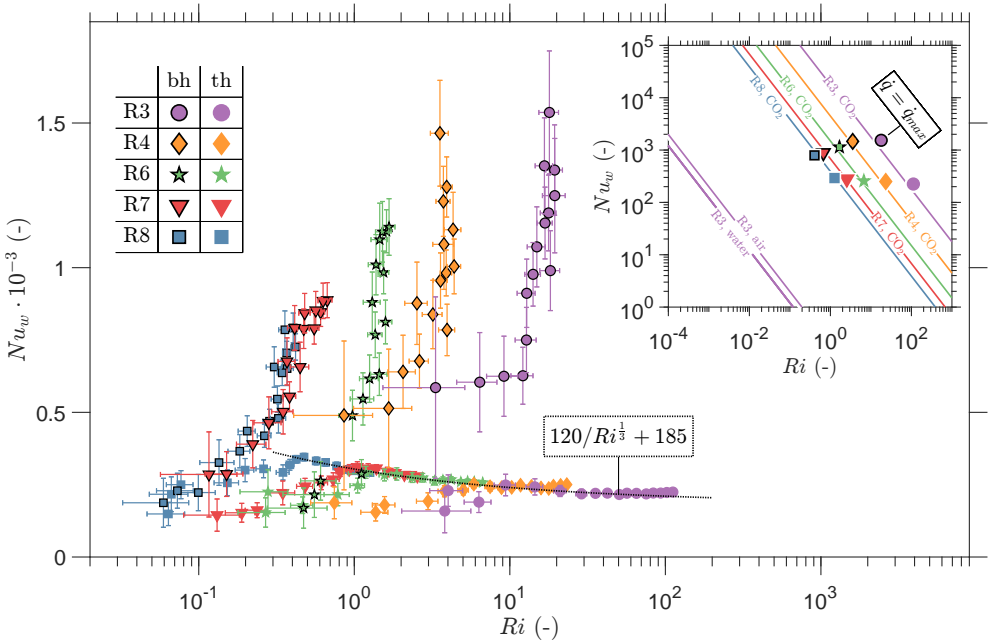
Figure 5.18: Nusselt number (main figure) and comparison with equivalent scenario with subcritical air and water (top right corner) for a selection of cases from figures 5.2 and 5.3, as a function of the deducted value for Ri. Bottom-up (bh) heating data points are shown with black-outlined markers, whereas top-down (th) heating data points are shown with homogenous markers. The data is shown with error bars of $\pm 2\sigma$.

ing rate. Contrary to a previous empirical investigation of purely bottom-upwards heated micro-channels of CO_2 with $Ri \lessgtr 1$ by Whitaker et al. (2024), the relative enhancement of the heat transfer progressively increases as buoyant forces become increasingly dominant at larger Ri within the current parameter range. A progressive improvement of the heat transfer with increasing degrees of unstable stratification is however in accordance with the current optical data. Here, the spatial density of the plumes and their lift velocities are found to both increase at greater heating rates, increasing the vertical momentum transfer in the channel. As such, the progressive enhancement of the heat transfer as buoyancy becomes more dominant with increasing degrees of unstable stratification in figure 5.18 is expected from the increasingly prevalent motion of the thermal plumes.

When the carbon dioxide is heated in the top-down configuration, the buoyancy caused by decreasing near-wall density opposes the heat transfer enhancement induced by the

variation in near-wall heat capacity. At low Ri, the effects of a variable c_p dominate, improving the heat transfer as $\dot{q}$ is increased. Eventually, as buoyancy becomes more dominant for larger Ri, the heat transfer deteriorates, yielding a maximum in Nu_w that resembles the results of Yamagata et al. (1972) and Bae et al. (2010). This deterioration of the heat transfer by buoyancy is supported by the current optical results. In the shadowgrams, the imposed density gradient of figure 5.15 is found to counteract vertical movement as the carbon dioxide is heated at the top surface of the channel, as is elaborated in figures 5.13 and 5.16. The resulting flow is characterized by the suppression of intermittent, irregular motion. Here, the mixing of distinct layers with different densities is counteracted. As such, the lighter fluid that is formed at the heated top wall remains predominantly in the near-wall region. As a result, the overall near-wall temperature increases. Therewith, the wall-normal heat transfer rate deteriorates in comparison with a neutrally buoyant flow, in which the wall-normal movement of warmer eddies removes hot fluid from the heated wall. Notably, at large values of Ri, the values of Nu_w for the current results coincide, as is shown in figure 5.18. Here, Nu_w attains an asymptotic value, irrespective of the imposed Reynolds number. For these conditions, Nu_w can be described using

$$Nu_w = \frac{120}{Ri^{\frac{1}{3}}} + 185, \tag{5.6}$$

as indicated with the black, dashed line in figure 5.18. Contrary to the progressive enhancement of the heat transfer under unstable stratification, Nu_w only moderately decreases as a function of Ri when the heat transfer deteriorates. This moderate dependence on Ri is in qualitative agreement with the shadowgraphy, as the intermittency of the optical signal shows minimal changes upon the initial suppression of fluctuations by the thermal stratifications. Then, only a change in the height of the homogenized layer follows from a further increase in Ri.

To highlight the non-ideality of the current heat transfer, we plot the Nusselt number as a function of the Richardson number in the inset of figure 5.18. There, the Nusselt number is expressed in terms of the Richardson number, which is re-defined as a function of $(T_w - T_b)$ and β_b, with

$$Ri = \frac{\beta_b \, (T_w - T_b) \, gh}{U_{\text{imp}}^2}, \tag{5.7}$$

where β_b is the volumetric expansivity, evaluated at T_{03} and P_{02}. By substituting $(T_w - T_b)$ into a Nusselt number that is evaluated at the bulk conditions, with

$$Nu = \frac{\dot{q}}{(T_w - T_b)} \frac{h}{\lambda_b}, \tag{5.8}$$

Nu can be expressed as a function of Ri, namely

$$Nu = \dot{q} \cdot \frac{\rho_b^2 \beta_b}{\mu_b^2 \lambda_b} \cdot \frac{g h^2 D_h^2}{Re_{Dh}^2} \cdot \frac{1}{Ri}. \tag{5.9}$$

Equation (5.9) enables a comparison of Nu for several fluids at similar operating parameters corresponding to the current experiments. The respective curves in the inset are plotted using the thermophysical properties of air and water at atmospheric conditions (at 20°C) and of CO_2 at the current experimental conditions, all for a heat flux of $\dot{q} = \dot{q}_{max} = 12\,\mathrm{kWm^{-2}}$. The experimental data (indicated using markers in the inset) for both stably and unstably stratification coincide with the curves of Nu for CO_2 at the current conditions. The results reveal a striking contrast: for a heat transfer configuration with a given Nusselt number, the Richardson numbers for CO_2 exceed those of air and water by several orders of magnitude. This confirms that buoyancy effects, which are negligible in typical subcritical single-phase systems, readily dominate heat transfer at supercritical pressures.

The significant non-ideality of the observed heat transfer strongly affects the performance of near-pseudo-critical heat exchangers in energy conversion systems at supercritical pressures. As buoyancy readily dominates at their operating conditions, the resulting heat transfer deviates strongly from equivalent but neutrally buoyant systems. As a result, the direction of the applied heat transfer strongly affects the behaviour within heat exchangers that operate in the vicinity of the pseudo-critical curve. Within the current parameter range, a significant difference between the heat transfer rates of purely top-heated and purely bottom-heated flow of carbon dioxide at supercritical pressure is observed. This difference is most notable for the larger heating rates in this work, for which the bottom-up heat transfer coefficient exceeds the top-down heat transfer coefficient by nearly a full order of magnitude, as shown in figure 5.18. However, in the flow channels of plate heat exchangers or a Printed Circuit Heat Exchangers (PCHEs), heat is generally exchanged in multiple directions. As such, the heat transfer enhancement near the bottom wall and the heat transfer deterioration near the top wall compete when the flow is heated. If the heating rate for both surfaces is equal, much like in the current work, the degree of stratification is greater in the region near the top wall. Therefore, the lower-density layer near the top wall would likely not be fully disrupted by the upward movement of plumes created at the bottom wall. Therewith, the behaviour within the heat exchanger would be qualitatively similar to a pipe flow to which a constant heat flux is applied (Chu and Laurien, 2016). Therefore, the equivalent heat transfer coefficient of the heat exchanger channel is expected to lie between the deteriorated and enhanced values of the one-sided heating configurations that are considered in this work.

5.5   Conclusions

In this work, the modulation of the turbulence and the stability of a continuous flow of a supercritical fluid by non-negligible buoyancy is investigated. Such flows are for instance prevalent in novel energy conversion systems that operate at supercritical pressures, which have gained particular recent interest for their potential to sustainably produce power and industrial heat. Within the heat exchangers of these energy systems in particular, non-negligible buoyancy may lead to highly non-ideal and configuration dependent heat transfer.

The current experimental facility employs the natural circulation of carbon dioxide that is passed through an optically accessible test section. To study the hydrodynamically developed flows of carbon dioxide at supercritical pressures within the test section, shadowgraphy is used in parallel with surface temperature measurements. The shadowgraphy is used to visualize a side-view, path integrated flow field. When the temperature of the CO_2 is sufficiently heterogeneous, thermal structures within the flow can be distinguished in the shadowgrams. As the structures are observed to move with the flow, they are considered to act as thermal flow tracers. As such, a correlation of their displacements yields velocity components in the directions perpendicular to the optical axis. It is validated that the mean streamwise displacements of these pseudo-tracers correspond to the expected mean flow velocity inside the test section, provided that the CO_2 is sufficiently turbulent (i.e. $Re_{\mathrm{Dh}} \gtrsim 3 \cdot 10^3$) and neutrally buoyant. However, the shadow image velocimetry is characterized by relatively large uncertainties, as the method depends on the local occurrence of density fluctuations (leading to variations in refractive index) of the flow, and the finite coherence of these structures in time. Furthermore, additional, rigorous calibration is necessary to translate the shadow displacements to physical velocities when large global refractive index gradients are present in the channel under heating conditions. Nevertheless, the shadowgrams can distinguish flow movement patterns within the channel unique to either stratification type when the CO_2 is heated either from the bottom or from the top of the test section. As such, the shadowgraphy serves to reveal the highly transient behaviour behind the non-ideal, and thermally inert heat transfer results in existing open literature to date.

The rectangular flow channel is heated unidirectionally in either vertical direction to impose a density gradient on the carbon dioxide within it. The CO_2, initially at 88.5 bar and 32.6 °C, is heated towards the pseudo-critical curve. As the carbon dioxide displays sharp variations in thermodynamic properties in the vicinity of this curve, strong stratifications are observed for remarkably moderate heating rates. Achieving a comparable degree of stratification in subcritical single-phase fluids

would require significantly larger length scales and heating rates. Consequently, these strong stratifications lead to the modulation of the initially neutrally buoyant base flow, as is shown in figures 5.2 and 5.3. Depending on the stratification type, the variability in the flow is either enhanced or suppressed.

When the channel is heated from the bottom upwards, the flow is characterized by increasingly strong secondary movement. Here, light plumes are seen to intermittently depart from the heated surface, limiting its increase in temperature. Both the wall-normal velocity and the spatial density of these plumes are found to increase as the applied heating rate is increased. As these effects enhance the energy exchange with the heated wall, they further support the heat transfer enhancement by the increase in near-wall heat capacity of the supercritical working fluid. As a result, the Nusselt number is found to progressively increase with respect to the neutrally buoyant case for all considered Reynolds numbers.

On the contrary, when only the top surface of the flow channel is heated buoyancy acts against the heat transfer enhancement by the varying specific heat capacity. Consequently, the heat transfer deteriorates at large heating rates when buoyancy becomes more significant. This deterioration in heat transfer coincides with the suppression of oscillations in the optical signal by the stable density gradient imposed by the heating. This imposes a restriction in vertical motion and mixing across the density gradient that limits the wall-normal motion of hot CO_2 from the heated surface, therewith reducing its heat transfer coefficient.

The present work emphasizes the necessity for the further investigation of buoyancy modulated turbulence and heat transfer in the near-pseudo-critical region beyond the current experimental conditions. Whereas the current results provide novel empirical insights in strong one-directional stratifications, the interplay of the opposing stratification remains unknown in the context of channel flows. Therefore, in order to properly describe the flow of supercritical carbon dioxide within horizontal heat exchanger channels, two-sided heating should also be considered. Furthermore, the current experimental framework can be extended to study the influence of non-negligible buoyancy in physical configurations beyond the current one. Therewith, vertical flows of highly property-variant fluids, where buoyancy also has a pronounced effect, can also be considered.

By improving the used optical diagnostics, they can serve as references for the improvement of hydrodynamic and heat transfer models. A further increase in the spatial resolution in of the shadow velocimetry in particular can for instance be achieved with the local, *in-situ* generation of thermal tracers. As an additional consequence, the flow can also be visualized when thermal tracers are not naturally present in the supercritical carbon dioxide. Furthermore, by controlling the ambient temperature of

the test section, the current framework could be extended to obtain discernible optical data for a greater thermodynamic range at supercritical pressures.

5.A   Optical filter

The present optical configuration is sensitive to surface imperfections of the visors shown in cross section **B** of figure 2.3. The imperfections cast optical distortions on the shadowgrams. In order to remove the visual noise induced by the surface flaws and to make the actual thermal structures within the channel discernible in the presented figures, a filter is used. As the large variations in refractive index deform the shadowgraphs and hence the striations cast by the imperfections, subtracting the averaged image from an instantaneous one yields noisy images. Nevertheless, the visors cast striations at several near-constant angles. As such, a spatial filter (a top-hat filter applied to the Fourier transforms of all shadowgrams) is tuned to remove a narrow bandwidth of spatial frequencies for a limited range of angles. As such, the filter removes the unwanted striations that can be seen in an averaged shadowgram, whereas structures of other orientations remain unaffected.

The effectiveness of the present filter is assessed in figure 5.19. The figure compares the unfiltered to the filtered optical signal for a range of Reynolds numbers. At the expense of image contrast, the filter removes most imperfections, whilst keeping the shadows caused by variable density mostly intact. The filter is applied to the shadowgrams shown in figures 5.2, 5.3, 5.5a, 5.7a, 5.8a, 5.9, and 5.13a. However, the filter is not applied to the raw shadowgrams used for the current image velocimetry.

5.B   Correlation profiles

The main text presents shadowgrams of CO_2 at supercritical pressure, and considers the fluid motion that can be deducted from their cross-correlation. Besides fluid motion, the analysis of the shapes of the cross-correlation functions themselves reveals additional information about the characteristics of the flow that helps substantiate the qualitative descriptions of the flow phenomena seen in the shadowgrams in the main body of the manuscript. Specifically, the correlation profiles convey the direction of the apparent flow and the degree of correlation between consecutive shadowgrams. Moreover, by fitting Gaussian profiles to the correlations (Oldenziel et al., 2023), the variability in the correlated displacements can be examined. Figures 5.20 and 5.21 show the cross correlation functions for both stratification types considered in the current work. In the figures, the standard deviations of the Gaussian fit is given for both principal directions.

5

$\mathrm{Re}_{Dh} = 0.5{\cdot}10^3$ $\mathrm{Re}_{Dh} = 0.5{\cdot}10^3$ $\mathrm{Re}_{Dh} = 2.2{\cdot}10^3$ $\mathrm{Re}_{Dh} = 2.2{\cdot}10^3$ $\mathrm{Re}_{Dh} = 3.3{\cdot}10^3$ $\mathrm{Re}_{Dh} = 3.3{\cdot}10^3$
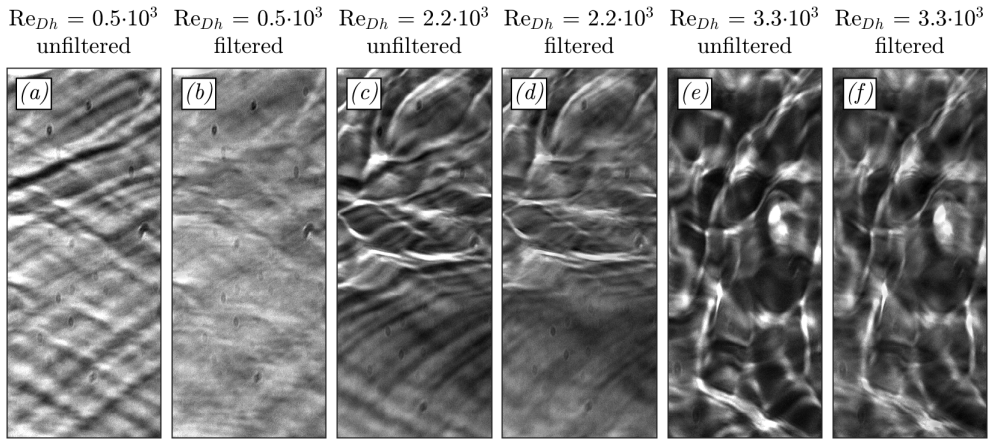   unfiltered   filtered   unfiltered   filtered   unfiltered   filtered

Figure 5.19: Assessment of effectiveness of current optical filter. The filter removes the background patterns cast by surface finish imperfections of the visors. Optical filter image pairs are shown for case R1 in (a) & (b), case R3 in (c) & (d), and for case R5 in (e) & (f).

In figure 5.20, the averaged correlations of several bottom-up heated cases are considered. For a neutrally buoyant flow, the correlation averages assume the shape of horizontal striations. There, either zero or non-zero streamwise displacements are correlated, depending on the presence of variable density turbulence (see also figure 5.6 of the main text). As a result, despite the strong correlation of the shadowgram pairs, the variability in the correlated streamwise displacements can be significant. When the flow is dominated by natural convection, the shadowgrams are characterized by disorganized chaos. There, consecutive image pairs decorrelate as many thermal structures overlap in the depth averaging shadowgrams. As a result, the correlation peak weakens and the variability of the correlations increases, decreasing the reliability of the correlated displacements. In between the extremes, at intermediate heating rates, finite vertical and streamwise displacements are captured with the sparsely present 'thermal tracers.' It is for this range that displacement rates are reported in the main text.

The averaged correlations of unstably stratified supercritical pressure CO_2 are shown in figure 5.21. As top-down heating is applied to the channel, the standard deviations of the correlation profiles along the vertical axis decrease, indicating a reduction of the displacement fluctuations in the vertical direction in line with section 5.4.3. Furthermore, as the flow of CO_2 stratifies, an increasingly large layer of homogeneous brightness is formed near the heated wall in the shadowgrams, in which a zero-mean
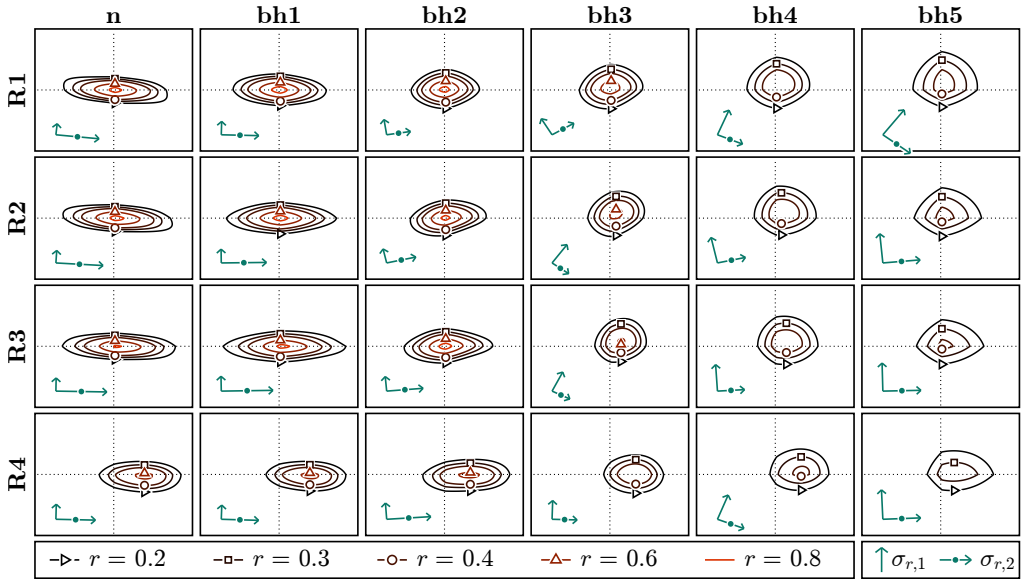
Figure 5.20: Isocontours of correlation-averaged image-pair correlations (for the current 128x128 windows) for the cases shown in figure 5.2. For bh5, a bottom-upwards heat flux of $\dot{q} = 12.0$ kWm^{-2} is applied. The figure denotes the correlation strength r of the shown isocontours, and the standard deviations of the Gaussian fitted to the averaged correlation (Oldenziel et al., 2023) in the two principal directions, $\sigma_{r,1}$ and $\sigma_{r,2}$ respectively. The positions of the symbols in the correlation profiles indicate the positions of their maxima along the x-axis.

streamwise velocity is correlated due to the absence of 'thermal tracers.' As a result, the variability of the averaged correlated streamwise displacements increases, stretching the cross-correlation profiles of the shadowgram pairs upon the inception of the homogeneous layer. As can be seen from the figure, the onset of this stretching occurs at increasingly large heating rates for increasing Reynolds numbers. Eventually, upon the homogenisation of a substantial fraction of the channel height, a zero-mean streamwise velocity is correlated. Thereafter, the correlation of shadowgram image pairs no longer yields fluid motion within the bulk of the flow.

5.C   Stability map

To represent the current stable stratification results in a way that facilitates the identi-fication and prediction of stability boundaries, this appendix presents a stability map
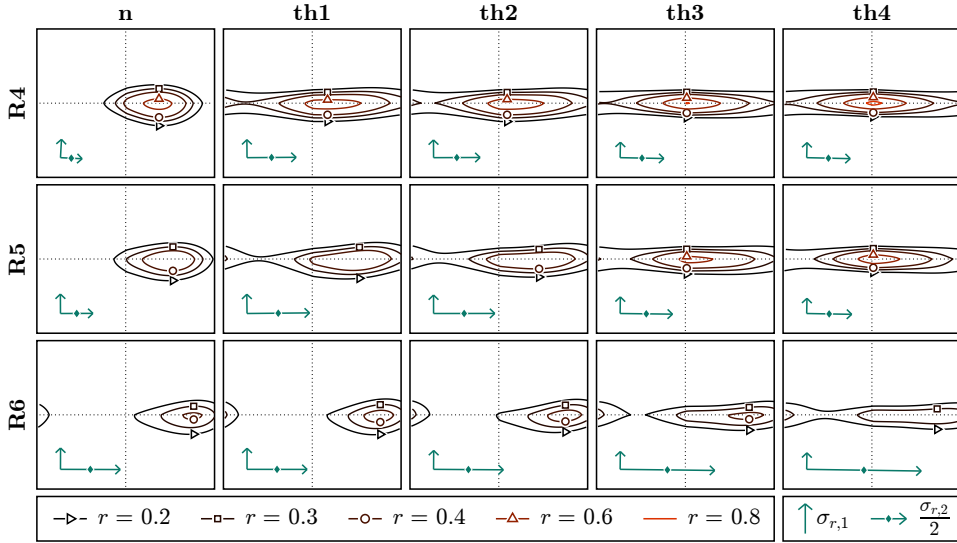
Figure 5.21: Isocontours of correlation-averaged image-pair correlations (for the current 128x128 windows) for a selection of the cases shown in figure 5.3. The figure denotes the correlation strength r of the shown isocontours, and the standard deviations of the Gaussian fitted to the averaged correlation (Oldenziel et al., 2023) in the two principal directions, $\sigma_{r,1}$ and $\sigma_{r,2}$ respectively. The positions of the symbols in the correlation profiles indicate the positions of their maxima along the x-axis.

derived from shadowgraphy data. Initially, the experimental results are expressed using the quantities commonly employed in stability maps for subcritical fluid stratification (Gage and Reid, 1968), enabling a direct comparison.

To position the current experiments on the linear stability map of Gage and Reid (1968), the results should be expressed in terms of the friction-based parameters Re_τ and Ri_τ, defined as:

$$Re_\tau = \frac{\rho_b u_\tau \frac{h}{2}}{\mu_b}, \quad Ri_\tau = \frac{g(\rho_{b1} - \rho_w)\frac{h}{2}}{\rho_b u_\tau^2}, \tag{5.10}$$

for which

$$u_\tau = \sqrt{\frac{\tau_w}{\rho_0}}. \tag{5.11}$$

To determine Re_τ and Ri_τ, a value for τ_w is required. Under the conditions of the present experiments, τ_w is strongly modulated by variable viscosity and near-wall velocity acceleration Nemati et al. (2015). However, no existing friction model
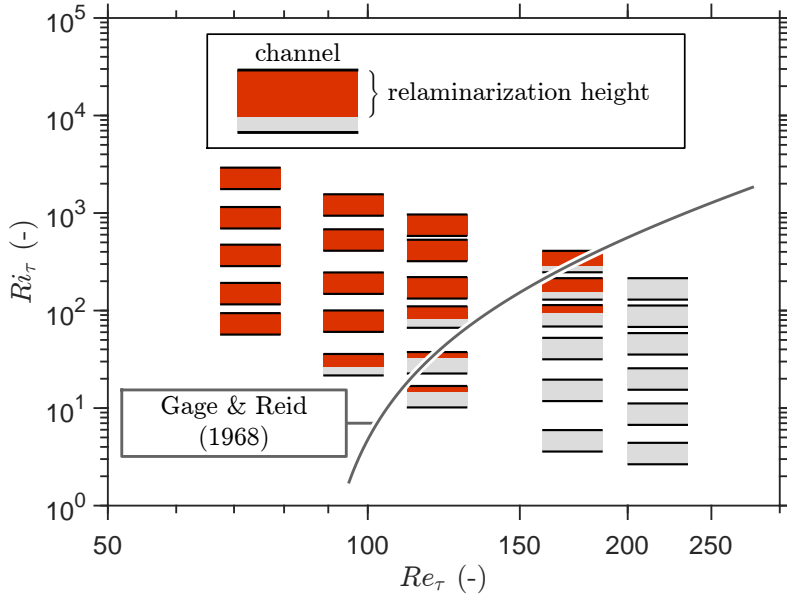
Figure 5.22: Idealised Re_τ - Ri_τ space of current stably stratified results. For each of the shown cases, the distance from the heated top wall for which the flow within the channel is considered to have relaminarised is specified in red. The fit by Zonta and Soldati (2018) of the neutral curve obtained from the linear stability analysis of Gage and Reid (1968) is furthermore indicated in the figure.

accurately captures the modulation of τ_w by buoyancy for this specific stably stratified configuration (see, for instance, Ehsan et al. (2018)). Therefore, τ_w is approximated by simplifying the problem and neglecting thermodynamic property variations in CO_2. One possible approach is to estimate τw using the Blasius friction model:

$$\tau_w = \frac{f\rho_b u_b^2}{2}, \quad f = \frac{0.0791}{Re_{\text{Dh}}^{0.25}}, \tag{5.12}$$

where the bulk properties ρ_b and u_b are evaluated at the inlet conditions of the optical test section (T_{03}, P_{02} of figure 2.3).

The resulting values of Re_τ and Ri_τ for cases R4-R8 and a selection of heat flux values ($\dot{q}$) are presented in figure 5.22. In the figure, the normalized thickness of the homogenized layer is indicated in red. As demonstrated in the space-time visualizations in section 5.4.3 of the manuscript and in appendix 5.B, the thermal 'tracers' in the shadowgrams progressively vanish in the homogenized layer under stable stratification, leading to a reduction of the correlated displacement rate to zero.
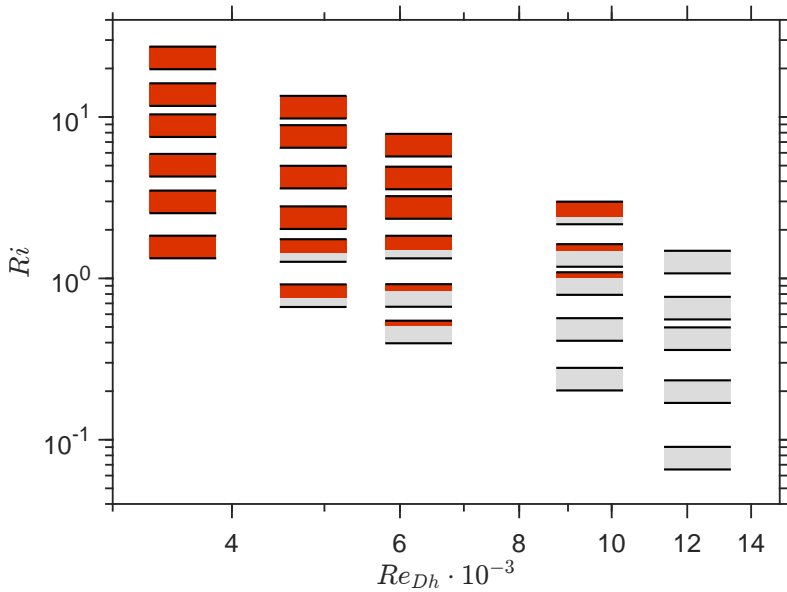
5

Figure 5.23: Nominal Re_{Dh} - Ri space of current stably stratified results. For each of the shown cases, the distance from the heated top wall for which the flow within the channel is considered to have relaminarised is specified in red.

This characteristic is then used to quantify the thickness of the relaminarized layer in the shadowgrams: once the mean correlated displacement rate at a given point falls below a specified fraction (currently $\frac{2}{3}$ of its neutrally buoyant value), the flow at that point is considered relaminarized. In figure 5.22, the normalized channel height at which the flow has relaminarized is marked in red, while the remaining turbulent portion of the channel is shown in gray.

As observed in figure 5.22, a finite-thickness homogenized layer emerges in proximity to the neutral stability curve of Gage and Reid (1968) when the simplified model for τ_w is applied. However, this direct comparison is inherently misleading due to the simplifications in modeling the skin friction. The actual values of Re_τ and Ri_τ in our experiments differ significantly from those in the figure due to the strong modulation of u_τ by variations in the thermophysical properties of CO_2. Consequently, the applicability of the stability boundary proposed by Gage and Reid (1968) to our specific experimental configuration cannot be directly inferred from figure 5.22.

Conversely, presenting the current experiments in terms of Re_{Dh} and Ri as defined in equation (5.1) in figure 5.23 provides a more accurate representation of the stability boundaries of the system. However, in this formulation, a direct comparison with the

stability map of Gage and Reid (1968) is no longer feasible.

5

5

Chapter 6

Conclusions

Experiments rarely reveal only the results one sets out to observe. More often, they uncover physical phenomena that were overlooked, underestimated, or entirely unexpected. In the present work, buoyancy effects proved more influential than initially anticipated. These effects overshadowed other physical mechanisms, and gave rise to the most insightful findings presented in this dissertation.

> What I now know is a drop,
> What I do not yet know is an ocean.
>
> Isaac Newton (adapted)

This final chapter summarizes the key findings of this research and presents the corresponding conclusions. The conclusions are organized to align with the topics explored in the main chapters of the thesis. Additionally, this chapter provides perspectives on potential directions for future research.

6.1 Conclusions

This thesis investigates the influence of buoyancy on the turbulence and stability of continuous supercritical fluid flow, to elucidate the underlying physics of the highly non-ideal and configuration-dependent heat transfer observed in supercritical flow systems, where buoyancy is often identified as a major contributor. The flow of supercritical pressure CO_2 is analyzed through concurrent optical analysis (shadowgraphy) and heat transfer measurements, providing a detailed assessment of buoyancy-driven effects. Gaining a more comprehensive insight into these effects is crucial for the design of heat exchangers in novel energy conversion systems operating at supercritical pressures. These systems have gained significant recent interest for their potential to sustainably produce power and industrial heat.

6.1.1 Natural circulation

To enable the optical experiments in this thesis, carbon dioxide is circulated by buoyancy within a natural circulation facility, which is described in chapter 2. However, since both the steady-state flow rate and the stability boundaries of natural circulation at supercritical pressures were previously not well defined — particularly in an experimental setting — they are investigated in this thesis.

6.1.1.1 Steady state

To describe the steady-state mass flow rate, chapter 3 presents an equation that extends existing models for subcritical single-phase natural circulation loops to supercritical conditions. The equation is experimentally validated by independently varying the system's filling mass, heating rate, imposed driving height, external pressure drop, and coolant temperature. Within the explored operational range, the predicted flow rate closely matches experimental observations. The model successfully captures several notable characteristics of supercritical pressure natural circulation, including the higher mass flow rate for liquid-like thermodynamic states, a peak in mass flow rate just before the pseudo-boiling curve, and a minimum in driving temperature at constant heating rates near the pseudo-critical curve, where specific heat reaches its maximum.

6

6.1.1.2 Stability

Supercritical pressure natural circulation loops have been predicted to become unstable under certain conditions, potentially leading to thermal fatigue. To ensure their viability as passive heat removal systems in nuclear applications and for the current optical experiments, chapter 4 experimentally investigates the stability boundaries of these loops and explores possible instability mitigation strategies.

Instabilities are triggered when the rate of thermodynamic change in the heaters increases, which is achieved by reducing the mass flow rate while maintaining a constant heat flux. In the current facility, oscillatory instabilities emerge before the predicted stability boundaries. A static model of the loop's heat exchangers suggests that the instability is not of a static nature. Instead, the oscillations originate from heat transfer deterioration in the NCL heaters, which leads to the formation of traveling density waves. These waves, in turn, periodically reinforce the deterioration, creating a self-sustaining cycle of instability. Since the passage of thermal waves is essential for sustaining these oscillations, mitigating their propagation can stabilize the system. This can be achieved by increasing the diffusion of the thermal waves by introducing design modifications such as a control valve or a system bypass. These measures help disrupt the feedback loop driving the instability, greatly improving the stability of the NCL.

6.1.2 Flow visualization

In chapter 5, shadowgraphy is used to visualize the side-view, path-integrated flow field of hydrodynamically developed carbon dioxide flow at supercritical pressures. When the temperature distribution within the CO_2 is sufficiently heterogeneous for the current experimental conditions ($p = 88.5$ bar and $T = 32.6°C$), distinct thermal structures appear in the shadowgrams. By correlating their displacements, velocity fields can be obtained. It is validated that the mean streamwise displacement rates of these pseudo-tracers correspond to the mean flow velocity, provided the CO_2 is sufficiently turbulent and neutrally buoyant. As such, these structures move with the flow and act as thermal tracers, visualizing flow motion within the test section. However, the shadow image velocimetry is characterized by relatively large uncertainties, as the method depends on the local occurrence of density fluctuations (leading to variations in refractive index) of the flow, and the finite coherence of these structures in time. Despite these limitations, shadowgraphy effectively distinguishes flow movement patterns that are unique to the two different stratification types examined in this thesis.

6

6.1.3   Thermal stratification & heat transfer

To induce stratification in the optically accessible heat exchanger channel, heating is applied either to the top or bottom surface in the experiments described in chapter 5. The CO_2 starts in a liquid-like state and is heated toward the pseudo-critical curve, where sharp variations in thermodynamic properties lead to strong stratifications, even at moderate heating rates. These stratifications modify the initially neutrally buoyant base flow, either enhancing or suppressing variability in the shadowgrams, depending on the stratification type. In contrast, achieving a comparable degree of stratification in subcritical single-phase fluids would require significantly larger channels and higher heating rates.

When heating is applied from the bottom, strong secondary flow structures emerge. Light plumes intermittently detach from the heated surface, increasing in both frequency and velocity as heating intensifies. These plumes enhance energy exchange with the wall, reinforcing heat transfer augmentation by the increased near-wall heat capacity of the supercritical working fluid. Consequently, the Nusselt number progressively rises compared to the neutrally buoyant case across all tested Reynolds numbers.

In contrast, when heating is applied to the top surface, fluctuations in the shadowgrams diminish, indicating a suppression of vertical motion and mixing. Shadowgraphy further reveals that heat removal from the heated surface is restricted, counteracting the heat transfer enhancement by varying specific heat capacity. As a result, at higher heating rates, heat transfer deteriorates beyond an optimum.

6.2   Future outlook

The current findings indicate that buoyancy strongly influences heat transfer in typical heat exchangers. Heat transfer measurements show significant deviations from neutrally buoyant flow behavior. An optical analysis of the flow through shadowgraphy and its velocimetry qualitatively supports this observation. To better understand these flows, the optical diagnostics used in this study should be refined. For example, generating *in situ* thermal tracers could increase the spatial resolution of the shadow velocimetry and broaden the range of flow rates for which it is applicable. Furthermore, maintaining a controlled ambient temperature in the test section may reduce the intermittent blurring of the shadowgrams. This would expand the experimental framework to cover a broader thermodynamic range at supercritical pressures, including more gas-like initial states.

At the same time, new flow measurement techniques are needed to obtain planar data for fluids at supercritical pressures. Such advancements would overcome the

inherent limitations of shadow velocimetry. For instance, shadow velocimetry fails when the temperature field becomes homogeneous under stable stratification. New methods would yield planar velocity fields that can directly benchmark turbulence and viscous loss models in flows with significant thermophysical variations. Addressing this challenge requires adapting (volume illuminated) particle image velocimetry techniques (Meinhart et al., 2000; Sinton, 2004; Wereley and Meinhart, 2010), for which several hurdles remain. One difficulty is ensuring proper density matching with the property-variant supercritical fluid for larger particles, which tend to settle in the absence of a mean upward bulk flow (Melling, 1997; Adrian and Westerweel, 2011). Another challenge is resolving compatibility issues when using smaller or fluorescent particles - both usually comprised of polymers - with supercritical fluids (Ansaloni et al., 2020; Al-Enezi, 2017). Moreover, as demonstrated in Chapter 5, local density variations can refract light from the particles. This refraction causes apparent displacements to differ from actual ones. Although correcting these distortions will require careful calibration and characterization, it is a necessary step toward achieving accurate measurements.

At this point, it is evident that optical measurement techniques can be applied to study flows in fluids with highly variable properties. As such, further research should explore additional heat transfer configurations where the interplay between buoyancy and variable properties is less pronounced than in the current horizontal flow setup. As optical techniques continue to advance, these investigations are expected to move beyond qualitative descriptions, ultimately paving the way for robust, predictive models for flows within heat exchangers in energy conversion systems.

6

6

References

Adamson, K., Walmsley, T., Carson, J., Chen, Q., Schlosser, F., Kong, L., and Cleland, D. (2022). High-temperature and transcritical heat pump cycles and advancements: A review. *Renew. Sustain. Energy Rev.*, 167:112798.

Adebiyi, G. A. and Hall, W. B. (1976). Experimental investigation of heat transfer to supercritical pressure carbon dioxide in a horizontal pipe. *Int. J. Heat Mass Transf.*, 19(7):715–720.

Adrian, R. J. and Westerweel, J. (2011). *Particle image velocimetry*. Number 30. Cambridge university press.

Ahn, Y., Bae, S., Kim, M., Cho, S., Baik, S., Lee, J., and Cha, J. (2015). Review of supercritical CO_2 power cycle technology and current status of research and development. *Nucl. Eng. Technol.*, 47(6):647–661.

Al-Enezi, S. (2017). Co2 induced foaming behavior of polystyrene near the glass transition. *Int. J. Polym. Sci.*, 2017(1):7804743.

Ambrosini, W. and Sharabi, M. (2008). Dimensionless parameters in stability analysis of heated channels with fluids at supercritical pressures. *Nucl. Eng. Des.*, 238(8):1917–1929.

Angelino, G. (1968). Carbon dioxide condensation cycles for power production. *J. Eng. Power*, 90(3):287–295.

Ansaloni, L., Alcock, B., and Peters, T. (2020). Effects of CO_2 on polymeric materials in the CO_2 transport chain: A review. *Int. J. Greenh. Gas Control*, 94:102930.

Austin, B. and Sumathy, K. (2011). Transcritical carbon dioxide heat pump systems: A review. *Renew. Sustain. Energy Rev.*, 15(8):4013–4029.

Bae, J. H., Yoo, J. Y., and Choi, H. (2005). Direct numerical simulation of turbulent supercritical flows with heat transfer. *Phy. Fluids*, 17(10).

Bae, Y., Kim, H., and Kang, D. (2010). Forced and mixed convection heat transfer to supercritical co2 vertically flowing in a uniformly-heated circular tube. *Exp. Therm. Fluid Sci.*, 34(8):1295–1308.

Banuti, D. T. (2015). Crossing the widom-line–supercritical pseudo-boiling. *J. Supercrit. Fluids*, 98:12–16.

BBC (2025). Trump vows to leave paris climate agreement and 'drill, baby, drill'. `https://www.bbc.com/news/articles/c20px1e05w0o`.

Blass, A., Zhu, X., Verzicco, R., Lohse, D., and Stevens, R. J. A. M. (2020). Flow organization and heat transfer in turbulent wall sheared thermal convection. *J. Fluid Mech.*, 897:A22.

Bodkha, K. and Maheshwari, N. (2021). Heat transfer in supercritical fluids: A review. *J. Nucl. Eng. Radiat. Sci.*, 7(3):030802.

Boldini, P., Bugeat, B., Peeters, J., Kloker, M., and Pecnik, R. (2024a). Direct numerical simulations of k-type transition in a flat-plate boundary layer with supercritical fluids. *arXiv preprint arXiv:2411.14286*.

Boldini, P., Bugeat, B., Peeters, J., Kloker, M., and Pecnik, R. (2024b). Transient growth in diabatic boundary layers with fluids at supercritical pressure. *Phys. Rev. Fluids*, 9(8):083901.

Boure, J. A., Bergles, A. E., and Tong, L. S. (1973). Review of two-phase flow instability. *Nucl. Eng. Des.*, 25(2):165–192.

Boussinesq, J. (1897). *Théorie de l'écoulement tourbillonnant et tumultueux des liquides dans les lits rectilignes à grande section*, volume 1. Gauthier-Villars.

Brunner, G. (2010). Applications of supercritical fluids. *Annu. Rev. Chem. Biomol. Eng.*, 1(1):321–342.

Bugeat, B., Boldini, P., Hasan, A., and Pecnik, R. (2024). Instability in strongly stratified plane couette flow with application to supercritical fluids. *J. Fluid Mech.*, 984:A31.

Cabeza, L., de Gracia, A., Fernández, A., and Farid, M. (2017). Supercritical co_2 as heat transfer fluid: A review. *Appl. Therm. Eng.*, 125:799–810.

Cattafesta, L., Bahr, C., and Mathew, J. (2010). Fundamentals of wind-tunnel design. *Encyclopedia of Aerospace Engineering*, pages 1–10.

Caulfield, C. P. (2021). Layering, instabilities, and mixing in turbulent stratified flows. *Ann. Rev. Fluid Mech.*, 53(1):113–145.

Chatoorgoon, V. (2001). Stability of supercritical fluid flow in a single-channel natural-convection loop. *Int. J. Heat Mass Transf.*, 44(10):1963–1972.

Chen, L., Deng, B., and Zhang, X. (2013). Experimental investigation of CO_2 thermosyphon flow and heat transfer in the supercritical region. *Int. J. Heat Mass Transf.*, 64:202–211.

Chen, L., Zhang, X., and Jiang, B. (2014). Effects of heater orientations on the natural circulation and heat transfer in a supercritical CO_2 rectangular loop. *J. Heat Transf.*, 136(5):052501.

Cheng, L., Wang, Q., and Xu, J. (2024). Supercritical heat transfer of CO_2 in horizontal tube emphasizing pseudo-boiling and stratification effects. *Int. J. Heat Mass Transf.*, 220:124953.

Chu, X. and Laurien, E. (2016). Flow stratification of supercritical CO_2 in a heated horizontal pipe. *J. Supercrit. Fluids*, 116:172–189.

Crespi, F., Gavagnin, G., Sánchez, D., and Martínez, G. (2017). Supercritical carbon dioxide cycles for power generation: A review. *Appl. Energy*, 195:152–183.

Debrah, S. K., Ambrosini, W., and Chen, Y. (2013). Discussion on the stability of natural circulation loops with supercritical pressure fluids. *Ann. Nucl. Energy*, 54:47–57.

Deusebio, E., Caulfield, C. P., and Taylor, J. R. (2015). The intermittency boundary in stratified plane Couette flow. *J. Fluid Mech.*, 781:298–329.

Dostal, V., Hejzlar, P., and Driscoll, M. (2006). High-performance supercritical carbon dioxide cycle for next-generation nuclear reactors. *Nucl. Technol.*, 154(3):265–282.

Draskic, M., Bugeat, B., and Pecnik, R. (2024). The steady behavior of the supercritical carbon dioxide natural circulation loop. *Energy*, 294:130735.

Dunham, M. and Iverson, B. (2014). High-efficiency thermodynamic power cycles for concentrated solar power systems. *Renew. Sustain. Energy Rev.*, 30:758–770.

EC (2025a). Consequences of climate change. `https://climate.ec.europa.eu/climate-change/consequences-climate-change_en`.

EC (2025b). Net electricity generation by type of fuel. `https://ec.europa.eu/eurostat/databrowser/view/NRG_CB_PEM__custom_5180368/default/table?lang=en`.

EEA (2015). Correlation of energy consumption and gdp per person. `https://www.eea.europa.eu/en/analysis/maps-and-charts/correlation-of-per-capita-energy`.

Ehsan, M., Guan, Z., and Klimenko, A. (2018). A comprehensive review on heat transfer and pressure drop characteristics and correlations with supercritical CO_2 under heating and cooling applications. *Renew. Sustain. Energy Rev.*, 92:658–675.

Elton, D. N., Arunachala, U. C., and Vijayan, P. K. (2020). Investigations on the dependence of the stability threshold on different operating procedures in a single-phase rectangular natural circulation loop. *Int. J. Heat Mass Transf.*, 161:120264.

Fang, X., Xu, L., Chen, Y., and Chen, W. (2020). Correlations for friction factor of turbulent pipe flow under supercritical pressure: Review and a new correlation. *Prog. Nucl. Energy*, 118:103085.

Fang, X., Xu, Y., Su, X., and Shi, R. (2012). Pressure drop and friction factor correlations of supercritical flow. *Nucl. Eng. and Des.*, 242:323–330.

Gage, K. S. and Reid, W. H. (1968). The stability of thermally stratified plane Poiseuille flow. *J. Fluid Mech.*, 33(1):21–32.

Garai, A., Kleissl, J., and Sarkar, S. (2014). Flow and heat transfer in convectively unstable turbulent channel flow with solid-wall heat conduction. *J. Fluid Mech.*, 757:57–81.

García-Villalba, M. and Del Alamo, J. C. (2011). Turbulence modification by stable stratification in channel flow. *Phys. Fluids*, 23(4):045104.

Garg, P., Kumar, P., and Srinivasan, K. (2013). Supercritical carbon dioxide brayton cycle for concentrated solar power. *J. Supercrit. Fluids*, 76:54–60.

Garg, V. and Dutta, G. (2020). Understanding of thermal-hydraulic instabilities and the mutual interactions at supercritical pressure. *Int. J. Heat Mass Transf.*, 152:119491.

Guo, Z., Zhao, Y., Zhu, Y., Niu, F., and Lu, D. (2018). Optimal design of supercritical CO_2 power cycle for next generation nuclear power conversion systems. *Prog. Nucl. Energy*, 108:111–121.

Hall, W. B., Jackson, J. D., and Watson, A. (1967). Paper 3: A review of forced convection heat transfer to fluids at supercritical pressures. In *Proceedings of the*

institution of mechanical engineers, conference proceedings, volume 182, pages 10–22. SAGE Publications Sage UK: London, England.

Hargather, M. J., Lawson, M. J., Settles, G. S., and Weinstein, L. M. (2011). Seedless velocimetry measurements by schlieren image velocimetry. *AIAA J.*, 49(3):611–620.

Hasan, A., Larsson, J., Pirozzoli, S., and Pecnik, R. (2023). Incorporating intrinsic compressibility effects in velocity transformations for wall-bounded turbulent flows. *Phys. Rev. Fluids*, 8(11):L112601.

Hasan, A. and Pecnik, R. (2024). Variable-property and intrinsic compressibility corrections for turbulence models using near-wall scaling theories. *arXiv preprint arXiv:2410.14637*.

Huang, D., Wu, Z., Sunden, B., and Li, W. (2016). A brief review on convection heat transfer of fluids at supercritical pressures in tubes and the recent progress. *Appl. Energy*, 162:494–505.

Huang, J., Zhou, Y., Huang, Y., Luo, Q., Yuan, Y., Yang, C., and Hu, W. (2024). Experimental study of pressure drop oscillation in a supercritical carbon dioxide natural circulation loop. *Int. J. Heat Mass Transf.*, 220:125005.

IEA (2019). Renewables 2019. `https://www.iea.org/reports/renewables-2019`.

IEA (2022). The future of heat pumps. `https://www.iea.org/reports/the-future-of-heat-pumps`.

IEA (2024). Electricity 2024. `https://www.iea.org/reports/electricity-2024/`.

IRENA (2023). Power to heat and cooling: Status. `https://www.irena.org/Innovation-landscape-for-smart-electrification/Power-to-heat-and-cooling/Status`.

Jackson, J. D. (1979). Forced convection heat transfer to fluids at supercritical pressure. *Turbulent forced convection in channels and bundles*, 2:563.

Jackson, J. D. (2013). Fluid flow and convective heat transfer to fluids at supercritical pressure. *Nucl. Eng. Des.*, 264:24–40.

Jain, P. K. and Rizwan-uddin (2008). Numerical analysis of supercritical flow instabilities in a natural circulation loop. *Nucl. Eng. Des.*, 238(8):1947–1957.

Jiang, P., Zhang, Y., Xu, Y., and Shi, R. (2008). Experimental and numerical investigation of convection heat transfer of CO_2 at supercritical pressures in a vertical tube at low reynolds numbers. *Int. J. Therm. Sci.*, 47(8):998–1011.

Jonassen, D. R., Settles, G. S., and Tronosky, M. D. (2006). Schlieren "PIV" for turbulent flows. *Opt. Lasers Eng.*, 44(3-4):190–207.

Kakaç, S. and Bon, B. (2008). A review of two-phase flow dynamic instabilities in tube boiling systems. *Int. J. Heat Mass Transf.*, 51(3-4):399–433.

Lefauve, A. and Couchman, M. (2024). Data-driven classification of sheared stratified turbulence from experimental shadowgraphs. *Phys. Rev. Fluids*, 9(3):034603.

Lemmon, E. W., Bell, I. H., Huber, M. L., and McLinden, M. O. (2018). NIST Standard Reference Database 23: Reference Fluid Thermodynamic and Transport Properties-REFPROP, Version 10.0, National Institute of Standards and Technology.

Li, D., Luo, K., and Fan, J. (2017). Buoyancy effects in an unstably stratified turbulent boundary layer flow. *Phys. Fluids*, 29(1):015104.

Li, Y., Yuan, B., and Du, W. (2022). Experimental investigation of near-critical CO_2 heat transfer performance in a closed natural circulation loop. *Int. J. Heat Mass Transf.*, 196:123225.

Liao, G., Liu, L., Jiaqiang, E., Zhang, F., Chen, J., Deng, Y., and Zhu, H. (2019). Effects of technical progress on performance and application of supercritical carbon dioxide power cycle: A review. *Energy Convers. Manag.*, 199:111986.

Licht, J., Anderson, M., and Corradini, M. (2008). Heat transfer to water at supercritical pressures in a circular and square annular flow geometry. *Int. J. Heat Fluid Flow*, 29(1):156–166.

Lienhard V, J. H. and Van Atta, C. W. (1990). The decay of turbulence in thermally stratified flow. *J. Fluid Mech.*, 210:57–112.

Liu, G., Huang, Y., and Wang, J. (2019). A new theoretical model of steady-state characteristics of supercritical carbon dioxide natural circulation. *Energy*, 189:116323.

Liu, G., Huang, Y., Wang, J., Lv, F., and Leung, L. (2016). Experiments on the basic behavior of supercritical CO_2 natural circulation. *Nucl. Eng. Des.*, 300:376–383.

Liu, G., Huang, Y., Wang, J., Lv, F., and Liu, S. (2017). Experimental research and theoretical analysis of flow instability in supercritical carbon dioxide natural circulation loop. *Appl. Energy*, 205:813–821.

Lopes, N., Chao, Y., Dasarla, V., Sullivan, N., Ricklick, M., and Boetcher, S. (2022). Comprehensive review of heat transfer correlations of supercritical CO_2 in straight tubes near the critical point: a historical perspective. *J. Heat Transf.*, 144(12):120801.

Ma, Y., Liu, Z., and Tian, H. (2013). A review of transcritical carbon dioxide heat pump and refrigeration cycles. *Energy*, 55:156–172.

Marchionni, M., Bianchi, G., and Tassou, S. (2020). Review of supercritical carbon dioxide (sCO_2) technologies for high-grade waste heat to power conversion. *SN Appl. Sci.*, 2(4):611.

Mehta, R. D. and Bradshaw, P. (1979). Design rules for small low speed wind tunnels. *Aeronaut. J.*, 83(827):443–453.

Meinhart, C. D., Wereley, S. T., and Gray, M. H. B. (2000). Volume illumination for two-dimensional particle imagevelocimetry. *Meas. Sci. Technol.*, 11(6):809.

Melling, A. (1997). Tracer particles and seeding for particle image velocimetry. *Meas. Sci. Technol.*, 8(12):1406.

Merzkirch, W. (2012). *Flow visualization*. Elsevier.

Michelis, T., Head, A. J., Majer, M., Colonna, P., and De Servi, C. M. (2024). Assessment of particle image velocimetry applied to high-speed organic vapor flows. *Exp. Fluids*, 65:90.

Michels, A. M. J. F. and Hamers, J. B. A. A. (1937). The effect of pressure on the refractive index of CO_2: The Lorentz-Lorenz formula. *Physica*, 4(10):995–1006.

NASA (2024). Global land-ocean temperature index. `https://climate.nasa.gov/vital-signs/global-temperature/?intent=121`.

Nemati, H., Patel, A., Boersma, B. J., and Pecnik, R. (2015). Mean statistics of a heated turbulent pipe flow at supercritical pressure. *Int. J. Heat Mass Transf.*, 83:741–752.

Nieuwstadt, F. T. M. (2005). Direct numerical simulation of stable channel flow at large stability. *Boundary-Layer Meteorol.*, 116:277–299.

Oberbeck, A. (1879). Über die wärmeleitung der flüssigkeiten bei berücksichtigung der strömungen infolge von temperaturdifferenzen. *Ann. Phys. Chem.*, 243(6):271–292.

Ohya, Y., Neff, D. E., and Meroney, R. N. (1997). Turbulence structure in a stratified boundary layer under stable conditions. *Boundary-Layer Meteorol.*, 83:139–162.

Okamoto, K., Ota, J., Sakurai, K., and Madarame, H. (2003). Transient velocity distributions for the supercritical carbon dioxide forced convection heat transfer. *J. Nucl. Sci. Technol.*, 40(10):763–767.

Oldenziel, G., Sridharan, S., and Westerweel, J. (2023). Measurement of high-re turbulent pipe flow using single-pixel piv. *Exp. Fluids*, 64(10):164.

Osorio, J., Hovsapian, R., and Ordonez, J. (2016). Dynamic analysis of concentrated solar supercritical co_2-based power generation closed-loop cycle. *Appl. Therm. Eng.*, 93:920–934.

Patel, A., Boersma, B., and Pecnik, R. (2016). The influence of near-wall density and viscosity gradients on turbulence in channel flows. *J. Fluid Mech.*, 809:793–820.

Patel, A., Peeters, J., Boersma, B., and Pecnik, R. (2015). Semi-local scaling and turbulence modulation in variable property turbulent channel flows. *Phys. Fluids*, 27(9).

Pecnik, R. and Patel, A. (2017). Scaling and modelling of turbulence in variable property channel flows. *J. Fluid Mech.*, 823:R1.

Peeters, J. W. R., Pecnik, R., Rohde, M., van der Hagen, T. H. J. J., and Boersma, B. J. (2016). Turbulence attenuation in simultaneously heated and cooled annular flows at supercritical pressure. *J. Fluid Mech.*, 799:505–540.

Pegallapati, A., Banoth, P., and Maddali, R. (2020). Dynamic model of supercritical co_2 based natural circulation loops with fixed charge. *Appl. Therm. Eng.*, 169:114906.

Petrov, N. E. and Popov, V. N. (1985). Heat-transfer and resistance of carbon-dioxide being cooled in the supercritical region. *Therm. Eng.*, 32(3):131–134.

Pioro, I., Khartabil, H., and Duffey, R. (2004). Heat transfer to supercritical fluids flowing in channels—empirical correlations (survey). *Nucl. Eng. Des.*, 230(1-3):69–91.

Pirozzoli, S., Bernardini, M., Verzicco, R., and Orlandi, P. (2017). Mixed convection in turbulent channels with unstable stratification. *J. Fluid Mech.*, 821:482–516.

Pitla, S., Robinson, D., Groll, E., and Ramadhyani, S. (1998). Heat transfer from supercritical carbon dioxide in tube flow: a critical review. *HVAC&R Res.*, 4(3):281–301.

Raffel, M. (2015). Background Oriented Schlieren (BOS) techniques. *Exp. Fluids*, 56:60.

Rahman, M. E. and Singh, S. (2019). Flow excursions and pressure drop oscillations in boiling two-phase channel. *Int. J. Heat Mass Transf.*, 138:647–658.

Rai, S. K., Kumar, P., and Panwar, V. (2021). Mathematical and numerical investigation of ledinegg flow excursion and dynamic instability of natural circulation loop at supercritical condition. *Ann. Nucl. Energy*, 155:108129.

Rai, S. K., Kumar, P., Tiwari, M., Panwar, V., Kumar, D., and Sharma, V. K. (2025). A comprehensive overview of advancements, applications, and impact of supercritical fluid natural circulation loops. *Ann. Nucl. Energy*, 211:110971.

Ren, J., Fu, S., and Pecnik, R. (2019a). Linear instability of poiseuille flows with highly non-ideal fluids. *J. Fluid Mech.*, 859:89–125.

Ren, J., Marxen, O., and Pecnik, R. (2019b). Boundary-layer stability of supercritical fluids in the vicinity of the widom line. *J. Fluid Mech.*, 871:831–864.

Reshotko, E., Saric, W., Nagib, H., Reshotko, E., Saric, W., and Nagib, H. (1997). Flow quality issues for large wind tunnels. In *35th Aerospace Sciences Meeting and Exhibit*, page 225.

Sadhu, S., Ramgopal, M., and Bhattacharyya, S. (2018a). Experimental studies on an air-cooled natural circulation loop based on supercritical carbon dioxide - part a: Steady state operation. *Appl. Therm. Eng.*, 133:809–818.

Sadhu, S., Ramgopal, M., and Bhattacharyya, S. (2018b). Steady-state analysis of a high-temperature natural circulation loop based on water-cooled supercritical CO_2. *J Heat Transf.*, 140(6).

Sarkar, M. and Basu, D. (2017). Influence of geometric parameters on thermalhydraulic characteristics of supercritical CO_2 in natural circulation loop. *Nucl. Eng. Des.*, 324:402–415.

Scagliarini, A., Gylfason, Á., and Toschi, F. (2014). Heat-flux scaling in turbulent Rayleigh-Bénard convection with an imposed longitudinal wind. *Phys. Rev. E*, 89(4):043012.

Schröder, A., Over, B., Geisler, R., Bulit, A., Schwane, R., and Kompenhans, J. (2009). Measurements of density fields in micro nozzle plumes in vacuum by using an enhanced tomographic Background Oriented Schlieren (BOS) technique. In *The 9th International Symposium on Measurement Science and Intelligent Instruments (ISMTII-2009), Saint Petersburg*.

Settles, G. S. (2001). *Schlieren and shadowgraph techniques: visualizing phenomena in transparent media*. Springer Science & Business Media.

Settles, G. S. and Hargather, M. J. (2017). A review of recent developments in schlieren and shadowgraph techniques. *Meas. Sci. Technol.*, 28:042001.

Sharma, M., Pilkhwal, D. S., Vijayan, P. K., Saha, D., and Sinha, R. K. (2010a). Steady state and linear stability analysis of a supercritical water natural circulation loop. *Nucl. Eng. Des.*, 240(3):588–597.

Sharma, M., Vijayan, P. K., Pilkhwal, D. S., and Asako, Y. (2013). Steady state and stability characteristics of natural circulation loops operating with carbon dioxide at supercritical pressures for open and closed loop boundary conditions. *Nucl. Eng. Des.*, 265:737–754.

Sharma, M., Vijayan, P. K., Pilkhwal, D. S., Saha, D., and Sinha, R. K. (2010b). Linear and Nonlinear Stability Analysis of a Supercritical Natural Circulation Loop. *J. Eng. Gas Turbines Power*, 132(10):102904.

Sinton, D. (2004). Microscale flow visualization. *Microfluid. Nanofluidics*, 1:2–21.

Smith, K. M., Caulfield, C. P., and Taylor, J. R. (2021). Turbulence in forced stratified shear flows. *J. Fluid Mech.*, 910:A42.

Swapnalee, B. T., Vijayan, P. K., Sharma, M., and Pilkhwal, D. S. (2012). Steady state flow and static instability of supercritical natural circulation loops. *Nucl. Eng. Des.*, 245:99–112.

Taler, D. (2016). Determining velocity and friction factor for turbulent flow in smooth tubes. *Int. J. Therm. Sci.*, 105:109–122.

Theologou, K., Mertz, R., Laurien, E., and Starflinger, J. (2022). Experimental investigations on heat transfer of CO_2 under supercritical pressure in heated horizontal pipes. *Energy*, 254(A):124171.

Tian, R., He, S., Wei, M., and Shi, L. (2021). The staged development of a horizontal pipe flow at supercritical pressure. *Int. J. Heat Mass Transf.*, 168:120841.

Tokanai, H., Ohtomo, Y., Horiguchi, H., Harada, E., and Kuriyama, M. (2010). Heat transfer of supercritical co_2 flow in natural convection circulation system. *Heat Transf. Eng.*, 31(9):750–756.

Tropea, C., Yarin, A. L., Foss, J. F., et al. (2007). *Springer handbook of experimental fluid mechanics*, volume 1. Springer.

Turchi, C., Ma, Z., Neises, T., and Wagner, M. (2013). Thermodynamic study of advanced supercritical carbon dioxide power cycles for concentrating solar power systems. *J. Sol. Energy Eng.*, 135(4):041007.

T'Joen, C. and Rohde, M. (2012). Experimental study of the coupled thermo-hydraulic–neutronic stability of a natural circulation hplwr. *Nucl. Eng. Des.*, 242:221–232.

UNCC (2015). Paris agreement. `https://unfccc.int/sites/default/files/english_paris_agreement.pdf`.

Valori, V., Elsinga, G. E., Rohde, M., Westerweel, J., and van der Hagen, T. H. J. J. (2019). Particle image velocimetry measurements of a thermally convective supercritical fluid. *Exp. Fluids*, 60:143.

Venkatakrishnan, L. and Meier, G. E. (2004). Density measurements using the background oriented schlieren technique. *Exp. Fluids*, 37:237–247.

Vijayan, P. (2002). Experimental observations on the general trends of the steady state and stability behaviour of single-phase natural circulation loops. *Nucl. Eng. Des.*, 215(1-2):139–152.

Vijayan, P. and Austregesilo, H. (1994). Scaling laws for single-phase natural circulation loops. *Nucl. Eng. Des.*, 152(1-3):331–347.

Vijayan, P., Sharma, M., and Saha, D. (2007). Steady state and stability characteristics of single-phase natural circulation in a rectangular loop with different heater and cooler orientations. *Experimental Thermal and Fluid Science*, 31(8):925–945.

Vukoslavčević, P. V., Radulović, I. M., and Wallace, J. M. (2005). Testing of a hot-and cold-wire probe to measure simultaneously the speed and temperature in supercritical CO_2 flow. *Exp. Fluids*, 39:703–711.

Wahidi, T., Chandavar, R. A., and Yadav, A. K. (2021). Supercritical co_2 flow instability in natural circulation loop: Cfd analysis. *Ann. Nucl. Energy*, 160:108374.

Wahl, A., Mertz, R., Laurien, E., and Starflinger, J. (2022). Heat transfer deterioration in vertical sco_2 cooling in 3 mm tube. *Energy*, 254:124240.

Wang, J., Huang, Y., Zang, J., and Liu, G. (2014a). Research activities on supercritical carbon dioxide power conversion technology in china. In *Turbo Expo: Power for Land, Sea, and Air*, volume 45660, page V03BT36A009. American Society of Mechanical Engineers.

Wang, Q., Xu, J., Zhang, C., Hao, B., and Cheng, L. (2023a). A critical review on heat transfer of supercritical fluids. *Heat Transf. Eng.*, 44(21-22):1969–1994.

Wang, W., He, S., Moulinec, C., and Emerson, D. R. (2023b). Direct numerical simulation of thermal stratification of supercritical water in a horizontal channel. *Comput. Fluids*, 261:105911.

Wang, Z., Liu, X., Chen, J., Ye, J., He, J., Jia, L., Chen, Y., and Luo, X. (2024). An overview of flow instability at supercritical pressure. *Int. J. Heat Mass Transf.*, 227:125533.

Wang, Z., Sun, B., Wang, J., and Hou, L. (2014b). Experimental study on the friction coefficient of supercritical carbon dioxide in pipes. *Int. J. Greenh. Gas Control*, 25:151–161.

Welander, P. (1967). On the oscillatory instability of a differentially heated fluid loop. *J. Fluid Mech.*, 29(1):17–30.

Wereley, S. T. and Meinhart, C. D. (2010). Recent advances in micro-particle image velocimetry. *Ann. Rev. Fluid Mech.*, 42(1):557–576.

Whitaker, T. A., Cochran, J. W., Hochhalter, J. D., and Rao, S. R. (2024). Flow regimes and heat transfer mechanisms affecting supercritical transition in microchannels. *Int. J. Heat Mass Transfer*, 218:124749.

Williams, O., Hohman, T., Van Buren, T., Bou-Zeid, E., and Smits, A. J. (2017). The effect of stable thermal stratification on turbulent boundary layer statistics. *J. Fluid Mech.*, 812:1039–1075.

WMO (2025). Wmo confirms 2024 as warmest year on record at about $1.55°$c above pre-industrial level. `https://wmo.int/news/media-centre/wmo-confirms-2024-warmest-year-record-about-155degc-above-pre-industrial-level`.

Wolscht, L., Knobloch, K., Jacquemoud, E., and Jenny, P. (2024). Dynamic simulation and experimental validation of a 35 mw heat pump based on a transcritical co_2 cycle. *Energy*, 294:130897.

Wolscht, L., Somaini, R., Jacquemoud, E., and Jenny, P. (2023). Full-scale demonstration and validation of a 35 mw transcritical co_2 heat pump. In *Turbo Expo: Power for Land, Sea, and Air*, volume 87073, page V012T28A002. American Society of Mechanical Engineers.

Wright, S., Davidson, C., and Scammell, W. (2016). Thermo-economic analysis of four sco_2 waste heat recovery power systems. In *Fifth International SCO2 Symposium, San Antonio, TX*, pages 28–31.

Yamagata, K., Nishikawa, K., Hasegawa, S., Fujii, T., and Yoshida, S. (1972). Forced convective heat transfer to supercritical water flowing in tubes. *Int. J. Heat Mass Transf.*, 15(12):2575–2593.

Yoo, J. (2013). The turbulent flows of supercritical fluids with heat transfer. *Ann. Rev. Fluid Mech.*, 45(1):495–525.

Yoshikawa, S., Smith Jr, R., Inomata, H., Matsumura, Y., and Arai, K. (2005). Performance of a natural convection circulation system for supercritical fluids. *J. Supercrit. Fluids*, 36(1):70–80.

Yu, J., Che, S., Li, R., and Qi, B. (2011). Analysis of ledinegg flow instability in natural circulation at supercritical pressure. *Prog. Nucl. Energy*, 53(6):775–779.

Yu, S., Li, H., Lei, X., Feng, Y., Zhang, Y., He, H., and Wang, T. (2013). Experimental investigation on heat transfer characteristics of supercritical pressure water in a horizontal tube. *Exp. Therm. Fluid Sci.*, 50:213–221.

Zhang, S., Xu, X., Liu, C., and Dang, C. (2020). A review on application and heat transfer enhancement of supercritical co2 in low-grade heat conversion. *Appl. Energy*, 269:114962.

Zhang, X., Chen, L., and Yamaguchi, H. (2010). Natural convective flow and heat transfer of supercritical co_2 in a rectangular circulation loop. *Int. J. Heat Mass Transf.*, 53(19-20):4112–4122.

Zhao, A., Pecnik, R., and Peeters, J. W. R. (2024). Thermodynamic analysis and heat exchanger calculations of transcritical high-temperature heat pumps. *Energy Convers. Manage.*, 303:118172.

Zigrang, D. and Sylvester, N. (1985). A review of explicit friction factor equations. *J. Energy Resour. Technol.*, 107:280–283.

Zonta, F., Sichani, P. H., and Soldati, A. (2022). Interaction between thermal stratification and turbulence in channel flow. *J. Fluid Mech.*, 945:A3.

Zonta, F. and Soldati, A. (2014). Effect of temperature dependent fluid properties on heat transfer in turbulent mixed convection. *J. Heat Transf.*, 136(2):022501.

Zonta, F. and Soldati, A. (2018). Stably stratified wall-bounded turbulence. *Appl. Mech. Rev.*, 70(4):040801.

Acknowledgements

My doctoral journey began during a lonely, confusing, and uncertain time defined by COVID lockdowns, curfews, and eerily deserted offices and labs. Fortunately, as the world slowly reopened, I found myself increasingly surrounded by amazing, inspiring people who made the doctoral journey not just bearable, but often genuinely enjoyable. I am deeply grateful for the support, encouragement, and good company of many wonderful individuals, and I'd like to acknowledge some of them here.

First and foremost, I want to thank prof. dr. Rene Pecnik for his mentorship, for making the project that shaped my PhD possible, and for trusting me to start this new experimental chapter. Thank you for your boundless enthusiasm and relentless dedication to the project — qualities that, combined with your remarkable approach-ability,[1] led to frequent chats, countless brainstorms, and many eager (but sometimes destructive[2]) lab visits. I admire your eye for detail, from scientific precision to aesthetics, all while keeping sight of the bigger picture. Lastly, though I stubbornly resisted it at the time (and though I will deny this if asked), you were absolutely right about buying a nicer table for the setup. I would also like to thank prof. dr. ir. Jerry Westerweel for bringing much-needed level-headed experimental expertise to the project from the second year onward. Your guidance helped me navigate a sea of enthusiastic (but often unproven) experimental ideas, and taught me to recognize and appreciate what is actually feasible, without venturing too far into wishful thinking. Even though we only met a few times a year, your advice had a significant influence on many of the experiments and results in this dissertation. A sincere thank you as well to dr. ir. Rene Delfos. Although not directly involved in the project, you generously offered experimental advice on numerous occasions and were the one who first sparked my enthusiasm for experimental research during my master's thesis.

I would also like to thank several highly experienced and knowledgeable colleagues from the Process & Energy laboratory for their help and guidance. Martijn Karsten and Daniël van Baarle, in particular, spent countless hours helping transform my experimental setup from drawing to a functioning reality. I'd like to believe that, thanks

---

[1] Even before the introduction of large language models, Rene's students already enjoyed a similarly impressive level of responsiveness.

[2] Thou shalt hide fragile gaskets and O-rings from thy enthusiastic supervisor.

to their guidance, I no longer have two left hands.[3] My appreciation also goes to Bart Hoek for enthusiastically and candidly sharing his experiences and concerns with similar setups. Those discussions directly sparked our interest in natural circulation — a topic that now makes up roughly half of this dissertation. I am also grateful to Edwin Overmars for sharing his optical expertise and offering advice that helped shape the optical measurement framework used in this work. Also, many thanks to Michel van den Brink for his invaluable help with facility approval and procurement — a process that, according to my mailbox, involved precisely 276 emails.

For a bit more than four years, I have had the honour of being part of the Energy Technology[4] group at the Process & Energy department. I am fairly certain that I have never been surrounded by a more talented pool of individuals. While it was intimidating at first — especially working on a project so different from everyone else's and understanding very little during those early group meetings — I have learned a lot from this amazing group, both through scientific discussions and over many dinners and drinks. For that, I would like to thank the core team of Pietro, Benjamin, Asif, Sanath, Stephan, Simone, and Rene — as well as the extended group with Jurriaan, Teja, An, Ryo, Atharv, Rafael, Bartu, Pedro, Baptiste, and Giandomenico. Pietro, thank you again for the incredible Nikola Jokic figurine which, sadly, looks absolutely nothing like him. I hope we can soon resume our regular basketball chats once we have both crossed the finish line with our dissertations. It's a pity our work didn't end up aligning more closely, your brilliantly complex research certainly deserved an experimental counterpart. Ben, your natural gift for teaching and your unparalleled ability to dissect complex problems from first principles have shaped the way I approach physics. Our discussions helped me make sense of many of the physical complexities I faced early in my PhD. Your future students in your beloved new home, the UK, are incredibly lucky to have you leading the way. Asif, the depth of your understanding of your research, your confidence in challenging even the greats, and the relentless drive and commitment you bring to both your scientific work and life beyond it have been truly inspiring to witness. Sanath, I was deeply honoured when you complimented and even adopted some of my slide layouts and colour schemes. As a small thank-you, I now officially pass the torch: you've earned the right to keep presenting my one and only stratification talk at future conferences — you already know it by heart anyway. And Teja, though I didn't go so far as to get it immortalised on my body like some others did, I was just as excited to finally meet my hero (you) as you were to meet yours (Rafa).

---

[3]For lack of a better English translation, this roughly means being inept at building or fixing things.
[4]The name has changed a few times over the years, but here I've written down the version I liked best.

Whilst being part of this research group, I was also lucky enough to be involved in the supervision of several talented students turned true *Delftse ingenieurs*. Pranav, thank you for your careful and thorough help in shaping the test section for my experiments, and for introducing me to gobi manchurian - a truly life changing event. Ankit, I commend you for confidently navigating your own path in studying complex supercritical fluids with OpenFOAM. Izzy, I deeply appreciate your dedication and enthusiasm for the natural circulation project, and your invaluable continued help in finishing and polishing our work even after your defense — all while patiently putting up with my persistent habit of butchering several languages simultaneously.[5]

One of the absolute highlights of my PhD was securing a prime spot[6] in room 34-K-1-290. Over the years, I had the pleasure of sharing this warm, chatty, and surprisingly productive office with Mengmeng, Zero, Rishabh, Suriya, Heng, Hugo, Elena, Sevgi, Irem, Noura, Darshan, Bartu, Sofen, Sanath, Giandomenico, Baptiste, Anna, Tarun, Shaina, and Letizia. I look back fondly on the many dinners and Secret Santa editions, which reliably escalated into chaos with unsolvable puzzles, fake clues, red herrings, impromptu push-up contests, and the occasional round of singing and dancing. There was also the unforgettable long con by Zero, who, at the age of nine, managed to trick me for an entire year into believing he didn't speak Dutch. Add to that the many late-night conversations and work sessions, one muddy wadlopen adventure, and the eventual retirement of my "PDF-experimentalist" label. I would especially like to thank Suriya, Heng, and Mengmeng for being around from the very beginning, and for being the kind of people I could turn to in both joyful and difficult moments. Thank you all three for trusting me to be your paranymph. Suriya, your infectious excitement for science has made me much more aware and appreciative of the impressive work happening around us. Thank you also Sofen, my friend, for your repeated kind words of appreciation and our many fascinating conversations. Thank you, Giando, for the occasional (and always excellent) snacks and puns. And Sanath: thank you for your many wonderfully unhinged remarks that kept things lively.

At the risk of forgetting some dear people, I would also like to thank several other colleagues by name — including Joe, Wouter, Arvind, Rumen, Maurice, Jelmer, Sohan, Boaz, Lyke, Jesse, Luuk, Rafael, Simone, Parsa, Julien, Gilles, Thanasis, Nikhilesh, Esaar, Nicola, Abhirath, Sowmya, Dirk, Shanwei, Gertjan, Shrinjay, Faruk, Shilong,

---

[5] I tried to compete with the Swiss, and lost.

[6] The perfect balance of privacy and people-watching. Don't get your hopes up, it has already been taken.

Pepijn and Ravi — for the many lighthearted chats, shared meals, and the occasional exchanges of complaints and gossip. Joe and Wouter, thank you for the many lunches we shared and the continued stream of dinner and gig invitations over the years. Shielded by a layer of sharp, grimy wit that repels some and sails over many more heads, you're two of the most sincere and attentive people in the department. Jelmer and Sohan, it was great to share the frame, share experiences, and occasionally vent about our stubborn experimental setups when needed. Thanks also for showing me just how versatile glue can be. Arvind and Rumen, I really enjoyed our board game nights with Suriya, Rishabh, and Heng. I'm sure you will manage to win one someday.

Moreover, I have been fortunate to have a solid group of friends who helped me stay grounded and provided a welcome distraction from research. Thank you to all the guys from *de biergroep* — Kevin, Olivier, Bas, Oscar, Jordi, Pierre, and Jelmer — for the festive dinners and yearly trips, even a decade after high school. Many thanks as well to Berd, Armin, Stefan, and Rama for the great company along the way. I'm especially thankful to my fellow try-hards Lim Chi, Rashed, Stefan, Michael, and Martijn. From sports and gaming to study sessions, work marathons, exotic holidays, or sharing[7] fried chicken at De Kade, you guys were truly always there to make a difference.

I also want to thank my bonus-family of the past few years, the Lugtmeijers. Lia, Michel, and Martijn; thank you for the many lovely dinners and conversations, for your warm hospitality, and for your continued support. Of course, I'm especially grateful to my best friend and favourite Lugtmeijer, Lisanne. Thank you for being close, even when far. I know I've had many moments of distraction and absent-mindedness along the way, and I truly appreciate your patience and unwavering support despite it. I am very excited for the adventures that lie ahead of us.

Lastly, I want to thank my parents, Rade and Zora, for their endless efforts to unburden me over the years. You have taken countless responsibilities off my shoulders and allowed me to fully focus on science and the things I enjoy. I deeply admire and look up to your hard work, your optimism, your boundless kindness and generosity, and the way you have built a life in a new country through your inexhaustible perseverance and determination. I am forever grateful to have you as my parents, thank you for your unwavering care and love. I hope I have made you proud.

---

[7]All of us, but "Joey."

Curriculum Vitae

Marko Draskic was born on September 26th, 1997, in Rotterdam, the Netherlands. After completing his secondary education at the Erasmiaans Gymnasium in Rotterdam, he enrolled in the Bachelor of Science program in Mechanical Engineering at Delft University of Technology in 2015. Motivated by a growing interest in heat transfer, he subsequently pursued a Master of Science in Energy, Flow & Process Technology at the same university, graduating in 2020. During his studies, he was actively involved in the department's study association. His master's thesis, titled "Heatpipes for Geothermal Heat Extraction: A Study on Film Heat Transfer in Heatpipes," focused on enabling the passive extraction of geothermal heat through experimental research on evaporation in falling liquid films.

After completing engineering internships at Hitard Engineering and Dynaflow Research Group, he began his doctoral research in the Process & Energy Department at Delft University of Technology in November 2020. This dissertation is the culmination of his work as a PhD candidate. Throughout his doctoral studies, Marko remained engaged with his academic peers, contributing to the organization of various departmental events and initiatives, as well as the sixth edition of the European Conference on Supercritical CO_2 for Energy Systems.

List of publications

Journal Publications

1. **M. Draskic**, J. Westerweel and R. Pecnik, *The stability of stratified horizontal flows of carbon dioxide at supercritical pressures*, Journal of Fluid Mechanics **1012**, A17 (2025) (CHAPTER 5).

2. **M. Draskic**, I.M.E. Nelissen and R. Pecnik, *Dynamic oscillations in the supercritical carbon dioxide natural circulation loop*, International Journal of Heat and Mass Transfer **250**, 127206 (2025) (CHAPTER 4).

3. **M. Draskic**, B. Bugeat and R. Pecnik, *The steady behavior of the supercritical carbon dioxide natural circulation loop*, Energy **294**, 130735 (2024) (CHAPTER 3).

Conference Presentations

I have had the opportunity to present my work at several conferences and scientific meetings. These events were absolute highlights of my doctoral journey, with memorable and valuable exchanges with fellow early-career researchers and great opportunities to talk science in a more relaxed, informal, and nuanced atmosphere.

- The European Conference on Supercritical CO_2 for Energy Systems, DELFT, THE NETHERLANDS (2025)

- Seminar on Non-Ideal Compressible Fluid Dynamics, LYON, FRANCE (2024)

- The European Fluid Dynamics Conference, AACHEN, GERMANY (2024)

- The J.M. Burgers Symposium, LUNTEREN, THE NETHERLANDS (2024, 2023)

- The International Supercritical CO_2 Power Cycles Symposium, SAN ANTONIO, UNITED STATES (2024)

- The J.M. Burgerscentrum Turbulence Contact Day, DELFT, THE NETHERLANDS (2023)

- The International Symposium on Turbulence, Heat and Mass Transfer, ROME, ITALY (2023)

- The European Conference on Supercritical CO_2 for Energy Systems, PRAGUE, CZECH REPUBLIC (2023)

Gallery

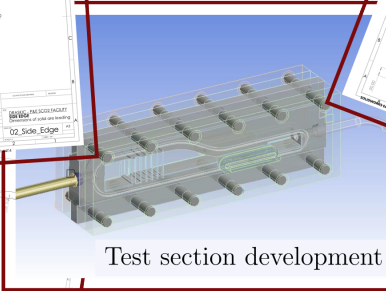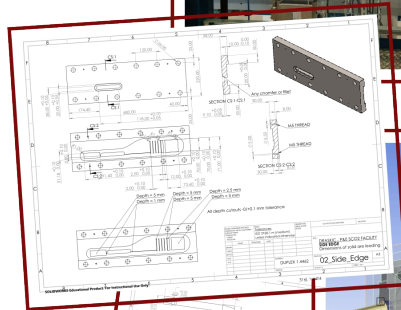Simulation of natural circulation loop dynamics
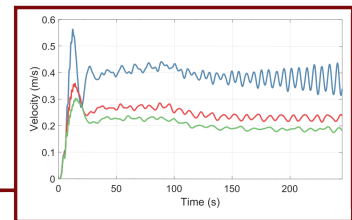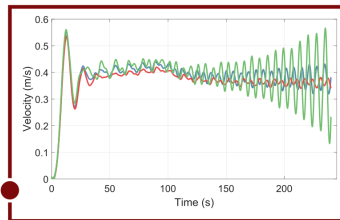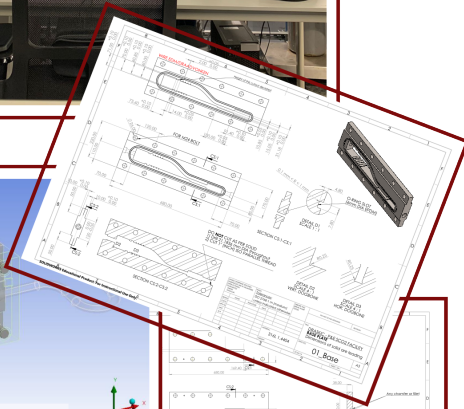

The data acquisition system
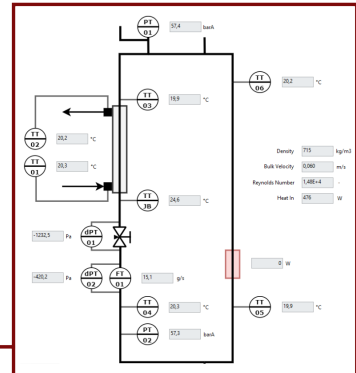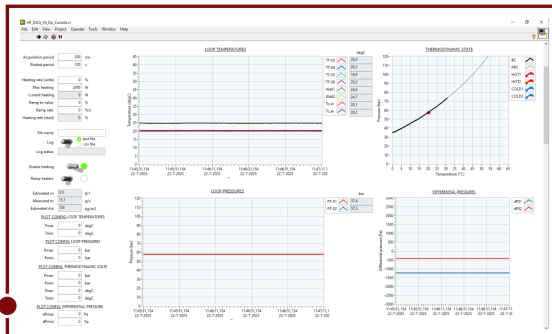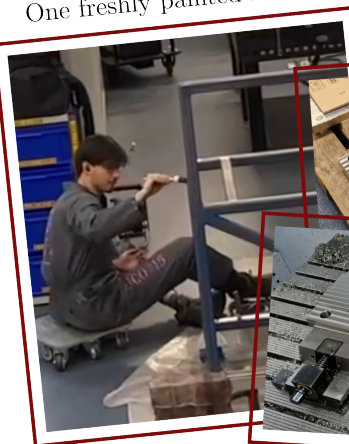

The natural circulation loop

Researchers for scale

Test section development

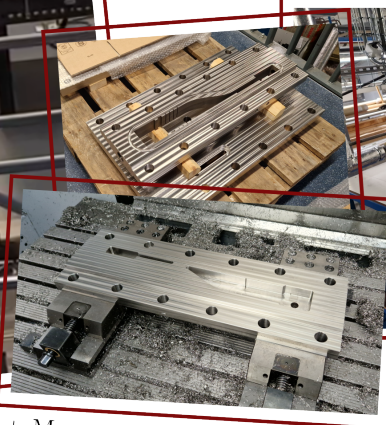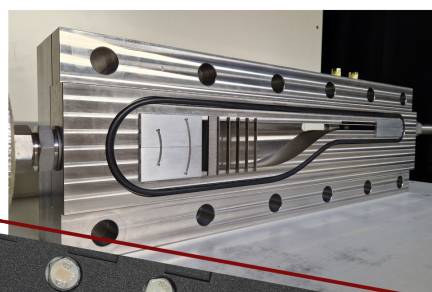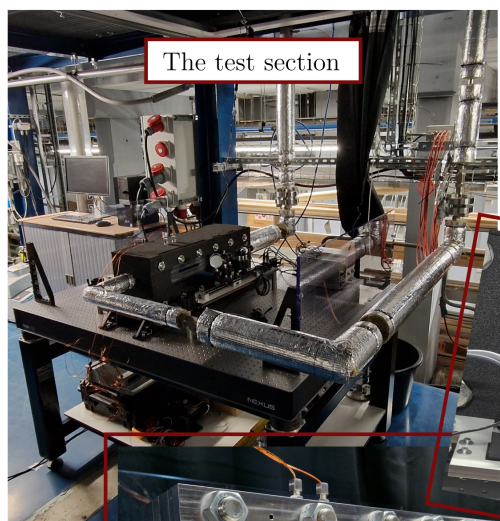One freshly painted frame

= Successful hydrostatic pressure test
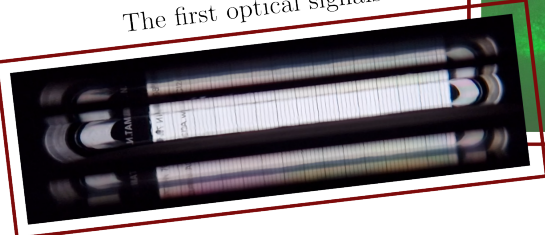
+ Many carefully machined parts

The test section

LED bundle on linear stage

The first optical signals

Critical opalescence